Lukas Kurtz

Direct and Inverse Algorithms for Characterizing Molecular Reaction Surfaces Locally and Globally

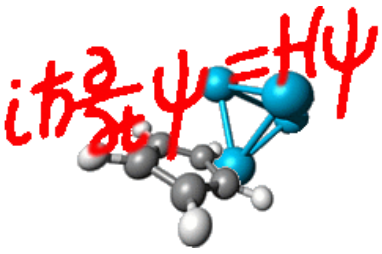

Direct and Inverse Algorithms for Characterizing Molecular Reaction Surfaces Locally and Globally

Dissertation an der Fakultät für Physik
der Ludwig-Maximilians-Universität München

Lukas Kurtz

München, den 9. Oktober 2001

1. Gutachten: PD Dr. Regina de Vivie-Riedle
2. Gutachten: PD Dr. Andreas Buchleitner

Tag der mündlichen Prüfung: 04. Dezember 2001

Zusammenfassung

In Physik und Chemie spielt der zunächst rein mathematische Begriff der Potentialfläche eine zentrale Rolle. Sie ist wesentlicher Teil der theoretischen Modellbildung und erst ihre detaillierte Kenntnis ermöglicht eine zuverlässige Abbildung des physikalischen Ursache-Wirkungsgefüges, die auch einer experimentellen Überprüfung Stand hält. Zur Gewinnung dieser Abbildung und der Reaktionsfläche sind zwei komplementäre Ansätze üblich: *Direkte* Methoden entwerfen zunächst ein Modell des Systems und konstruieren dafür Reaktionsflächen (Ursachen). Sie trachten danach, beispielsweise durch Simulationen, Messgrößen (Wirkungen) vorherzusagen, die im Wechselspiel mit dem Experiment verglichen werden und dessen Aussagen erweitern. Ein Genauigkeitsgewinn wird durch fortschreitendes Verbessern der Modellierung erzielt. Demgegenüber nutzen *inverse* Probleme experimentelle Beobachtungen (Wirkungen) unmittelbar, um damit im Rahmen eines mathematischen Modells für das untersuchte System auf die Ursachen, in diesem Fall Potentialflächen, zu schließen. Höhere Messgenauigkeit geht i. Allg. mit genaueren Reaktionsflächen einher. Die vorgelegte Arbeit macht sich beide Ansätze zu Nutze.

In Teil I wird als direkte Methode die Normalmodenanalyse (NMA) entwickelt. Hierbei werden Normalmoden als lokale Eigenschaften von *ab initio* Reaktionsflächen mit den experimentell in transienter Absorption beobachtbaren Schwingungen eines kohärenten Wellenpaketes in Beziehung gesetzt. Dieses Verfahren eignet sich besonders für (ultraschnelle) Reaktionen, in denen ein gut lokalisiertes Wellenpaket einem wohldefinierten Reaktionspfad auf der Potentialfläche folgt. Im Rahmen der Dissertationsschrift wird NMA auf zwei Systeme angewandt: Als Vorhersage eines experimentellen Signals für die photoinduzierte Ringöffnungsreaktion von Cyclohexadien und in Anwendung auf den Protontransferprozess in 2-(2'-Hydroxyphenyl)Benzothiazole; in diesem Fall zur Bestätigung eines neuen, auf experimentellen Daten fußenden Vorschlages für den grundlegenden Reaktionsmechanismus.

Teil II der Dissertation wendet sich einem inversen Problem zu, das die Reaktionsfläche selbst gewinnt. Unter Verwendung der prinzipiell messbaren zeitabhängigen Wahrscheinlichkeitsdichte $|\psi(x,t)|^2$ wird das Eherenfest-Theorem benützt eine Integrodifferentialgleichung zu formulieren, deren Lösung der Gradient der molekularen Reaktionsfläche ist. Eine einfache Integration reproduziert dann die gesuchte Fläche. In Erwartung künftiger Messdaten wird dieser Algorithmus erfolgreich auf Simulationsdaten aus einem Doppelminimum- und einem Morse-Potential angewandt. Zielsetzung ist die hohe Anwendungsfreundlichkeit des Algorithmus und eine verbesserte Genauigkeit der Lösung des inversen Problems. Dies beinhaltet die folgenden Aspekte: erweiterte Tikhonov Regularisierung zur Behebung der Schlecht-Gestelltheit des inversen Problems, Verhalten bei rauschbehafteten Eingangsdaten, unterschiedliche Kombinationsmöglichkeiten für Daten verschiedener Experimente, welche jeweils Teile der Reaktionsfläche erkunden.

Abstract

The initially purely mathematical concept of potential energy surfaces plays a central role in physics and chemistry. They are a chief ingredient to any theoretical model and it is their detailed understanding that enables the construction of a reaction mechanism that will explain the experiment and add to the understanding of the underlying concepts. Generally, two complementary approaches exist gaining these reaction surfaces: *Direct* methods construct a suitable mathematical model including reaction surfaces first, and subsequently try to infer information from it by means of simulating and predicting quantities which are compared to experimental data. Improvement is achieved by gradually increasing the model's accuracy. *Inverse* problems on the other hand, employ experimental effects to at once extract their origin, being the potential energy surfaces in this case. In this class of problems an enhanced quality of the surface results from more and improved experimental data. Both approaches have been employed.

In Part I, normal mode analysis (NMA) is developed as a direct algorithm. It employs the normal modes of *ab initio* reaction surfaces as a probe for their local characteristics and connects these to the experimentally accessible beat of a coherently vibrating wavepacket monitored in transient absorption. NMA performs best in (ultrafast) reactions where a confined wavepacket can be assumed to follow a well defined reaction path on a potential energy surface. This method is applied to two systems: For predicting the characteristic traits of an experimental trace in the photoinduced ringopening reaction of cyclohexadiene and for the excited state intramolecular proton transfer in 2-(2'-hydroxyphenyl)benzothiazole; in the latter case it serves to support a novel reaction mechanism for the transfer process put forth only recently.

Part II is concerned with an inverse problem that is capable of yielding the entire reaction surface at once. Employing the observable time dependent probability density $|\psi(x,t)|^2$ it rigorously reformulates the Ehrenfest-Theorem to yield an integro-differential equation whose solution is the surface's gradient. Integration will produce the reaction surface itself. In anticipation of expected $|\psi(x,t)|^2$-data this algorithm is successfully applied to the simulated inversion of a double-well system and a Morse potential. The goal of the investigations in this thesis is to enhance the practical utility of the method as well as to improve the solution's quality. This includes the following research topics: Extended Tikhonov regularization to reduce the ill-posedness of the inverse problem, investigation of the inversion's behavior under the influence of data noise, different combination schemes for distinct data sets, each set representing a different experiment exploring different portions of the reaction surface.

Contents

Introduction **1**

I Local Characteristics of Molecular Reaction Surfaces **5**

1 Normal Mode Analysis of Cyclohexadiene **7**
1.1 The Ringopening Reaction 7
1.2 Normal Mode Analysis – The Method 9
1.3 Results and Discussion for the Ringopening 18

2 Normal Mode Analysis of the Protontransfer in 2-(2'-hydroxyphenyl)benzothiazole **29**
2.1 The Proton Transfer Reaction – Experimental Findings . . . 30
2.2 The *ab Initio* Reaction Surface 34
2.3 Results and Discussion for the Protontransfer 35

3 Summary and Outlook for Part I **41**

II Extracting Reaction Surfaces Globally **43**

4 A Novel Extraction Scheme **45**
4.1 Introduction 45
4.2 The Basic Inversion Procedure and the Model Systems 46

5 Improved Regularization **53**

6 Combining Distinct Sets of Laboratory Data **63**
6.1 Optimal Combination of Experimental Data 63
6.2 Other Combinations of Data 68
6.3 The Influence of Noise on the Inversion 69

7 Summary and Outlook for Part II **73**

Conclusion **77**

A Selected Normal Modes of Cyclohexadiene and Hexatriene **79**

B Preparatory Rotations **83**

C Optimality Proof **87**

D Other Means of Improving the Inversion **91**
D.1 Avoiding Partial Integration for $b(x)$ 91
D.2 Scale Invariance and Search for Regularization Parameters . . 93

Bibliography **97**

Introduction

In physics and chemistry potential energy surfaces play a central role for modeling molecular processes on a microscopic scale. An accurate knowledge is required to understand ultrafast chemical dynamics on a quantum mechanical level, which is crucial for deducing the mechanisms underlying their coherent manipulation [1, 40, 46, 57, 66, 67].

In general, two ways can be distinguished that connect the theoretical model involving the reaction surface to the experimental endeavor. Both approaches will be dealt with in this thesis. The *direct* way constructs *ab initio* potential energy surfaces [21,22,32,65] with the help of a suitably constructed system Hamiltonian of the reactants. This reaction surface is then used to derive spectroscopic as well as dynamical properties of the molecular systems often related to experimental observables. In an iterative process computed results are compared to experimental results and the theoretical model is refined.

The complementary second approach deals with an *inverse* problem. Experimental data are utilized with an algorithm that directly reveals the molecular reaction surface. Improvement is achieved by incorporating more data into the problem prior to solving it.

Part I is devoted to the *direct* approach. Herein, normal mode analysis (NMA) relates the experimental traces, that contain contributions of several normal modes found in a transient absorption measurement, to the local characteristics of a quantum chemically computed reaction surface. The ability to probe the local features with normal modes is explicable by an expansion of the potential to the second order in the vicinity of an equilibrium configuration $\boldsymbol{x}_0$. Since normal modes are the eigenvectors of the Hessian they are local to the vicinity of $\boldsymbol{x}_0$ on the surface. There even is the chance that the experimental analysis provides information on the reaction path far from the neighborhood of $\boldsymbol{x}_0$. This requires the momentum acquired by the molecule along the reaction path to persist in the wavepacket's oscillations when it reaches the area of detection close to $\boldsymbol{x}_0$.

NMA is applied exemplarily to two ultrafast reactions: The photoinduced ringopening reaction of cyclohexadiene (CHD) and the excited state intramolecular protontransfer (ESIPT) in 2-(2'-hydroxyphenyl)benzothiazole

(HBT). The ringopening reaction of CHD is investigated in Chapter 1. In this ultrafast photoreaction the molecule can rapidly decay from the excited to the groundstate via multiple conical intersections. To better understand the dynamics of the molecule on its way toward the product states regarding which modes drive the reaction, a vibrational analysis towards and in the vicinity of two prominent conical intersections is performed and several eigenmodes are found to characterize its motion. These indicator modes are discussed with respect to their experimental value for rapidly detecting a specific product by a time resolved transient absorption measurement. The possibility to use these modes as feedback signals for an optimal control experiment that selectively steers the molecule through a specific conical intersection and influences the product yield is addressed as well.

Chapter 2 applies NMA to support a novel model for the ESIPT in HBT derived from recent two-color pump-probe experiments with high temporal resolution [48, 61, 77]. The reaction, experimental findings, and the novel ESIPT model are introduced first, NMA then follows.

Results are discussed in Chapter 2.3: NMA connects the recently developed theoretical model of the reaction surface to experimental findings. Theoretical and experimental results are in good agreement which is very encouraging for future applications of NMA to other ultrafast reactions. Finally, Chapter 3 concludes on NMA of molecular processes.

Part II deals with the *inverse* approach. This part presents and extends a new method extracting molecular reaction surfaces globally from time dependent probability density data available through x-ray scattering, electron diffraction, Coulomb explosion, or other experimental techniques [29,63,78]. Recently [81], novel algorithmic achievements have been presented that rigorously reformulate Ehrenfest's theorem to construct an inverse problem yielding the gradient of the potential energy surface without the need to resort to Schrödinger's equation. This original algorithm is outlined in Chapter 4 and the subsequent chapters extend this original work.

To enhance practical utility and accuracy new concepts are introduced into the extraction method. They are applied to the simulated inversion of a double well system and a Morse potential: An improved method removing the generally ill-posed nature of the inverse problem via an extended Tikhonov regularization is provided and methods for choosing optimal regularization parameters are discussed. Several ways to incorporate multiple data sets are investigated. This includes the presentation of an optimal combination scheme that will help to combine data from many experiments exploring different regions of the potential surface. In addition, results on the stability of the inversion procedure including the optimal combination scheme under the influence of data noise are discussed. Chapter 7 summarizes the findings of Part II and suggests future research topics. A general conclusion of the work presented in both parts is given in the end.

Publications

The following publications are related to my PhD studies and to the material presented in this thesis:

- Lukas Kurtz, Herschel Rabitz, and Regina de Vivie-Riedle
  Optimal use of time dependent probability density data to extract potential energy surfaces
  submitted to Physical Review A (physics/0109043).

- Vincent de Waele, Lukas Kurtz, Eberhard Riedle, and Regina de Vivie-Riedle
  Ab initio *investigation of structure and vibrational motions driving the excited state proton transfer of HBT*
  in preparation.

- Carmen M. Tesch, Lukas Kurtz, and Regina de Vivie-Riedle
  Applying optimal control theory for elements of quantum computation in molecular systems
  Chemical Physics Letters, **343** (2001) 633-641.

- Lukas Kurtz, Angelika Hofmann, and Regina de Vivie-Riedle
  Groundstate Normal Mode Analysis: Linking Excited State Dynamics and Experimental Observables
  Journal of Chemical Physics, **114** (2001) 6151-6159.

- A. Hofmann, L. Kurtz, and R. de Vivie-Riedle
  Interaction of electronic structure and nuclear dynamics on the S_1 reaction surface for the ringopening of cyclohexadiene
  Applied Physics B, **71** (2000) 391-396.

- Regina de Vivie-Riedle, Lukas Kurtz, and Angelika Hofmann
  Coherent control for ultrafast photochemical reactions
  Pure and Applied Chemistry, **73** (2001) 525-528.

- R. de Vivie-Riedle, L. Kurtz, A. Hofmann, and K. Sundermann
  Passive and active control of photochemical processes
  Journal of Information Recording, **25** (2000) 175-182.

Part I

Local Characteristics of Molecular Reaction Surfaces

Chapter 1

Normal Mode Analysis of Cyclohexadiene

Dealing with the ringopening reaction of cyclohexadiene (CHD) first, Section 1.1 will provide an introduction to this ultrafast photoreaction. Section 1.2 then introduces into the computational details of normal mode analysis (NMA). Subsequently, NMA is applied to the ringopening in Chapter 1.3 and its results are discussed. A final paragraph concludes on the findings of the NMA of CHD.

1.1 The Ringopening Reaction

One of the prominent textbook examples for an electrocyclic reaction that follows Woodward-Hoffmann rules is the photoinduced ringopening of CHD to cZc-hexatriene (cZc-HT). This is an ultrafast reaction mediated by several conical intersections (CoIns). After photoexcitation of the CHD groundstate configuration on the S_0 ($1A_1$) to the S_2 ($1B_2$) surface, the molecule rapidly decays via a CoIn to the S_1 ($2A_1$) state. From here it rushes back to the groundstate surface S_0, passing at least two other CoIns under formation of a three or fourcenter bond. Subsequently the molecule relaxes into the vibrationally excited cZc-HT and CHD (cf. Fig.1.1).

This reaction has been studied by means of quantum chemistry [3, 6, 26, 27], by resonance-Raman spectroscopy [58–60, 69, 70], and by femtosecond spectroscopy in solution [47, 54–56] as well as in gas phase [25, 71]. All experimental results confirm the ultrashort reaction times around 200 fs, explicable only by direct barrierless transitions to the groundstate via CoIns connecting the S_1 and S_0 states.

Several theoretical studies already describe dynamics in the vicinity of CoIns. Some simulate real molecules by means of normal mode expansion [75, 76] while others investigate model systems of two or three modes

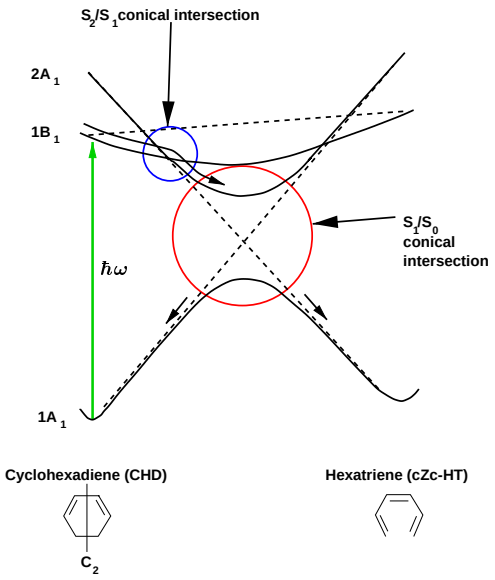

Figure 1.1: Schematic drawing of CHD's photoinduced ringopening reaction. Potential energy curves are given as full lines according to the Woodward-Hoffmann rules (dashed lines). The circles mark the conical intersections with the S_1/S_0-CoIn outside the depicted plane.

only [18–20]. In our group we intend to study CHD's reactive dynamics on the S_1-surface by wavepacket propagation on multidimensional interpolated *ab initio* potential energy surfaces (PES) to gain microscopical insight into the mechanism driving the system toward and through the conical intersections. A detailed model including the coupling between the PES could be developed and has been implemented successfully in parallelized numerical code. Remarkable, purely quantum mechanical effects influencing the product yield have been discovered [35, 36, 38].

The initial quantum mechanical approach to this reaction on the S_1-surface was through the computation of two prominent minimum energy paths (MEPs), that were either truly of minimal energy or under the constraint to preserve the educt's C_2-symmetry, see [27] for an overview. Both of them end in two prominent conical intersections between the S_1 and S_0-surface ($CoIn_{Min}$ and C_2-CoIn respectively). As reported recently [28], both CoIns appear to be part of a seam of conical intersections.

On return to the groundstate PES via $CoIn_{Min}$ and C_2-CoIn, vibrationally excited CHD and cZc-HT are found. The question arises, which information could be extracted in a transient absorption measurement from the beating of normal modes as soon as the reaction product reaches the

groundstate surface? The aim of the following chapters is to develop NMA as an algorithm to answer this question and also to find out which modes are predominantly involved in the molecule's dynamics.

Identifying dominant modes and extracting fingerprints local to a reaction path not only might help to quickly show in an experiment which of the two products is mainly created, but it could also be helpful in determining the conical intersection the molecule predominantly passed on its way.

This signature would provide a feedback signal for an optimal control experiment to selectively steer the molecule through a specific CoIn and influence a desired product's yield.

The subsequent sections describe how normal mode analysis can be helpful in this process. First, a description of the computational method to extract Fourier coefficients from static quantum chemical molecular structures will be given, supplemented by material presented in Appendix B. This derivation is followed by applying NMA to the ringopening reaction and the discussion of the results in Chapter 1.3. The final part summarizes the findings for the ringopening reaction of CHD. Additional material describing the molecular motion in characteristic normal modes that further supports the microscopic understanding of the reactive process is provided in Appendix A.

1.2 Normal Mode Analysis – The Method

In principle, a bound classical vibrational motion can be composed of the normal modes suited best for the molecular state one wishes to describe. The focus here is on the detection of these modes as soon as the molecule reappears on the S_0 surface as vibrationally hot CHD or cZc-HT. It is supposed that a specific reaction path chosen by the excited molecule will imprint a distinct mode pattern onto the vibrations that are detected when the molecule is monitored on the groundstate surface.

The goal is to find a quickly identifiable fingerprint of the expected product via these vibrations as well as extracting information about the molecule's evolution in the excited state. Therefore NMA focuses on the vicinity of both S_1-S_0 CoIns on the S_1 surface mentioned in Section 1.1 but is using the eigenmode system of groundstate CHD and cZc-HT to identify such fingerprint modes. Information about the evolution on the S_1 surface is of particular value since it was shown that the molecule's frame and the molecular orbitals change strongly on this S_1-PES. Hence this surface is understood to determine the overall reaction dynamics and product yield [37] of the ringopening process of CHD.

A future aspect that is addressed here as well is coherent guidance of the photoreacting system with laserbeams thus influencing the product yield

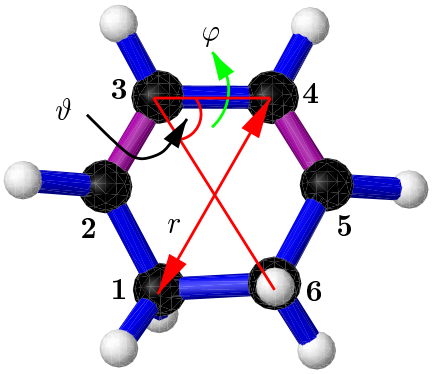

Figure 1.2: Reactive coordinates account for the relevant changes during the evolution on the S_1 surface and contain the important modes active on the femtosecond timescale. The torsional angle ϑ and φ the dihedral angle are two C_2-symmetric degrees of freedom, the distance r describes an asymmetric bending motion. To simplify descriptions all the carbon atoms have been labeled. Figure adapted from [36].

with the help of optimal control (OCT) schemes. The principle of focusing a wavepacket at a CoIn could already be proven in previous calculations in our group [8].

In previous computations performed in our group [35, 36, 38] it could be demonstrated that the complex 36-dimensional nuclear motion on the S_1-PES can be to be readily described with the help of reactive coordinates shown in Fig. 1.2. Already the dihedral angle φ and distance r very well describe quantum mechanical effects such as the coherent bifurcation of a wavepacket on its way towards the two S_1-S_0 CoIns (see Fig. 1.4). Both of them are reached, yet with different branching ratios – and thus product yields – that are influenced by the initial state preparation [35, 36, 38].

Although reactive coordinates are a powerful tool to simulate CHD's S_1-dynamics there is a drawback for NMA. This efficient reduction of the full 42-dimensional atomic coordinate space to only three degrees of freedom impedes the inversion of the problem. Without additional quantum chemical computations it is impossible to recompute from r, φ, ϑ the x, y, z positions of all atoms and to perform NMA for the wavepacket. However, simulations show all the wavepackets moving in a region bounded by two different minimum energy paths (MEPs). These MEPs will be described in more detail below.

For the wavepackets displayed in Fig. 1.4 the time evolution of their position averages was evaluated. They move on simple trajectories like classical particles (see Fig. 1.3) and reflect the abilities of the MEPs to serve as boundaries. Fortunately, all atoms' positions for several configurations along both paths are exactly known so these configurations are amenable to NMA.

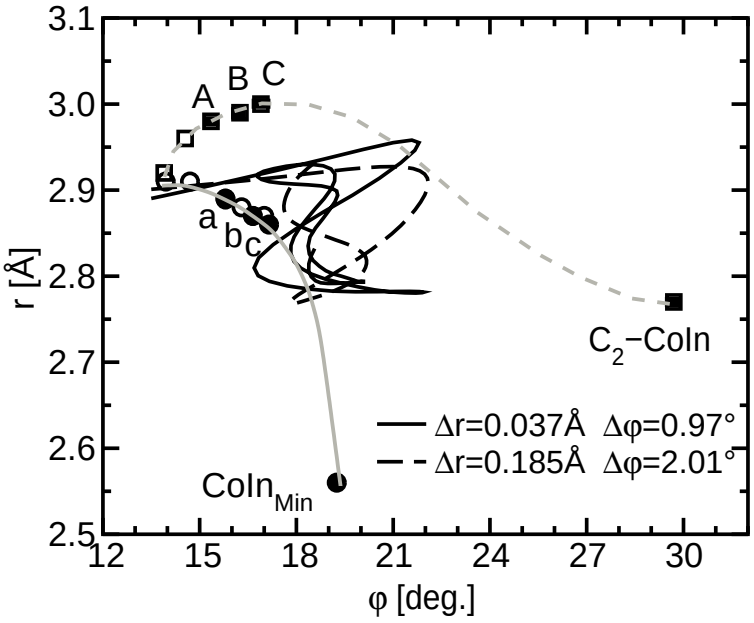

Figure 1.3: Position averages and MEPs in reduced reactive coordinates r, φ. The true MEP (solid grey guide to the eye) and the C_2-symmetry conserving MEP (dashed grey) are shown together with the position averages of the wavepackets displayed in Fig. 1.4 (black lines). Points C and c have minimal potential energy on either MEP. Although the initial maxima of both wavepackets were chosen close to the S_2-S_1 CoIn around $(2.9\,\text{Å}, 14°)$, the computation of position averages in non-Cartesian coordinates leads to different starting points for the $\langle x(t)\rangle$. Time evolution of the narrow wavepacket (solid black) is truncated after 118.5 fs, after 58.7 fs for the broad wavepacket (dashed black). Filled squares and circles indicate the configurations selected for NMA.

For the position averages, Fig. 1.3 reveals the initially C_2-symmetric molecule accelerated into the direction of the C_2-MEP first, but only to turn toward the true MEP later. Although some parts of both wavepackets clearly reach both CoIns (see Fig. 1.4), the position average remains far away from them and exhibits a damped oscillatory motion. This damping is due to fast parts of the wavepacket that quickly reach the intersections and are funneled to the lower-lying PES. Hence they cannot contribute to the averaging process and one is left with slow components of the wavefunction prevailing in the vicinity of the S_1-minimum.

Both MEPs connect the S_2-S_1 and the two S_1-S_0 CoIns. All computation were performed by other authors [6, 27, 28]. One MEP is the actual path of minimal potential energy and leads to the energetically lower lying CoIn_{Min} (true MEP), the other is a route conserving the C_2-symmetry of the educt

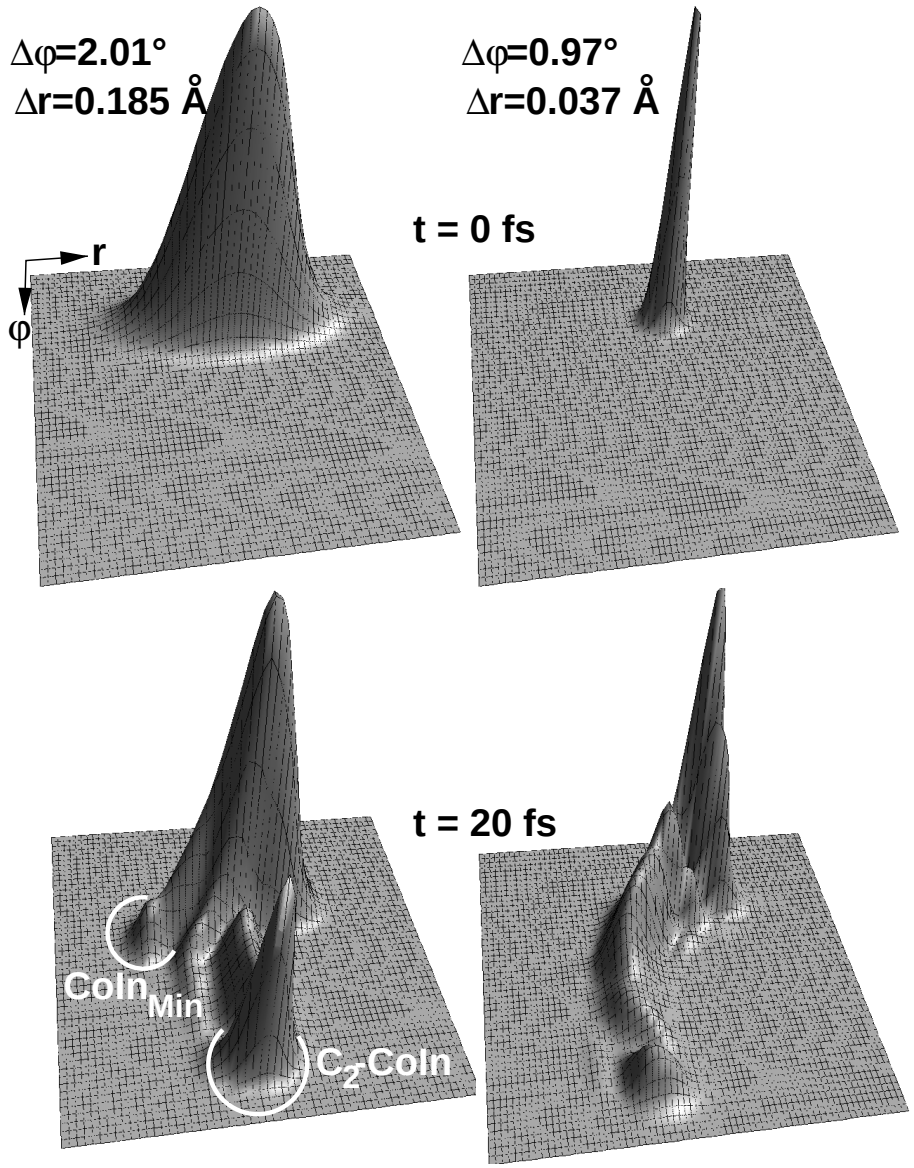

Figure 1.4: Snapshots of the time evolution of two wavepackets $r^2|\Psi|^2$ on the S_1 surface (cf. Fig. 1.5) in reduced reactive coordinates r and φ. Depending on the widths Δr and $\Delta\varphi$ of the initial Gaussian packets (roughly simulating different schemes of laser excitation) they show different coherent branching but still can reach both CoIns after several femtoseconds. The CoIn regions are exaggerated for graphical clarity. Details can be found in [35].

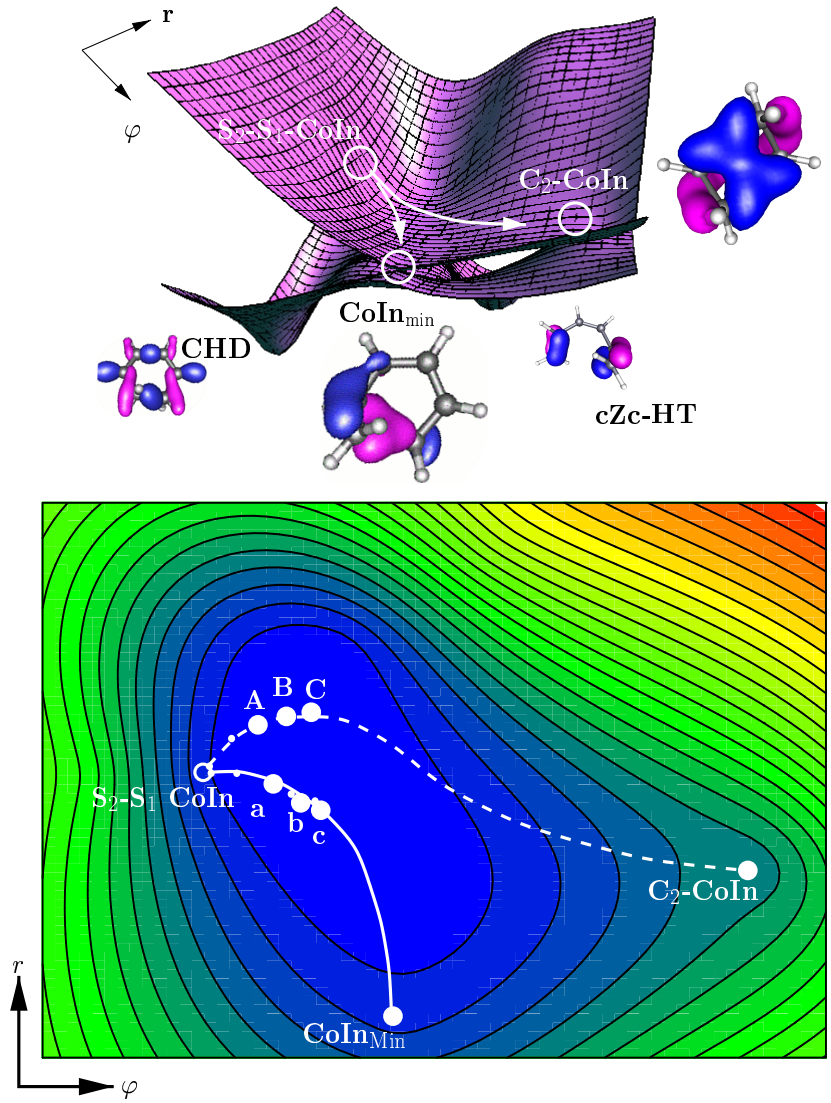

Figure 1.5: TOP: The S_0 and S_1 PES in reduced reactive coordinates r, φ as used for the wavepacket simulations in [35]. Circles indicate the active CoIns. CHD's and cZc-HT's groundstate equilibrium structures correspond to the two minima on the S_0-surface. MOs involved in the ringopening process are included illustrating the formation of a four-center bond at C_2-CoIn and of a three-center bond at $CoIn_{Min}$. BOTTOM: Contour plot of parts of the S_1-surface : $r = 2.5 \ldots 3.3, \varphi = 9° \ldots 32°$. Quantum chemically computed MEP configurations (small white dots) are connected by guides to the eye (full: true MEP, dashed: C_2-MEP). Enlarged full circles indicate configurations selected for NMA: A (1.5), B (2.0), C (C_2 2A-Min), C_2-CoIn and a (1.5), b (1.98), c (2A-Min), $CoIn_{Min}$. Labels in braces refer to positions and distances along the MEP-coordinate in [27]. These are the labels employed in subsequent figures.

state and ends at the C_2-CoIn (C_2-MEP). The symmetry conserving C_2-CoIn lies at higher potential energy than $CoIn_{Min}$ which can also be inferred from the contour plot in Fig. 1.5.

The conical intersections coincide with the formation of a multi-center bond replacing the C_1-C_6 σ-bond. The behavior of the corresponding molecular orbitals (MOs) is illustrated for the true MEP in Fig. 1.6 and for the C_2-MEP in Fig. 1.7. In both cases, a strong interdependence between the concerted electronic and the nuclear motion is observed when the excited molecule sweeps across the S_1-surface.

Figure 1.6 shows that close to the groundstate structure MO 20 has dominant σ-bond character including the C_1-C_6 bond, where the breaking will occur. At 3 au down the MEP the initial C_2-symmetry is broken and the σ-bond type orbital obtains small π-orbital contributions. Around 4.5 au the system crosses from the S_2 to the S_1 state and the σ electrons are pushed further into the π-orbital system. During the evolution from MEP position 5.95 (structure 1.98) to the pericyclic minimum (2A-Min) at 6.36 au along the MEP the energies of both MOs approach each other. A fast cyclic motion of the electrons is observed despite the minimal change of the nuclear frame.

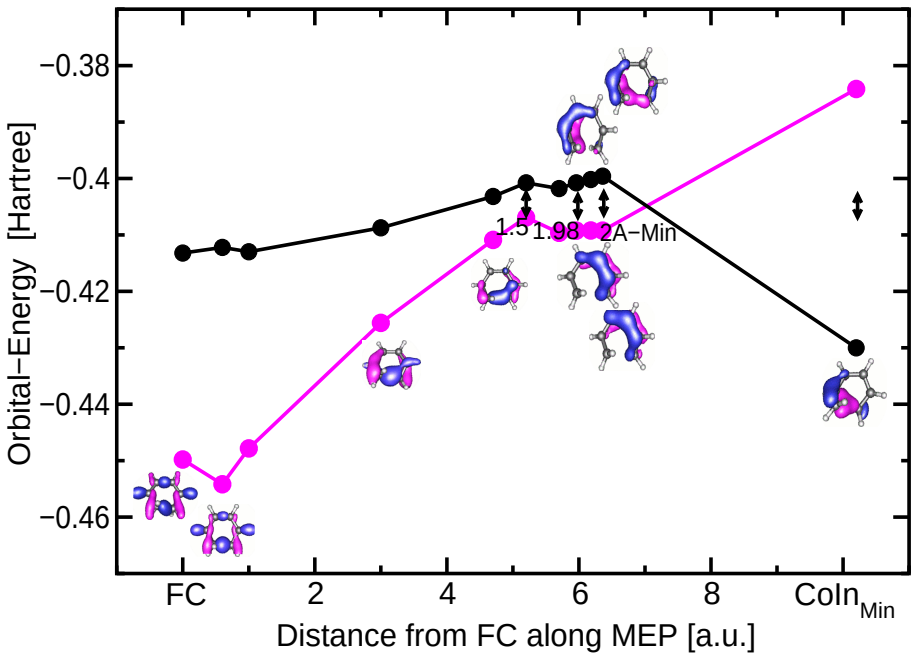

Figure 1.6: MOs 20 and 21 along the full minimum energy paths connecting the FC region on the S_2-surface with $CoIn_{Min}$ on the S_1-surface (cf. [37]). Distances on the abscissa refer to this full MEP. Arrows point to structures selected for NMA and the corresponding labels refers to those employed in the text and in subsequent figures. All orbitals were evaluated with a 6-31G* basis set with Gaussian94 [23]. See the text for further details.

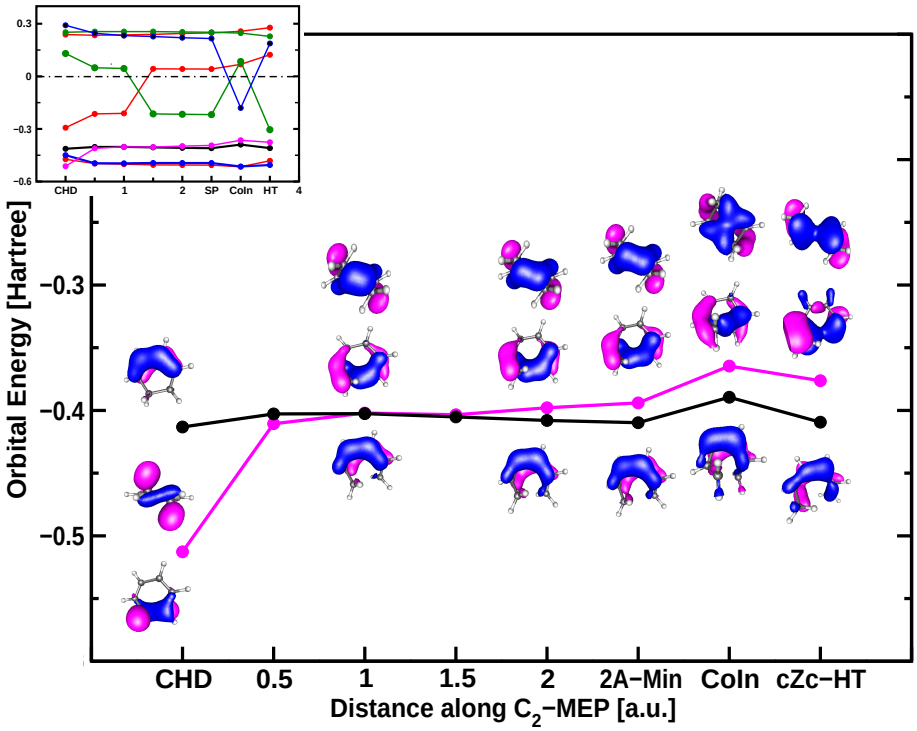

Figure 1.7: Evolution of MOs along the C_2- MEP on the S_1-surface. The evolution of all MOs is displayed in the small inset while the the larger part shows the concerted electronic motion in MOs 20 and 21 only. Abscissa labels refer to the distance from the S_2-S_1 CoIn! Compare to Fig.1.6. Consult the text for details.

While the motion in the previously dominant MO 20 slows down now, MO 21 takes over a major role. It finally forms a three-center bond at $\mathrm{CoIn}_{\mathrm{Min}}$.

For the C_2-symmetric path the observed changes are in accordance with the constraint to conserve symmetry, Fig. 1.7. While the HOMO and LUMO orbitals only show large energetic but not structural changes along the C_2-MEP, MOs 20 and 21 also exhibit strong changes in the electron density, similar to the non-symmetric case in Fig. 1.6. In contrast to the latter case, the electrons show no fast pericyclic movement around the open ring and result in the formation of a four-center bond at C_2-CoIn this time.

To introduce into the NMA method a classical, dynamical viewpoint is employed. An exact position $\boldsymbol{q}_i(t) = [x_i(t), y_i(t), z_i(t)]^{\mathrm{T}}$ can be assigned to each atom $i = 1, 2, \ldots, 14$ in CHD. Neglecting all intramolecular effects but vibrations the atomic motion in a harmonically vibrating molecule can be

expressed as

$$\boldsymbol{q}_i(t+\mathrm{d}t) = \boldsymbol{q}_i(t) + \boldsymbol{R} + \boldsymbol{\Omega} \times \boldsymbol{q}_i(t)\,\mathrm{d}t + \sum_{j=1}^{36} c_j\,\boldsymbol{\xi}_{ij}\cos(2\pi\nu_j t + \phi_j) \tag{1.1}$$

as time advances $t \to t + \mathrm{d}t$.

This describes for every atom i the new position $\boldsymbol{q}_i(t+\mathrm{d}t)$ in terms of the old position $\boldsymbol{q}_i(t)$, a translational displacement of the center of mass $\boldsymbol{R}$, a rotational displacement of the whole molecular skeleton $\boldsymbol{\Omega} \times \boldsymbol{q}_i(t)$, and of the intramolecular motion due to the 36 vibrational degrees of freedom. $\boldsymbol{\xi}_{ij}$ is atom i's eigenvector of mode j and c_j are the dimensionless Fourier coefficients. Both, frequencies ν_j and Cartesian eigenvectors $\boldsymbol{\xi}_{ij}$ of the eigenmodes of the CHD- and cZc-HT groundstate, were obtained with Gaussian94 [23] in harmonic approximation on RHF level with a 4-31G basis set. This basis suffices to demonstrate the ideas of this approach.

Combining all nuclear positions $\boldsymbol{q}_i$ in a 42-dimensional vector $\boldsymbol{X} = [\boldsymbol{q}_1^{\mathrm{T}}, \boldsymbol{q}_2^{\mathrm{T}}, \ldots, \boldsymbol{q}_{14}^{\mathrm{T}}]^{\mathrm{T}}$ and introducing a solution vector $\boldsymbol{c}$ of equal dimension the above equation (1.1) can be reformulated as matrix problem

$$\begin{aligned} \boldsymbol{\Delta} &:= \boldsymbol{X}(t+\mathrm{d}t) - \boldsymbol{X}(t) \\ &= \boldsymbol{\Theta}(t) \cdot \boldsymbol{c}\,. \end{aligned} \tag{1.2}$$

The 42×42 time-dependent matrix $\boldsymbol{\Theta}(t)$ comprises vibrational motion as well as the molecule's rotation and translation

$$\boldsymbol{\Theta}(t) := \left[\widetilde{\boldsymbol{\Xi}}(t)\ \widetilde{\boldsymbol{\Omega}}(t)\ \widetilde{\boldsymbol{R}}\right] \tag{1.3}$$

with the 42×36 submatrix

$$\widetilde{\boldsymbol{\Xi}}(t) := \begin{bmatrix} \xi_{1x,1}\cos(2\pi\nu_1 t + \phi_1) & \cdots & \xi_{1x,36}\cos(2\pi\nu_{36} t + \phi_{36}) \\ \xi_{1y,1}\cos(2\pi\nu_1 t + \phi_1) & \cdots & \xi_{1y,36}\cos(2\pi\nu_{36} t + \phi_{36}) \\ \xi_{1z,1}\cos(2\pi\nu_1 t + \phi_1) & \cdots & \xi_{1z,36}\cos(2\pi\nu_{36} t + \phi_{36}) \\ \vdots & \ddots & \vdots \\ \xi_{14z,1}\cos(2\pi\nu_1 t + \phi_1) & \cdots & \xi_{14z,36}\cos(2\pi\nu_{36} t + \phi_{36}) \end{bmatrix} \tag{1.4}$$

and the 42×3 parts for translational

$$\widetilde{\boldsymbol{R}} := \begin{bmatrix} R_x & 0 & 0 \\ 0 & R_y & 0 \\ 0 & 0 & R_z \end{bmatrix} \otimes \begin{bmatrix} 1_1 \\ 1_2 \\ \vdots \\ 1_{14} \end{bmatrix} \tag{1.5}$$

and rotational changes

$$\widetilde{\boldsymbol{\Omega}}(t) := \begin{bmatrix} (\boldsymbol{\Omega} \times \boldsymbol{q}_1(t))_x & 0 & 0 \\ 0 & (\boldsymbol{\Omega} \times \boldsymbol{q}_1(t)))_y & 0 \\ 0 & 0 & (\boldsymbol{\Omega} \times \boldsymbol{q}_1(t))_z \\ (\boldsymbol{\Omega} \times \boldsymbol{q}_2(t))_x & 0 & 0 \\ \vdots & \vdots & \vdots \\ 0 & 0 & (\boldsymbol{\Omega} \times \boldsymbol{q}_{14}(t))_z \end{bmatrix} \mathrm{d}t \; . \tag{1.6}$$

In principle, inverting Eq. (1.2) yields the solution vector $\boldsymbol{c}$ describing all atomic displacements. By construction are its first 36 entries the vibrational Fourier coefficients and the last six should all be either "1" if described in a frame of reference in which the molecule experiences translation and rotation or "0" if it is at rest. However, in the latter case $\widetilde{\boldsymbol{R}}$ and $\widetilde{\boldsymbol{\Omega}}$ are zero, hence Eq.(1.2) is underdetermined.

The basic question NMA will answer is: *Which eigenvector $\boldsymbol{\xi}_j$ must be added with which Fourier amplitude c_j to the groundstate equilibrium configuration of CHD or cZc-HT to follow the MEP?*

The time dependent viewpoint will prove helpful in solving this problem. It provides a solution to Eq.(1.2), which also lends itself quite favorably to indicate the computation's numerical quality.

Only static information is available dealing with quantum chemically computed configurations. However it is useful to adopt a point of view that treats the positions along the MEP like an overdamped motion. Thus in Eq.(1.2) each location $t + \mathrm{d}t$ along the MEP is considered the starting point of a new vibration with $\cos(2\pi\nu_j\, t + \phi_j) = 1$ always. Information about the phase variables $\phi_j = 0$ cannot be obtained and every normal mode contributes only through the eigenvector $\boldsymbol{\xi}_j$. Its frequency ν_j is not accounted for.

In this sense, NMA is a projection method and its dynamic introduction given above must be understood as a more general ansatz. Time is considered merely as an index of the molecule's position on the MEP. In the following, the groundstate equilibrium configuration is referred to with time t and $\boldsymbol{X}_{\mathrm{ref}} = \boldsymbol{X}(t)$ and all the MEP configurations investigated are using times $t + \mathrm{d}t$ and are denoted $\boldsymbol{X}(t + \mathrm{d}t)$.

Accordingly, the rotation and translation submatrices have to be adapted to suit the needs of NMA. For $\widetilde{\boldsymbol{R}}$ in Eq.(1.5) the entries $R_x = R_y = R_z = 1$ are chosen, and for $\widetilde{\boldsymbol{\Omega}}$ in Eq.(1.6) rotational displacement vectors are selected. Employing the usual rotation matrix $\boldsymbol{U}_k(\eta)$ around the k-axis $k \in \{x, y, z\}$ for an angle, say, $\eta = 1^\circ$ the displacement

$$\boldsymbol{\delta}_k := \boldsymbol{X}_{\mathrm{ref}} - \boldsymbol{U}_k(\eta) \cdot \boldsymbol{X}_{\mathrm{ref}} \tag{1.7}$$

is computed for all three axes. The rotation submatrix $\widetilde{\boldsymbol{\Omega}}$ is then combined from

$$\widetilde{\boldsymbol{\Omega}} = [\boldsymbol{\delta}_x \; \boldsymbol{\delta}_y \; \boldsymbol{\delta}_z] \tag{1.8}$$

and the solution coefficients in $\boldsymbol{c}$ for these "modes" apply to small, artificial rotations. Of course, an error is introduced at this stage since this approach neglects that rotations cannot be interchanged. However, $\widetilde{\boldsymbol{R}}$ and $\widetilde{\boldsymbol{\Omega}}$-entries are used as indicators only. Ultimately, only negligibly small contributions should be accepted.

The resulting $\boldsymbol{\Theta}$-matrix is invertible and will provide solutions to the projection problem, which are still open to improvement by iteration. By construction, the meaning of the $\widetilde{\boldsymbol{\Omega}}$ and $\widetilde{\boldsymbol{R}}$-entries in the solution vector $\boldsymbol{c}$ is clear. On convergence, these solution coefficients are practically zero if all residual translation and rotation has been compensated for. Only the first 36 Fourier amplitudes, describing vibrations in the solution vector $\boldsymbol{c}$, are of interest and will be presented here.

It is crucial to accurately account for the possible shift of the center of mass, and the MEP-configuration $\boldsymbol{X}(t + \mathrm{d}t)$ must be rotated into closest distance of $\boldsymbol{X}_{\mathrm{ref}}$! A suitable method is outlined in Appendix B. Only then will $\boldsymbol{\Delta}$ in Eq.(1.2) describe the structural change of the molecular skeleton as pure vibrations.

In practice, the compensation procedure is repeated until all six ancilla Fourier amplitudes vanish. Furthermore, the first 36 Fourier coefficients in the solution vector $\boldsymbol{c}$ are cross checked with results obtained by singular value decomposition of $\widetilde{\boldsymbol{\Xi}}$[1)].

1.3 Results and Discussion for the Ringopening

With the NMA-method introduced in the preceding Section 1.2 the Fourier coefficients of selected excited state molecular configurations along both MEPs were calculated. The eight configurations highlighted in Fig. 1.3 were chosen since they are closest to the two CoIns and each position has a twin configuration on the other path, that is a similar distance away from the S_2-S_1 intersection. The resulting amplitudes are displayed in Figs. 1.8 and 1.9. Note that for CHD as well as cZc-HT their magnitude doesn't vanish completely, neither when the molecule is at the potential energy minimum nor when it reaches the CoIns. This is due to choosing the normal mode system of the groundstate molecules and not expanding in eigenmodes of an excited state configuration.

[1)] Since computational time is not an issue here the Matlab package was utilized to solve Eq.(1.2) and to perform the cross checks.

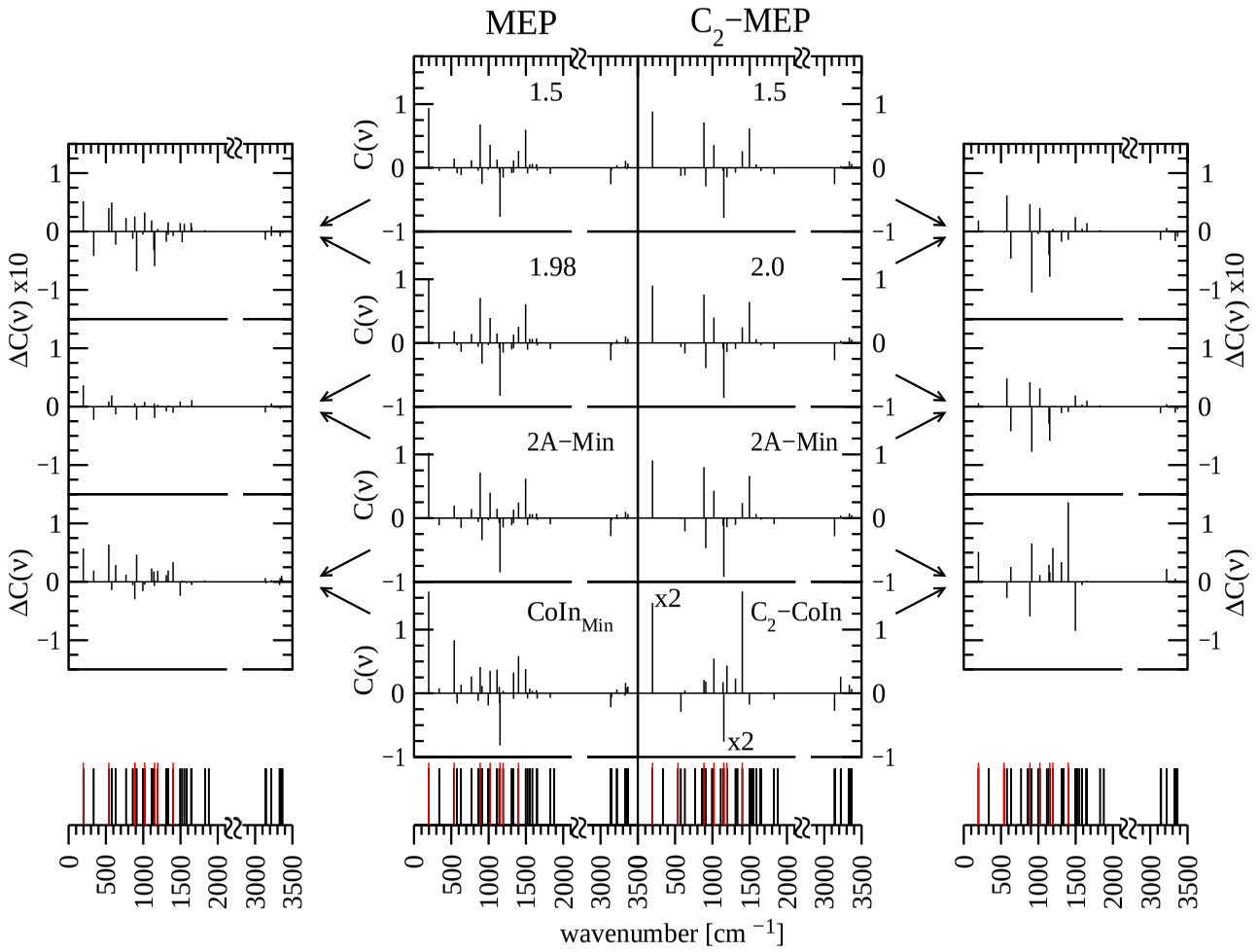

Figure 1.8: The coefficients $c(\nu)$ of CHD computed for the four molecular configurations along the true MEP (center left) and for the four along the C_2-MEP (center right) (comp. Fig. 1.3). If required multiply $c(\nu)$ with the specified factor to regain the correct values. The outer panels display the differential spectra for two neighboring configurations as indicated by arrows (results partly enlarged by a factor of ten). Changes in the solution coefficients can be due to adaptation to the anharmonicity of the potential, or could result from a harmonic evolution. This difference cannot be resolved with the diffusive ansatz. The eigenmodes' frequencies are displayed as stick spectra below with significant modes highlighted (see table 1.1a). Note the discontinuous frequency axis.

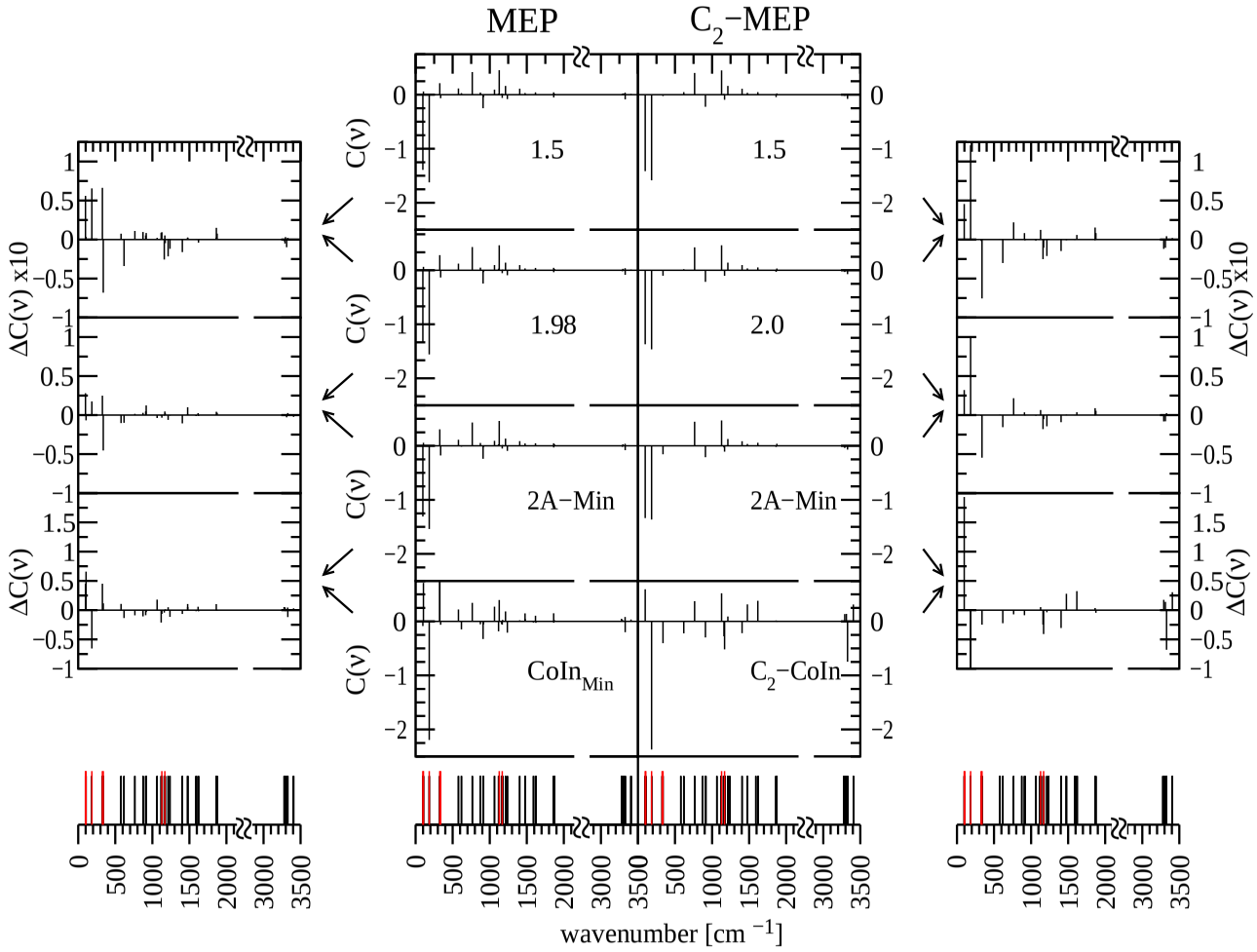

Figure 1.9: Fourier coefficients $c(\nu)$ and differential spectra along the two MEPs in the eigenmode system of cZc-HT, compare to Fig. 1.8. The highlighted modes in the lowest panel correspond to the fingerprint modes given in table 1.1b. Not all of them can be resolved on the figure's scale.

a)

ν [cm^{-1}]	$c(\nu)_{C_2}$	$c(\nu)_{\mathrm{Min}}$
196	2.8391	1.5975
539	0.0000	0.8340
887	0.2096	0.4133
1020	0.5467	0.3538
1153	-1.5211	-0.8185
1195	0.4363	0.0391
1401	1.5995	0.5857

b)

ν [cm^{-1}]	$c(\nu)_{C_2}$	$c(\nu)_{\mathrm{Min}}$
97	0.5951	-0.8557
106	0.0000	0.7142
184	-2.3717	-2.1956
326	0.0000	0.7578
338	-0.4036	-0.0620
1128	0.5209	0.3963
1169	-0.5172	-0.0588

Table 1.1: The Fourier amplitudes $c(\nu)$ of seven dominant modes. These vibrations very well reproduce the characteristic features of the vibronic motion that is assumed to set off at each of the CoIns (comp., Fig. 1.10). (a) refers to the CHD and (b) to the cZc-HT eigenmode system. While the right columns are amplitudes found at the conical intersection of minimal energy $\mathrm{CoIn}_{\mathrm{Min}}$, results in the middle correspond to the findings for the C_2-symmetric CoIn.

Both figures are organized as follows: The two columns on the left refer to the true MEP, the two on the right to the C_2-MEP. For comparison the frequencies of all normal modes are given as stick spectra in the lowest panel. Please note the discontinuous frequency axis. Solution coefficients $c(\nu)$ are displayed in the central block of both figures, while their differential change is shown in the spectra in the outer panels of Figs. 1.8 and 1.9. These differential spectra are computed according to $\Delta c(\nu)_N := c(\nu)_N - c(\nu)_{N-1}$ between two neighboring configurations $(N, N-1)$ on either MEP (indicated by arrows).

For CHD (Fig. 1.8) many modes are required to describe the configurations along both MEPs. Centered around 1200 cm^{-1}, their energy range spans almost the entire spectrum below 2000 cm^{-1}, the lowest frequency 196 cm^{-1} sharply peaked. While some eigenmodes are contributing strongly along the whole path, some are rising sharply at the CoIns (e.g., modes 539 cm^{-1} and 1401 cm^{-1}). Fewer frequencies are important in the C_2-symmetric case, but all in all the seven modes given in table 1.1a suffice to properly reproduce the vibronic motion at both CoIns. These dominant modes also help to distinguish between the symmetry constrained and unconstrained MEP (see text below and Appendix A for illustrations of the molecule's motion in several normal modes). These indicator eigenmodes have been highlighted in the spectra of Fig. 1.8.

Another facet of our analysis has proven invaluable for the quantum mechanical simulations performed in our group. We found reactive coordinates to properly capture the relevant geometrical changes on the S_1-surface during the ringopening reaction and to have a large overlap with many vi-

a)

ν [cm^{-1}]	dr	dϑ	dφ
196	0.03	0.03	**0.67**
539	**0.12**	**0.18**	0.06
578	0.01	0.02	**0.48**
631	**0.10**	**0.10**	**0.15**
860	0.03	**0.11**	0.03
887	0.07	0.02	**0.11**
912	0.06	0.02	**0.31**
1112	0.01	**0.19**	0.05
1142	0.01	0.03	**0.42**
1153	0.01	0.07	**0.45**
1195	0.01	0.01	**0.14**
1401	0.02	0.01	**0.14**
1827	0.01	**0.13**	0.07
1879	0.06	**0.23**	0.07
3138	0.01	0.00	**0.14**

b)

ν [cm^{-1}]	dr	dϑ	dφ
97	0.01	0.02	**0.29**
184	0.05	**0.11**	0.07
326	**0.10**	**0.14**	0.01
338	0.05	0.07	**0.45**
578	0.02	**0.11**	0.02
619	0.03	**0.11**	**0.27**
764	0.02	0.08	**0.23**
874	0.04	**0.19**	0.01
910	0.09	0.05	**0.13**
1065	0.01	**0.27**	0.05
1128	0.01	0.01	**0.12**
1161	0.02	0.05	**0.16**
1169	0.01	0.01	**0.11**
1213	0.01	0.06	**0.19**
1623	0.01	**0.10**	0.02
1864	0.01	**0.10**	0.04
1875	**0.12**	**0.11**	0.04

Table 1.2: Projection of the normal modes of CHD (a) and cZc-HT (b) onto the reactive coordinates. Given are the relative displacements dr,dϑ, and dφ together with the mode's frequency (cf. [37]). Large changes are printed in bold. Modes are underlined if they appear in tables 1.1a and 1.1b as well.

brational eigenmodes of CHD and cZc-HT, see the reproduced tables 1.2a and 1.2b and [37]. The present analysis now further supports that reactive coordinates are well designed since the dominant modes found in table 1.1 are among those well described with reactive coordinates.

The aforementioned modes 539 cm^{-1} and 1401 cm^{-1} are particularly valuable. Mode 1401 cm^{-1} drives the molecule further away from planarity and affects the C_2-symmetric dihedral angle φ. It shows a large contribution at the C_2-symmetric CoIn. On the other hand mode 539 cm^{-1} strongly promotes changes in the asymmetric length r. It is prominent at the asymmetric CoIn only. These two might come in handy as fingerprint frequencies to distinguish between molecules passing predominantly $\mathrm{CoIn}_{\mathrm{Min}}$ or the C_2-CoIn.

Inspecting the results for cZc-HT (Fig. 1.9) almost the entire frequency range below 2000 cm^{-1} is found to be involved. Preference lies on the low energy regime where eigenmodes mostly involve the carbon backbone of the molecule. Higher frequency modes already have large contributions of wagging C-H bonds and are of lesser interest to the reaction's dynamics.

By construction the reactive coordinates in figure 1.2 only account for their contributions on a coarse grained level (see [35, 36] for details).

Only minor changes of amplitudes for most frequencies along both MEPs (outer panels of Fig. 1.9) are observed, yet some rise sharply at the corresponding CoIn. The C_2-symmetric MEP again requires fewer modes for description. Several dominant eigenmodes were selected that very well describe molecular oscillations that can be initiated after passing the CoIns (see Fig. 1.10). The seven candidates are listed in table 1.1b and are highlighted in the eigenmode spectra of Fig. 1.9.

Identifying experimentally reliable fingerprint modes that would help to pinpoint the proper CoIn passed by the molecule is difficult for both molecules. Some modes tend to vanish while others to show up: 97 cm^{-1} vs. 106 cm^{-1}, 326 cm^{-1} vs. 338 cm^{-1}. We have found especially the latter two to be well accounted for in reactive coordinates (cf. [37] and table 1.2), where eigenmode 338 cm^{-1} drives a C_2-symmetric φ motion and mode 326 cm^{-1} dominantly affects the asymmetric length r.

Unfortunately, all these modes are almost degenerate and experimentally indistinguishable, which poses a major experimental difficulty. Consequently it will be also very difficult to find a suitable feedback signal for an optimal control experiment. The best candidate for cZc-HT is mode 1169 cm^{-1}. Its solution coefficients $c(\nu)$ for $\mathrm{CoIn}_{\mathrm{Min}}$ and C_2-CoIn are large enough to suggest good experimental detectability, yet they differ by a factor of ten. This makes the two cases easily distinguishable. The drawback is that CHD possesses a strong mode at 1153 cm^{-1}. This is fairly close in the frequency domain. However, in combination with the detection of the major modes 98 cm^{-1} or 106 cm^{-1} it should be possible to make the distinction between CHD and cZc-HT. Both frequencies are absent in CHD's eigenmode spectrum.

For CHD, mode 539 cm^{-1} might well indicate the passing of $\mathrm{CoIn}_{\mathrm{Min}}$, whereas its absence and a strong signal for mode 1401 cm^{-1} would hint at a reaction predominantly funneled through C_2-CoIn.

The Fourier amplitudes $c(\nu)$ computed, it is interesting to get first insight how the molecules might start to vibrate at either CoIn under the influence of those $c(\nu)$. The beating of all atoms relative to their equilibrium configuration $\boldsymbol{X}_{\mathrm{ref}}$ in groundstate CHD or cZc-HT expressed through $\Delta\boldsymbol{X}(t) := \boldsymbol{X}(t) - \boldsymbol{X}_{\mathrm{ref}}$ was computed according to

$$|\Delta\boldsymbol{X}(t)|^2 = \boldsymbol{c}^{\mathrm{T}} \cdot \left(\boldsymbol{\Theta}(t)^{\mathrm{T}} \cdot \boldsymbol{\Theta}(t)\right) \cdot \boldsymbol{c} \tag{1.9}$$

and is shown in Fig. 1.10. This time $\boldsymbol{X}(t)$ really refers to the molecule at time t.

CHD and cZc-HT behave differently (black curves). While CHD shows pronounced oscillatory motion dominated by a slow envelope, cZc-HT exhibits smaller oscillations due to lower relevant frequencies that are lying

closely together. For both molecules the C_2-symmetric case shows very rich features compared to the non-symmetric. These effects can be reproduced with the proper combination of only a few modes. The colored lines describe the molecular movement in terms of the selected dominant modes in tables 1.1a and 1.1b only. In all four situations the overall shape of $|\Delta \boldsymbol{X}(t)|^2$ is very similar, resulting from the dominant contribution of modes 196 cm^{-1} (CHD) and 184 cm^{-1} (cZc-HT) to the envelope.

However, if the evolution in Fig. 1.10 hints at the structure of a possible transient absorption measurement it will be very challenging to extract from it characteristic traces employable as feedback signals in an optimal control experiment. This will be difficult also for signals related to an autocorrelation-like quantity as simulated by $|\Delta \boldsymbol{X}(t)\Delta \boldsymbol{X}(0)|$ and displayed in Fig. 1.11. The very high time resolution required to reliably detect the small features expected is a major experimental challenge.

Summary of NMA of CHD's Ringopening In the preceding sections the reactive evolution of cyclohexadiene along two MEPs on the excited S_1-surface toward the groundstate was investigated. The focus was on how this evolution could be described in terms of normal modes belonging to the groundstate equilibrium structures of CHD and cZc-HT. The underlying idea was to determine the driving modes along the reaction path which still might be present as well as new modes activated at the path's ending when it returns to the ground state surface.

If these modes are extractable in transient absorption measurements, this information will verify and improve the microscopic understanding of the ringopening process and the potential energy surface employed for its description. Moreover, it opens the chance for employing a feedback signal in an optimal control experiment that selectively steers the molecule's reactive dynamics and influences a desired product's yield.

To determine the modes involved, normal mode analysis was developed. Using quantum chemically computed excited state configurations along the true MEP and a C_2-symmetry conserving MEP as static input information, it describes the molecule's route along these MEPs like a diffusive motion toward the two terminating conical intersections. It computes for all MEP positions investigated the projection coefficients $c(\nu)$ onto all the eigenmodes that are required for the formation of the specific nuclear arrangement. Dominant fingerprint modes are subsequently determined with the help of these results.

The findings of the investigation are: (1) So many eigenmodes are involved along both reaction paths that a pure normal mode simulation on several coupled potential energy surfaces will be numerically inefficient. However, this can be efficiently accounted for by employing reactive coordinates. On the other hand, normal modes are still invaluable to interpret the signal

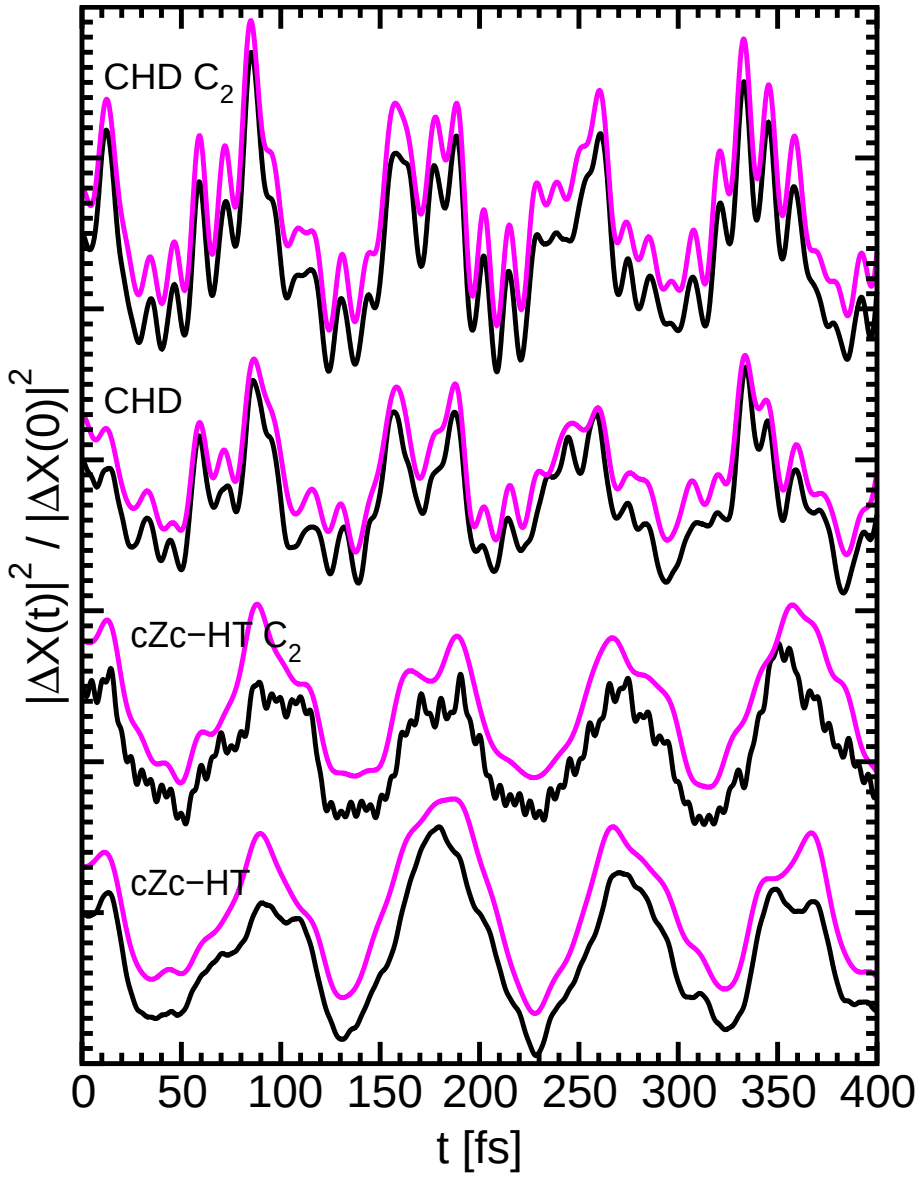

Figure 1.10: Evolution of vibrations. Starting at each of the two CoIns the normalized oscillations of all atoms around their groundstate equilibrium position are shown, see Eq.(1.9) and text. Colored lines denote the harmonic motion if the description is restricted to the modes given in table 1.1. For graphical clarity the rows have been offset.

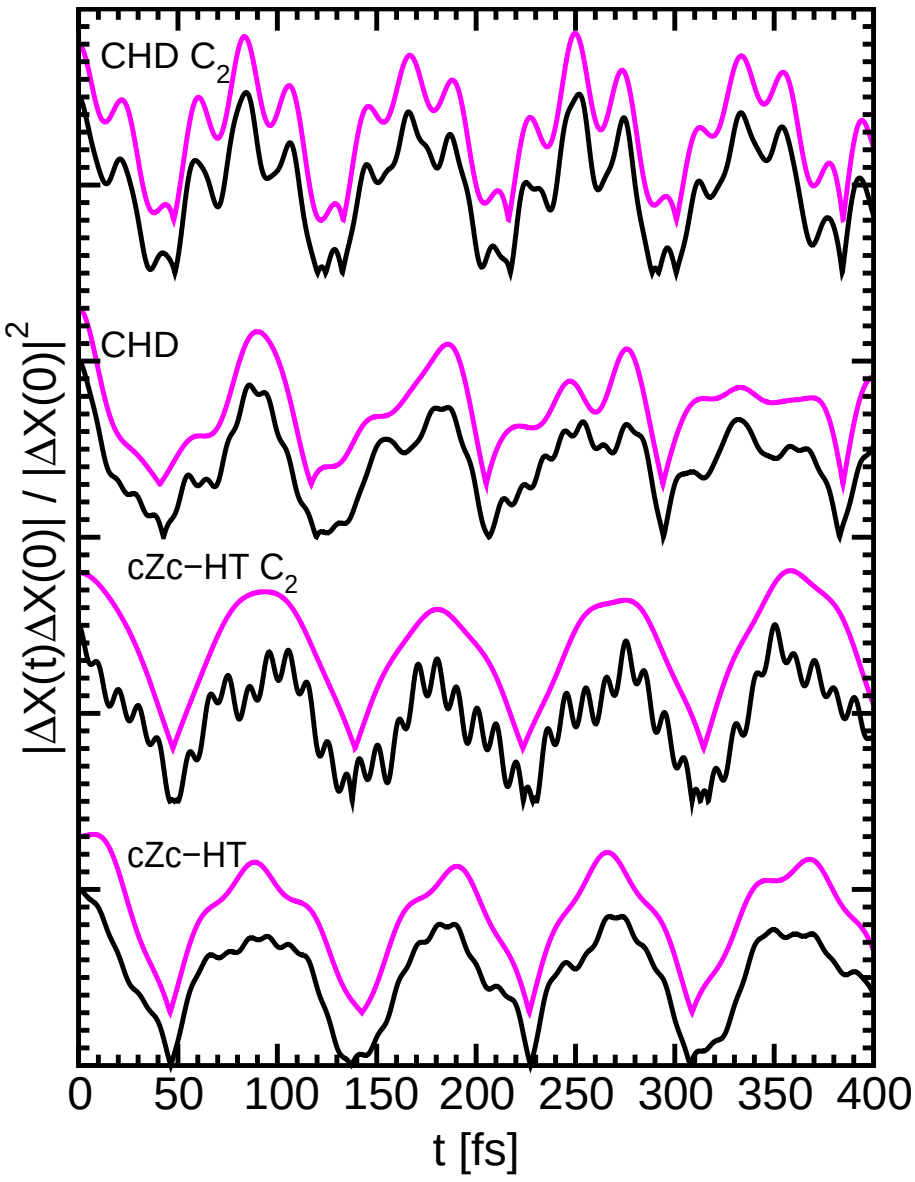

Figure 1.11: Similar to Fig. 1.10 but this time $\Delta \boldsymbol{X}(t)$ is compared to the initial excursion $\Delta \boldsymbol{X}(0)$. Colored lines again represent vibrations dictated by the few fingerprint modes selected in the tables 1.1a and 1.1b.

of, say, a transient absorption measurement. (2) Although experimentally challenging, several fingerprint modes were found to discriminate specific excited state mechanisms as well as specific products (CHD or cZc-HT, choice of a C_2-symmetric path or not). Their experimental detection would help to distinguish which conical intersection the molecule passed on its way toward the groundstate.

The most promising candidates found for CHD are modes 539 cm^{-1} and 1401 cm^{-1}, specific to either the minimal energy conical intersection $CoIn_{Min}$ or the C_2-CoIn. Both are among the strong modes along the two MEPs and both selectively indicate the CoIn passed by the excited molecule.

The situation is more complex for cZc-HT. There are several low lying eigenmodes available to pinpoint the CoIn passed by the molecule which unfortunately are energetically almost degenerate. Mode 1169 cm^{-1} does not encounter this problem and presumably is best suited for an experimentalist's needs. A minor problem is the neighboring CHD mode 1153 cm^{-1}, a combination with the detection of the strong cZc-HT modes 98 cm^{-1} or 106 cm^{-1} circumvents this difficulty.

Chapter 2

Normal Mode Analysis of the Protontransfer in 2-(2'-hydroxyphenyl)benzothiazole

Numerous studies are devoted to excited state intramolecular proton transfer (ESIPT) whose ultrafast dynamics are a challenge for spectroscopy as well as theory. Their better understanding requires and reveals insight into the interplay of structure, dynamics, and reactivity. Recent progress in time-resolved spectroscopy has demonstrated the possibility to observe highly localized wavepackets even in large molecular systems in condensed phase. In particular, ESIPT dynamics were studied in two-color pump-probe experiments with 25 fs pulses for 2-(2'-hydroxy-5'methylphenyl)-benzotriazole (TIN) [7] and 2-(2'-hydroxyphenyl)benzothiazole (HBT, depicted in Fig. 2.2) molecules [48, 61, 77]. The temporally and spectrally resolved stimulated emission of the keto type reaction product revealed coherent vibrational motion giving rise to a novel concept of the ESIPT driven by several well defined low-frequency modes.

To further support these findings the pump-probe studies with high temporal resolution on HBT in the group of E. Riedle[1)] were combined with the *ab initio* investigations of V. de Waele and R. de Vivie-Riedle. Due to the long lasting confinement of the experimentally observed wavepacket it is expected that the analysis along a quantum chemically computed reaction path should capture the characteristic features of the molecular evolution [77].

This is where normal mode analysis (NMA) comes into play. Employing quantum chemically computed normal modes and following a predicted reaction path NMA is able to connect the theoretical model for the reaction surface to experimental findings, thus verifying the consistent microscopical explanation for the ultrafast ESIPT dynamics.

[1)] Lehrstuhl für BioMolekulare Optik, Sektion Physik, LMU, München

These last two chapters devoted to normal mode analysis are organized as follows: In the subsequent section an introduction into the subject including the experimental findings and the resulting novel model of the ESIPT mechanism is provided. It is followed by a brief account of the quantum chemical computations for the structures and energies of the stationary configurations, for the minimum energy path, and for the two dimensional potential energy surface involved in the process. The Section 2.3 then exploits and combines these pieces of information by applying NMA to the ESIPT process. It finally concludes on NMA of HBT's ESIPT.

2.1 The Proton Transfer Reaction – Experimental Findings

The hydrogen transfer process in HBT occurs in the following fashion: After photo-excitation of the enol species the proton transfer occurs in the excited state in a ballistic fashion on a sub 100 fs timescale. It is followed by radiationless deactivation from the excited keto tautomer to the groundstate. A subsequent proton back-transfer closes the loop (see Fig. 2.2).

The experiments in the Riedle group were performed on HBT dissolved in cyclohexane with an 25 fs UV pump pulses of 347 nm center wavelength. The molecules were monitored by the observation of the transient transmission change in the wavelength range between 450 and 680 nm. Signals could be resolved with 30 fs temporal resolution. The observation of a large Stokes shift of 7 500 cm^{-1} with respect to the S_0-S_1 absorption band indicates that the molecule has undergone a significant rearrangement – the hydrogen transfer. This shift also confirms the transfer process taking place in the excited state.

A typical pump-probe trace at a detection wavelength of 502 nm is given in the central part of Fig. 2.1. In addition to the exponential decay it clearly shows persistent oscillatory contributions for more than 2 ps despite the solvent. A detailed analysis of the experimental signal allows for identifying four low frequency in-plane modes that perfectly fit the experimental data: 118 cm^{-1}, 254 cm^{-1}, 289 cm^{-1}, and 529 cm^{-1}. The frequency 254 cm^{-1} shows strongest signal contributions.

The experimental findings give rise to a new interpretation of the ESIPT mechanism [61]: After the $\pi\pi^*$ photoexcitation a tightening of the H-chelate ring occurs with the nitrogen and oxygen atoms moving closer together, tightly embracing the hydrogen. Halfway down the reaction path an electronic rearrangement toward the nitrogen sets in, and finally the ring releases its clasp on the proton and opens again partly. After this completion of the actual transfer within 60 fs the molecular frame has not yet arrived in its new excited keto equilibrium geometry. Having acquired considerable momentum along the reaction path the molecule starts vibrating coherently in

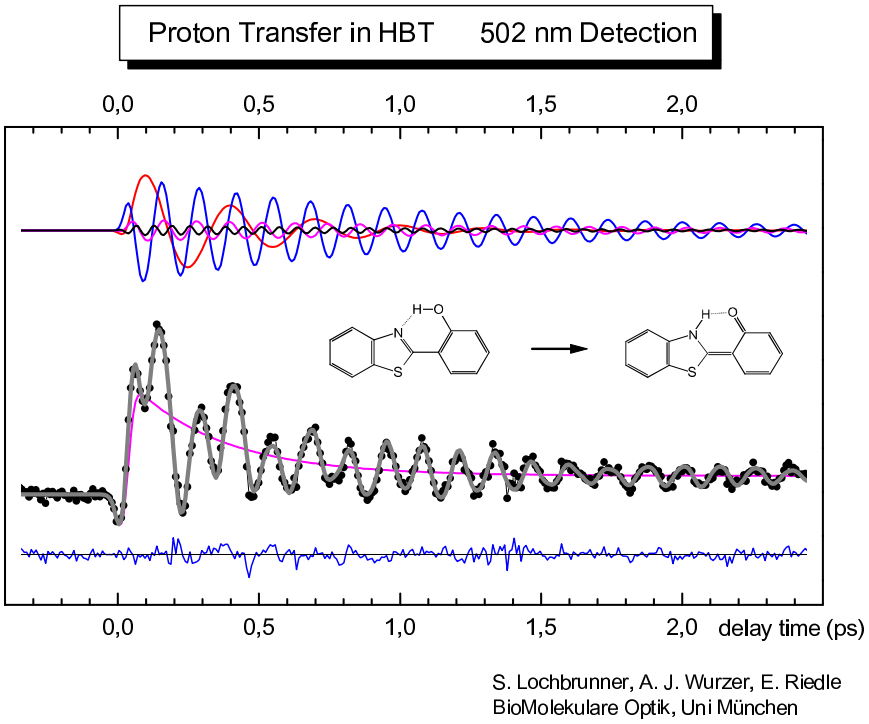

Figure 2.1: Time resolved transmission change (dots, center) for a 20 fs probe pulse at 502 nm induced by ESIPT after an excitation at 347 nm. In combination with the exponential decay (magenta) the remaining signal can be perfectly reproduced (grey line, center) with four low frequency modes 118 cm^{-1}, 289 cm^{-1}, 529 cm^{-1}, and a dominant contribution at frequency 254 cm^{-1} (top part). Only a negligible residuum remains (lowest curve).

four low-frequency modes corresponding to an in-plane deformation of the chelate ring. It is this coherent ringing of a wavepacket in the excited keto state that is monitored in the pump-probe signal.

It can be concluded that the interplay of electronic rearrangement in the excited state and the deformation of the entire molecule are the driving forces of the ultrafast excited state intermolecular proton transfer in HBT. It is not the proton itself that contributes significantly to the transferring process. The hydrogen merely follows adiabatically and the localized high-frequency OH or NH modes are not excited.

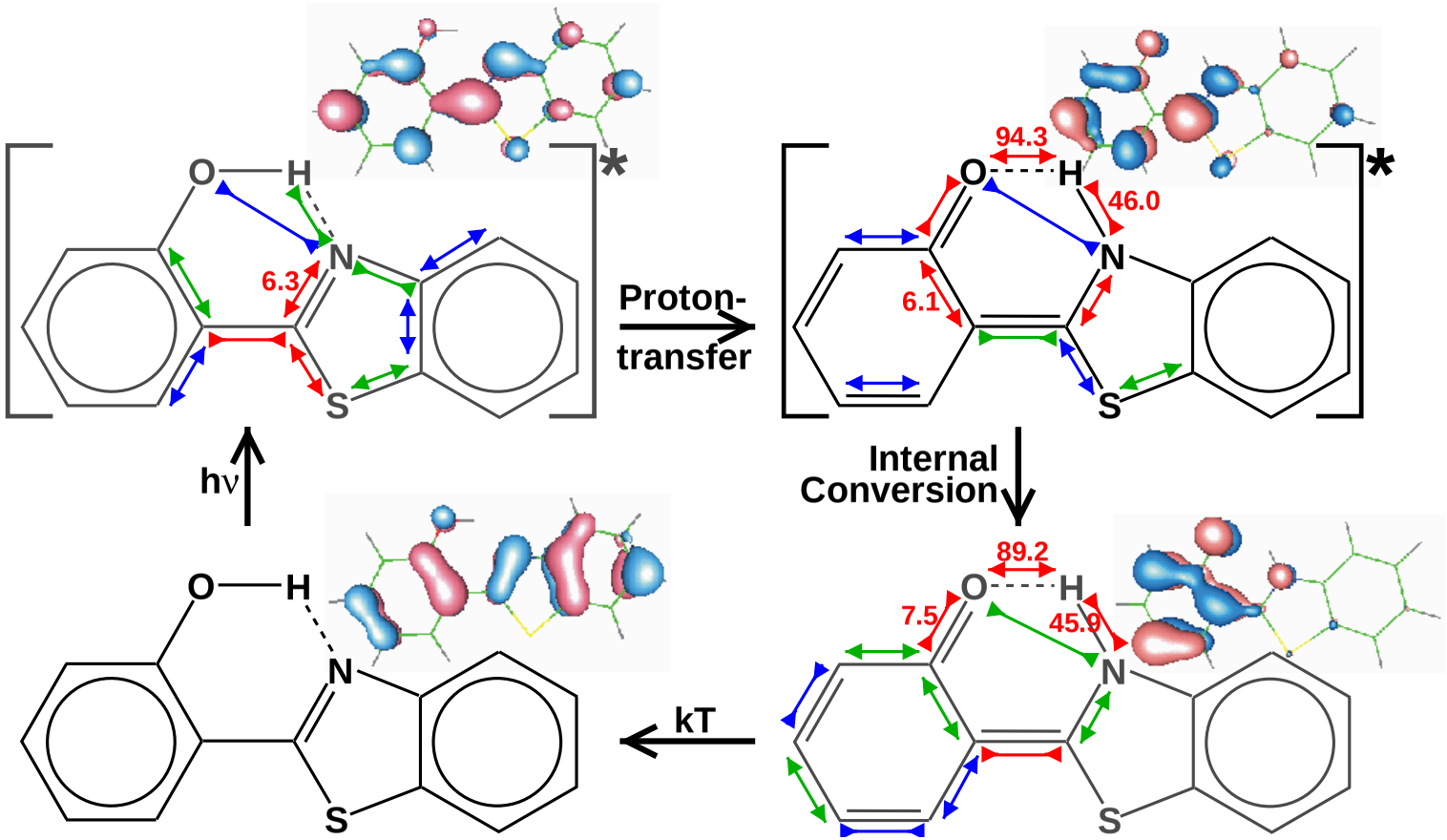

Figure 2.2: Sketch of the excited state intermolecular proton transfer in HBT. Given are the Lewis formulae of both tautomers with the less stable structures printed in grey. To indicate the molecular skeleton's distortions during the process dominant changes relative to the enol groundstate structure are highlighted (blue: 1.5-3.0%, green: 3.0-4.5%, red: 4.5-6.0%). Some relative changes are given explicitely. HOMO and LUMO orbitals are included to illustrate the electronic rearrangement during the H-transfer.

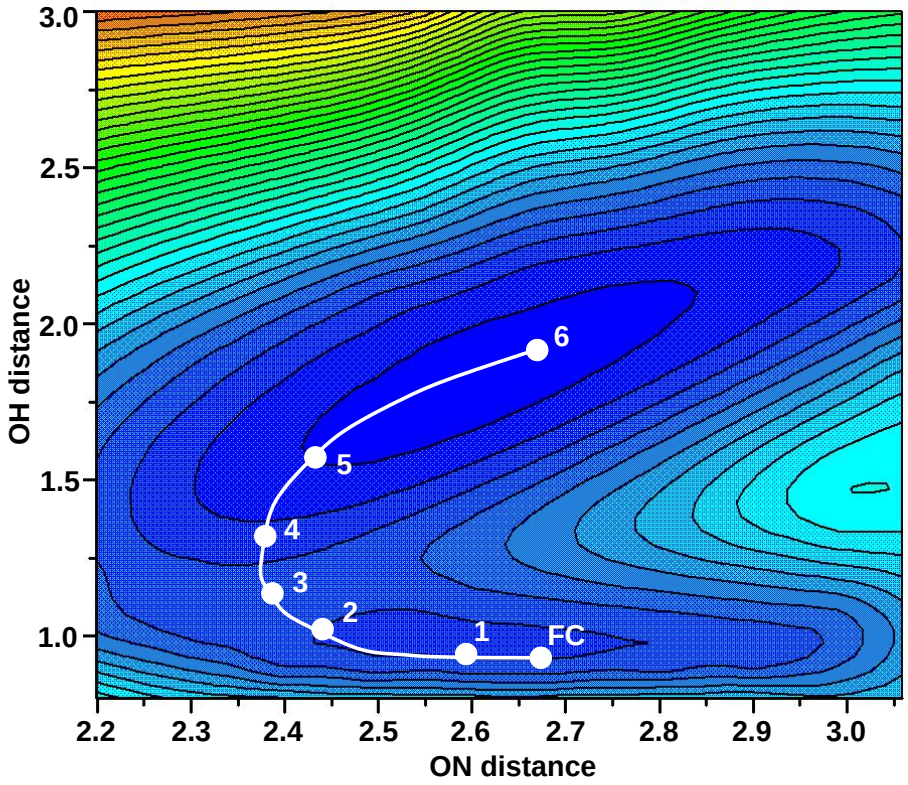

Figure 2.3: The 2-D S_1 reaction surface predicted for the ESIPT of HBT [9]. *Ab initio* calculations proved the ON and OH-distance (in [Å]) to be the relevant coordinates for describing the H-transfer. The reaction path (white line) connects the FC-region to the K^* configuration close to structure "6", passing the transition state "3". NMA results for the points FC, 1, 3, 5, and 6 follow in Chapter 2.3.

2.2 The *ab Initio* Reaction Surface

Extensive *ab initio* studies of the proton transfer process have been undertaken [9] to draw a consistent picture composed of the observed wavepacket motion and the structural and electronic evolution. This section summarizes briefly their major traits to elucidate the computational process leading to the two dimensional PES tailored to the ESIPT process. A detailed account will be given elsewhere [10].

First, the equilibrium structures of the HBT groundstate were optimized with Hartree-Fock (HF) [21, 22, 32] and Density Functional Theory (DFT) methods employing a 6-31G* basis and using the B3LYP functional. The lowest excited state S_1 of HBT was using the configuration interaction of single excitation (CIS) method starting from the HF-wavefunction. Geometries were optimized and the vibrational force field computed subsequently. Single point energy corrections were added with time-dependent DFT and

the B3LYP functional. Of similar logic were the computations of the minimum energy paths (MEPs) connecting the groundstate enol (E) to the keto (K) structure. The same applies for the excited state where E^* is connected to K^*.

The quantum chemical MEP studies in the ground and the excited state revealed the OH and NO distances on the S_1-surface to be the relevant proton transfer coordinates. Accordingly, a two dimensional PES has been computed. Since the reaction path sets off from the FC-region an unrelaxed PES in the OH and ON coordinate was computed with the help of CIS vertical transitions from a comparable relaxed groundstate surface. This reaction surface is presented in the Fig. 2.3.

Two valleys can be observed corresponding to the E^* (point 1) and the K^* excited tautomer (point 6), separated by a low barrier along the OH coordinate. A projection of the excited state MEP onto this surface is included as well. The normal mode analysis discussed in Chapter 2.3 will follow this path from the FC region to the keto minimum. Results will be given for the configurations "FC" and "1", for the transition state "3" on top of the barrier, and for points "5" and "6" in the vicinity of the excited keto minimum K^*.

2.3 Results and Discussion for the Protontransfer

For the equilibrium structures, their normal mode systems were determined as eingenvectors and eigenfrequencies of their Hessians. To adjust the calculated normal mode frequencies to the observed frequencies, *one* scaling factor 0.9 has been applied to *all* the modes' frequencies. Only the E^* and, above all, the K^* reference will be considered in NMA since the hydrogen transfer process occurs in the excited state.

The procedure follows the method outlined in Chapter 1.2. First, the x, y, z positions of all nuclei in HBT are combined in a 75-dimensional vector $\boldsymbol{X} = [\boldsymbol{q}_1^{\mathrm{T}}, \boldsymbol{q}_2^{\mathrm{T}}, \ldots, \boldsymbol{q}_{25}^{\mathrm{T}}]^{\mathrm{T}}$ and an equally long solution vector $\boldsymbol{C}$ is introduced. It will contain the projection coefficients onto the normal mode system. NMA derives $\boldsymbol{C}$ for the structural difference between the molecule's reference configuration $\boldsymbol{X}_{\mathrm{ref}}$ and one of the structures investigated along the reaction path via the matrix problem

$$\boldsymbol{X}_{\mathrm{ref}} - \boldsymbol{X}_{\mathrm{point}\ i} = \boldsymbol{\Theta} \cdot \boldsymbol{C} \ . \tag{2.1}$$

Compare to Eq.(1.2) on p.16. The two reference structures $\boldsymbol{X}_{\mathrm{ref}}$ will be the E^* and K^* tautomers. The two 75×75 matrices $\boldsymbol{\Theta}$ considered for HBT comprise all corresponding 69 vibrational eigenvectors as well as the translation of the center of mass and the rotation of the entire molecule to satisfy the Eckart conditions [12, 13]. With the algorithm outlined in Appendix B

residual translations and rotations between $\boldsymbol{X}_{\text{ref}}$ and $\boldsymbol{X}_{\text{point } i}$ are discarded, ensuring a solution vector with 69 entries $C(\nu)$ that describe vibrations only. The remaining six components are used as numerical indicators only, assuring negligible rotational and translational contributions.

The solution coefficients $C(\nu)$ for $\boldsymbol{X}_{\text{ref}} = \boldsymbol{X}_{\text{E}^*}$ are displayed in Fig. 2.4, those for $\boldsymbol{X}_{\text{ref}} = \boldsymbol{X}_{\text{K}^*}$ are given in Fig. 2.5. The panels are organized to follow the reaction path taken by NMA (cf. Fig. 2.3). This route sets off at the FC-region (top panel), passes by close to the excited enol structure (point 1), crosses the transition state (point 3), and proceeds toward point 6 in the vicinity of the excited keto-HBT tautomer. For comparison, panels showing the quantum chemically computed and rescaled mode frequencies of the E* (Fig. 2.4) and K* structures (Fig. 2.5) were added to the figures. From all possible modes only those are involved that retain the molecule's planar structure.

HBT's eigenmodes can be loosely arranged in three groups in energy space. Low frequency modes below 1000 cm^{-1}: They predominantly belong to long range vibrations involving the entire molecular backbone. These are also the modes accessible to the experiment due to available time resolution and laser energy [77]. Vibrations between 1000 cm^{-1} and 2000 cm^{-1}: These modes show an increasingly local deformation of the molecule that affects, for example, the benzene ring or the benzothiazole subgroup only. The mid-energy modes also lead to an enhanced motion of the hydrogen atoms attached to the skeleton. Finally, modes above 3000 cm^{-1}: Only few hydrogen atoms move but not the molecular backbone. Among them the highest mode (3210 cm^{-1} in the E* and 3266 cm^{-1} in the K* system) is in both cases extremely localized on the OH or NH relative motion. Other atoms in HBT do not participate.

Since the eigenmode system of E* as well as of K* are both complete they both can express all the MEP configurations equally well. However, from a physical point of view $\boldsymbol{X}_{\text{ref}} = \boldsymbol{X}_{\text{E}^*}$ after the photoexcitation of the enol species (Fig. 2.4). Many planar modes are found to be involved (structure FC) with a slightly larger contribution of few low energy vibrations. These amplitudes will shrink (point 1) and set in again around the transition state (point 3). From there on, the large amplitude of some dominant low-frequency modes will persist. Compared to them, modes in the mid-energy range 1000-2000 cm^{-1} show contributions that are smaller along the entire reaction path. In this region, characteristic features barely appear and one lacks distinct fingerprint modes. These medium-energy vibrations act like a background that shows little modulation apart from a light increase in amplitude beyond the transition state.

The high energy modes are not excited in the beginning. But after passing the transition state mode 3210 cm^{-1} will set in and show the largest $C(\nu)$ value of all modes in the end. However, this is only mathematical truth. In the reference experiment [61] the available laser energy is estimated

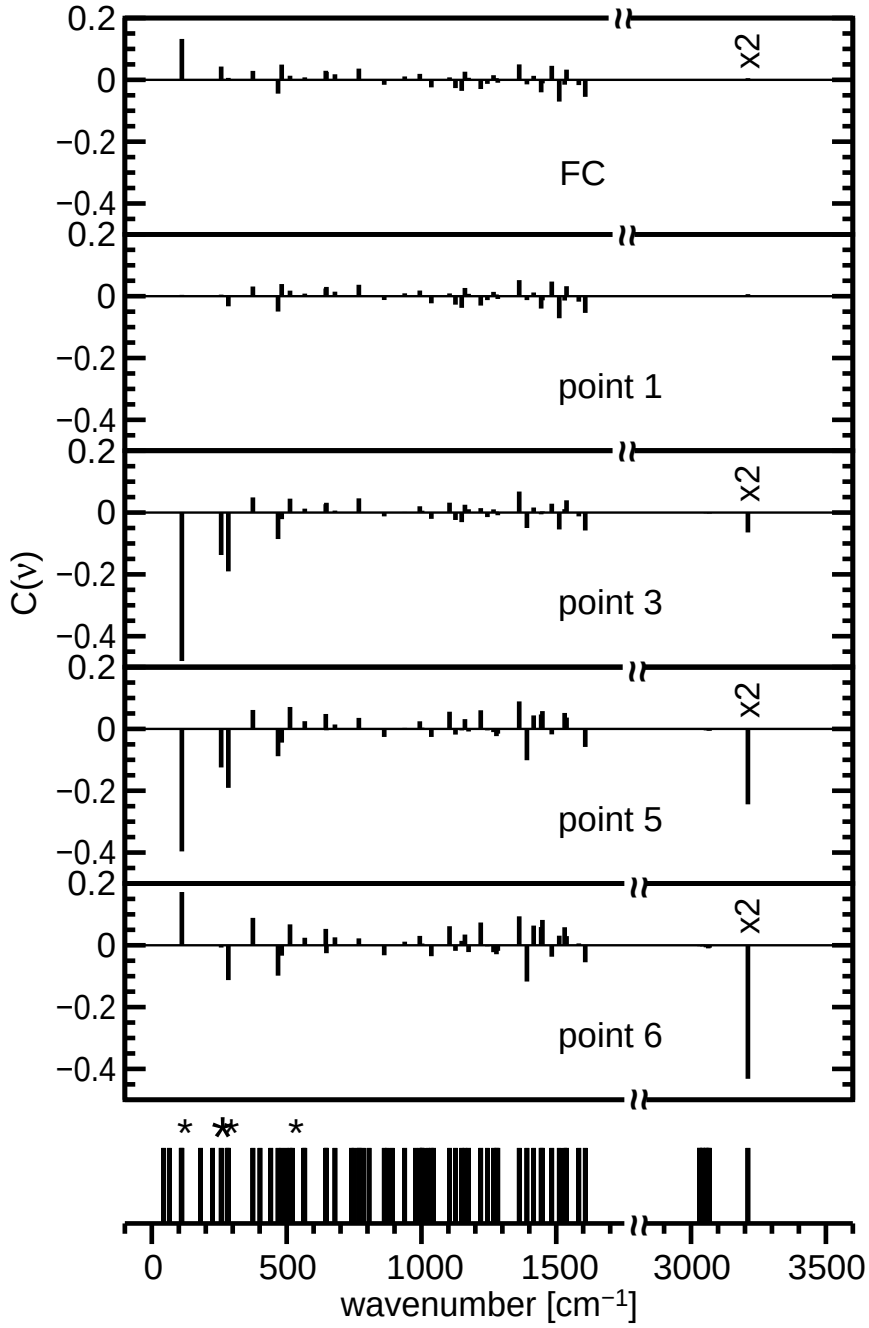

Figure 2.4: NMA along the predicted reaction path with respect to the excited enol-HBT equilibrium; given are the solution coefficients $C(\nu)$. For comparison all quantum chemically computed and rescaled normal mode frequencies are shown as stick spectrum in the lowest part. Stars indicate modes closest to the experimentally observed frequencies; i.e. in pairs $(\nu_{\text{ex.}}, \nu_{\text{theo.}})$: (118 cm^{-1}, 111 cm^{-1}), (289 cm^{-1}, 283 cm^{-1}), (529 cm^{-1}, 512 cm^{-1}), and the experimentally strongest signal at (254 cm^{-1}, 257 cm^{-1}), marked by a larger star. Please note the discontinuous frequency axis. The highest mode requires rescaling by a factor of 2 to regain the correct result.

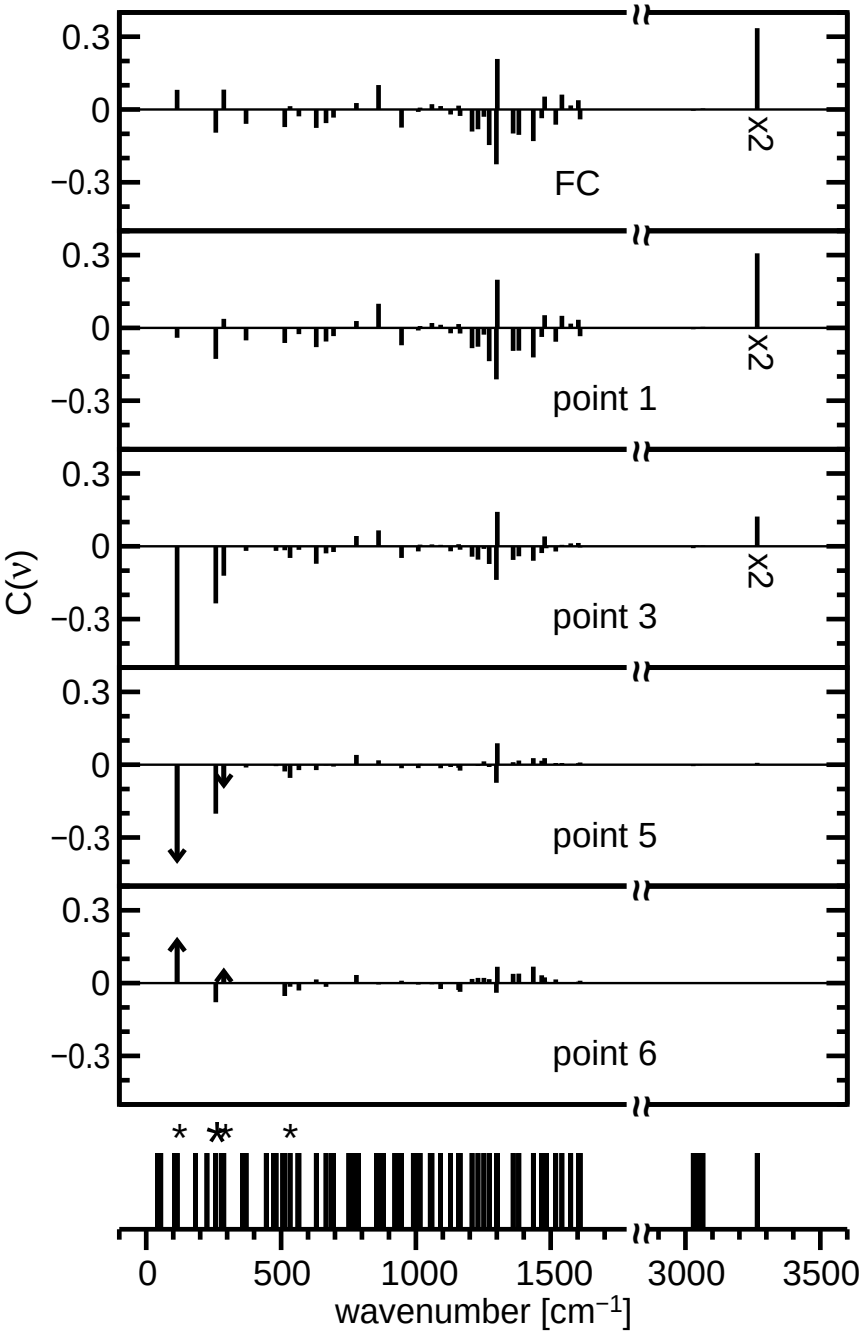

Figure 2.5: NMA with solution coefficients $C(\nu)$ along the reaction path with respect to the K* equilibrium structure. The computed normal mode frequencies are given in the bottom row for comparison. Stars point out modes that are close to the experimentally observed frequencies. In the keto modes system these are $(\nu_{\text{ex.}}, \nu_{\text{theo.}})$: (118 cm^{-1}, 114 cm^{-1}), (289 cm^{-1}, 288 cm^{-1}), (529 cm^{-1}, 533 cm^{-1}), and the experimentally strongest signal at (254 cm^{-1}, 258 cm^{-1}), marked by a larger star. Compare to Fig. 2.4 and the text for details.

around 2 500 cm^{-1}. Hence the OH mode cannot be excited and it is not able to participate in the actual proton transfer process.

The generally increasing $C(\nu)$ values in all modes beyond the transition state indicate that point 3 also must be considered a transition point in mathematical terms. Beyond it the wavepacket has no meaningful physical representation in terms of E^* eigenvibrations and to extract reasonable dynamical information the switch to $\boldsymbol{X}_{\mathrm{ref}} = \boldsymbol{X}_{K^*}$ is required (Fig. 2.5).

The behavior of the medium and high energy modes in the E^* system is directly opposed to their behavior in the K^* system, which will be discussed now. In this case the higher modes evolve from large amplitudes in the FC region down to small $C(\nu)$ values in the vicinity of the keto-like structure around point 6. The true equilibrium excited state keto-HBT configuration is not observed in the computation. It would yield a solution vector $\boldsymbol{C} = \boldsymbol{0}$. This equilibrium keto structure must be situated in the vicinity of point 6 in the direction toward point 5. The passing of a minimum also must be the reason for the sign inversion of some low frequency contributions (marked by arrows): Traveling down the reaction path the wavepacket acquires momentum, traverses the PES well, and continues toward a point of reflection. This comparable to the beating of the wavepacket observed in the experiment. Since not all amplitudes show this sign reversal, configuration 6 must be slightly off the direct line connecting point 5, the PES minimum, and such a point of reflection.

While the medium and high energy modes of the excited enol and keto reference behave opposed to each other this is not the case for low frequency modes. For the E^* and K^* reference few dominant low energy vibrations are initiated in passing transition state point 3. The *ab initio* computation revealed that while there are larger differences in the normal mode systems of E^* and K^* in the medium and high-energy regime there are large similarities in the low frequency range. Modes comparable in frequency are also comparable in the skeleton's motion.

The observed dominant low energy vibrations are: Mode 114 cm^{-1}, featuring a scissors-like motion of the chelate ring; mode 258 cm^{-1}, a stretch along the central CC bond connecting the phenol ring to the benzothiazole structure; mode 288 cm^{-1}, performing a scissors-like motion of the chelate ring as well. Mode 533 cm^{-1}, closest to the experimental value 529 cm^{-1}, would be expected also but showed only small $C(\nu)$ values throughout the computation. However, this eigenmode and its neighboring vibration 513 cm^{-1} display a minute – physical or computational – interplay along the reaction path (Fig. 2.5). In both modes a waving motion is observed in which the hetero atoms are leaning toward each other. They thus facilitate the closure of the chelate ring and enhance the proton's transfer. In general, the frequencies of both modes are so similar that it is certainly difficult to resolve them experimentally. Hence, one presumably measures an average contribution of both.

Summary of NMA of HBT's ESIPT Photoexcitation of groundstate enol HBT leads to the excitation of several low and mid-energy modes that involve the entire molecular skeleton. All participating vibrations conserve the molecule's planar structure. Passing the transition state few low-energy modes dominate and form an oscillating wavepacket around the excited state keto equilibrium structure. High-energy modes that are local to the attached hydrogen atoms do not contribute. This supports the idea that the proton is not the active player in the transfer process. It is rather carried along by the motion of the entire skeleton actived by passing the transition state. An active role of the hydrogen would necessitate the large contribution of high-frequency modes which NMA can rule out for the transferring process.

There is good agreement between the computed fingerprint modes and the data extracted from the wavepacket's beating in the experiment. Moreover, computations not only reveal the modes' frequencies to coincide with the experiment but the modes' motion also is consistent with the actual transferring process and its novel model outlined in Section 2.1: In concurrence with a concerted electronic rearrangement the chelate ring tightly embraces the proton first and relaxes subsequently. Its opening leading to the OH-bond cleavage and HN-bond formation with the proton sticking to the nitrogen. This is followed by a relaxation of the molecular structure toward the excited keto tautomer. The echo of the chelate ring motion is then detected as the ringing of the modes in the experiment.

Chapter 3

Summary and Outlook for Part I

The preceding chapters dealt with NMA as a *direct* means to connect *local* characteristics of a computationally derived reaction surface for ultrafast processes to the normal mode beating of a molecular wavepacket observed in an experiment.

NMA was developed for predicting signatures of experimental traces associated to the ringopening process of cyclohexadiene. Determining fingerprint modes helps to understand the ultrafast reactive process and provides access to controlling it. Several indicator modes were identified leading to suggestions for feedback signals in an optimal control experiment that aims at steering the molecule selectively through two distinct conical intersections and influences the product yield.

In contrast to this predictive nature, the other half of the NMA investigation was devoted to a system that already had been subject to an experiment. In the excited state intramolecular proton transfer in HBT normal mode analysis further supports a novel model of the ESIPT process. The results obtained are in good agreement with experimental findings. A transfer mechanism driven by a single high-frequency mode could be rule out. This was achieved by employing a recently developed detailed 2-D reaction surface on which NMA followed a proposed reaction path.

In general, it can be concluded that NMA is an efficient tool that is applicable to reactions whose dynamics are well described by confined wavepackets that follow a clearly identifiable reaction path.

Part II

Extracting Reaction Surfaces Globally

Chapter 4

A Novel Extraction Scheme

The final part of the thesis turns toward an *inverse* method connected to molecular reaction surfaces. To this end, an algorithm is introduced that is capable of extracting the potential energy surface *globally* from the in principle experimentally observable quantity $|\psi(x,t)|^2$.

4.1 Introduction

To fully understand chemical dynamics phenomena it is necessary to know the underlying potential energy surfaces (PES) [45]. Surfaces can be obtained by two means: *ab initio* calculations [4, 21, 22, 32, 65] and the inversion of suitable laboratory data [15, 30, 33, 34, 50, 51, 73, 79]. This part is concerned with an emerging class of laboratory data [29, 63, 78] with special features for inversion purposes. Traditional sources of laboratory data for inversion produce an indirect route to the potential requiring the solution of Schrödinger's equation [62] in the process. An alternative suggestion [80, 81] has been put forth to utilize the ultrafast probability density data from diffraction observations or other means [2, 39, 41, 43, 72, 74] to extract adiabatic potential surfaces. Such data consists of the absolute square of the wavefunction. Although the phase of the overall wavefunction is not available, there is sufficient information in this data to extract the potential fully quantum mechanically *without* the solution of Schrödinger's equation. Instead, the proposed procedure rigorously formulates the inversion algorithm as a linear integrodifferential equation utilizing Ehrenfest's theorem [14] for the position operator. Additional attractive features of this algorithm are (a) the procedure may be operated non-iteratively, (b) no knowledge is required of the molecular excitation process leading to the data and (c) the regions where the potential may be reliably extracted are automatically revealed by the data.

Extensive efforts are under way to achieve the necessary temporal and spatial resolution of the probability density data required for inversion pro-

cesses as well as for other applications [80]. In anticipation of these developments a number of algorithmic challenges remain to provide the means to invert such data. Part II of this thesis aims to introduce into and build on the previous work [81] and address some of these needs. In particular it will consider (i) optimal choices for regularizing the inversion procedure, (ii) incorporation of multiple data sets and (iii) inclusion of data sampled at discrete time intervals. These concepts are developed and illustrated for the simulated inversion of a double well and a Morse potential.

Part II is organized as follows: The basic inversion procedure and the model systems are introduced in Chapter 4.2. Based on the inversion algorithm derived in Ref. [81] an extended regularization procedure is presented in Chapter 5 followed by a discussion of a modified time integration scheme applicable to different types of experimental data sampling in Chapter 6. This development naturally leads to consideration of an optimal combination of data from different measurements. A proof on how to optimally combine the data is supplied in Appendix C. The stability of this data combination procedure under the influence of noise is discussed as well and additional material is provided in Appendix D. Chapter 7 summarizes the findings of this part and offers suggestions for future work.

4.2 The Basic Inversion Procedure and the Model Systems

The algorithms developed in this paper will be illustrated for a one-dimensional system but the generalization to higher dimensions is straightforward [82]. The major difference with higher dimensions is the additional computational effort. Atomic units are used throughout.

For a system whose dynamics is governed by the Schrödinger equation

$$\mathrm{i}\frac{\partial}{\partial t}\psi(x,t) = \left[-\frac{1}{2m}\frac{\partial^2}{\partial x^2} + V(x)\right]\psi(x,t) \tag{4.1}$$

the time evolution of the average position obeys Ehrenfest's theorem

$$0 = m\frac{\mathrm{d}^2}{\mathrm{d}t^2}\int x\,\rho(x,t)\,\mathrm{d}x + \int u(x)\,\rho(x,t)\,\mathrm{d}x\;, \tag{4.2}$$

where $u(x) := \mathrm{d}V(x)/\mathrm{d}x$ and $\rho(x,t) := |\psi(x,t)|^2$. The probability density $\rho(x,t)$ is assumed to be observed in the laboratory and the goal is to determine the potential energy surface (PES) $V(x)$ from the gradient $u(x)$.

Following [81], Eq.(4.2) can be used to construct a Gaussian least squares minimization problem to determine the PES gradient $u(x)$

$$J_0\{u(x)\} := \frac{1}{T}\int_0^T \left[\int u(x)\,\rho(x,t)\,\mathrm{d}x + m\frac{\mathrm{d}^2}{\mathrm{d}t^2}\int x\,\rho(x,t)\,\mathrm{d}x\right]^2 \mathrm{d}t\;. \tag{4.3}$$

The time averaging acts as a filtering process to increase inversion reliability by gathering together more data and reducing the ill-posedness of the problem. This increase is in principle only limited by the exploratory ability of the wavepacket. Beyond some point in time little information on the potential may be gained by taking further temporal data starting from any initial condition.

Variation with respect to $u(x)$ results in a Fredholm integral equation of the first kind

$$\frac{\delta J_0\{u(x)\}}{\delta u(x)} \stackrel{!}{=} 0 \quad \Rightarrow \quad \int A(x',x)\, u(x')\, \mathrm{d}x' = b(x) \tag{4.4}$$

with righthand side (RHS)

$$b(x) := -\frac{m}{T} \int_0^T \rho(x,t)\, \frac{\mathrm{d}^2}{\mathrm{d}t^2} \int x'\, \rho(x',t)\, \mathrm{d}x'\, \mathrm{d}t \tag{4.5}$$

and symmetric, positive semidefinite kernel

$$A(x',x) := \frac{1}{T} \int_0^T \rho(x',t)\rho(x,t)\, \mathrm{d}t\ . \tag{4.6}$$

Treated as an inverse problem, Eq.(4.4) produces the desired PES gradient $u(x)$ as its solution. For numerical implementation the matrix version and its formal solution

$$\boldsymbol{A}\cdot\boldsymbol{u}\,\Delta x = \boldsymbol{b} \quad \Rightarrow \quad \boldsymbol{u} = \boldsymbol{A}^{-1}\cdot\boldsymbol{b}\,\Delta x^{-1} \tag{4.7}$$

is employed. Here, the integral in Eq.(4.4) is evaluated at points of constant spacing Δx.

In the numerical evaluation of Eq.(4.5) the second order time derivative of the position average was computed by applying the accurate second order differencing scheme twice. This scheme is defined for a function $f(x)$ via

$$\frac{\mathrm{d}}{\mathrm{d}x} f(x) = \frac{f(x+\Delta x) - f(x-\Delta x)}{2\Delta x} + O(\Delta x^3)\ . \tag{4.8}$$

Although less accurate, the boundary terms at $t = 0$ and $t = T$ have been computed in each step with single-sided differentials to not loose data points. For the evaluation of spatial and temporal integrals the NAG-routine **d01gaf** has been utilized. It is designed for numerically integrating (discrete) functions over a finite range, which are sampled at four or more points. Using third-order finite-difference formulae with error estimates developed in [31] it can also cope with irregularly grided data.

The actual inversion process in Eq.(4.7) was performed through singular value decomposition (SVD) (consult [53, 64] for an overview) with NAG-routine **f04jgf**. Various methods to solve linear problems are available and SVD is certainly not the fastest. However, it is very stable and can cope with non-invertible matrices as well. In that case it returns the least-squares solution. Hence, it can also be employed to test the inversion performance without regularization.

The above approach in Eq. (4.4) to seeking the PES has a number of attractive features [81]. The formulation requires no knowledge of any preparatory steps to produce a specific $\psi(x,0)$ which evolves freely to yield $\rho(x,t)$. Moreover, although this is a fully quantum mechanical treatment there is no need to solve Schrödinger's equation to extract the PES. The generation of $A(x,x')$ and $b(x)$ depends only on $\rho(x,t)$ and begins when the observation process is started. The dominant entries of $A(x,x')$ and $b(x)$ automatically reveal the part of the PES that will be reliably extracted and the linear nature of Eq.(4.4) is very attractive from a computational perspective.

Notwithstanding these attractions, a principal problem to manage is the generally singular nature of the kernel of the integral equation in Eq.(4.4). The wavepacket can only explore a portion of the PES, and it is not possible to continuously monitor the wavepacket with arbitrary accuracy. Hence the $\boldsymbol{A}$-matrix will always have a nontrivial nullspace. The resulting solution $u(x)$ will only be reliable in regions where the wavepacket has significant magnitude during its evolution. This is demonstrated for the unregularized inverse solution of the Morse configuration $\mathrm{M_u}$ in Fig. 5.5b with corresponding $V(x)$ in Fig. 5.5c.

The inversion procedure can manage the null space with the help of a suitable regularization procedure. Truncated singular value decomposition as well as truncated iterative solution schemes are available (cf. [49, 53] for an overview), but here extended Tikhonov regularization will be employed (see Chapter 5).

The procedures developed in this thesis are applied to a simulated inversion with a system taken to have a slightly asymmetric double well potential [11]

$$V(x) = \frac{\Delta}{2q_0}(x-q_0) + \frac{\hat{V}-\Delta/2}{q_0^4}(x-q_0)^2(x+q_0)^2 + \Delta \tag{4.9}$$

with parameters

$$q_0 = 1.0 \tag{4.10a}$$
$$\Delta = 0.000\,257 \quad \text{(asymmetry)} \tag{4.10b}$$
$$\hat{V} = 0.006\,25 \quad \text{(barrier height)}\,. \tag{4.10c}$$

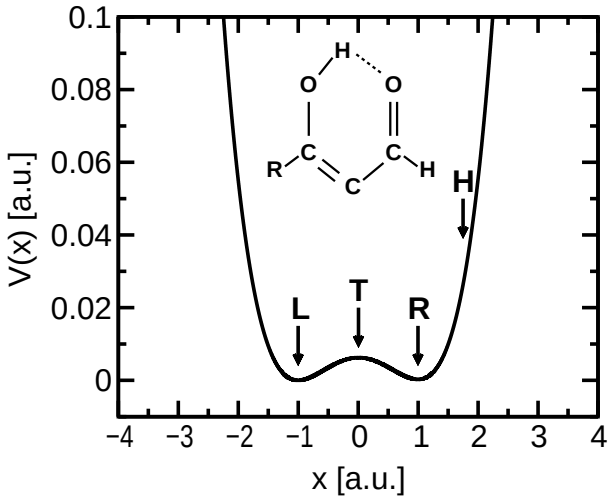

Figure 4.1: The substituted malonaldehyde model system with its corresponding one dimensional potential energy function $V(x)$ as given in Eq.(4.9). L, T, R, H indicate the different wavepacket initial positions utilized for the simulated inversions.

In the work of N. Došlić *et al.* [11] this PES represents a one dimensional model for the intramolecular proton transfer in substituted malonaldehyde (see Fig. 4.1). The particle mass is accordingly that of hydrogen.

The wavepacket propagations to obtain the simulated $\rho(x,t)$ data employed the split operator method [16, 17]. For propagation as well as inversion we used a grid with 8192 points over the range $-4.0 \leqslant x \leqslant 4.0$. A time step $\Delta t_{\text{prop}} = 3$ was chosen and total propagation time was $T = 1200$. The small values of Δt_{prop} and Δx_{prop} ensured good convergence of the numerical propagation procedure.

The initial wavefunctions were normalized Gaussian wavepackets of width $\sigma = 0.05$. As stated earlier, the inversion algorithm requires no knowledge of how these packets were formed, but generally one may assume that a suitable external laser field was applied for times $t < 0$. The initial packets were placed at the left (L) and right minimum (R) of the PES, on top of the barrier (T), and at a location high on the potential (H). The wavepacket positions are illustrated in Fig. 4.1 and their exact values, the associated average energies and the classical turning points at these energies are given table 4.1.

The inversion process employed a timestep and grid spacing that differed from those used in the propagation, as high spatial and temporal resolution is difficult to attain in the laboratory. Hence, only a portion of all the available propagation data $\rho(x,t)$ in time and space was employed. Inversion results are presented using every 16th propagation grid point (i.e. $\Delta x = 16 \cdot \Delta x_{\text{prop}}$) and every fifth available propagation snapshot (i.e., $\Delta t = 5 \cdot \Delta t_{\text{prop}}$).

Configuration index	x_0	$\langle\psi_0\|H\|\psi_0\rangle$	classical turning points: left	right
H	1.75	0.081	-2.1563	2.1534
R	0.9977	0.055	-2.0013	1.9978
T	0.0052	0.061	-2.0403	2.0370
L	-1.002	0.054	-1.9996	1.9961

Table 4.1: Characteristics of the initial wavepackets in the malonaldehyde system. The configuration indices are used throughout the text. All wavepackets start with equal width $\sigma = 0.05$ and are initially at rest centered at the respective starting position x_0. The average energy of each packet as well as the corresponding turning points of an equivalent classical particle of equal energy are given.

To further test the inversion's performance and to compare to the original work [81], the simulated inversion of the potential energy function of O-H has been investigated also. The following Morse potential [51]

$$V(x) = D_0 \left[\mathrm{e}^{-\beta(x-x_0)} - 1 \right]^2 - D_0 \,, \tag{4.11}$$

with parameters

$$\beta = 1.189 \tag{4.12a}$$
$$D_0 = 0.1994 \quad \text{(dissociation energy)} \tag{4.12b}$$
$$q_0 = 1.821 \quad \text{(equilibrium distance)} \tag{4.12c}$$

describes the O-H bond [52]. The different tests on this system will be referred to as "M" with a characteristic index.

Propagation with the help of the split operator method was performed for a particle with mass $m = 1742.5106$ from $t = 0$ to $T = 340$ with the timestep $\Delta t_{\mathrm{prop}} = 2.0$ on a grid $0.1 \leqslant x \leqslant 16.484$ with 8192 points. The initial normalized Gaussian wavepackets were at rest and have the same width as in the double well system. Results are given for a configuration in which the initial packet sets off at $x_0 = 1.0$, representing a highly excited O-H dissociating rapidly. As for the double well inversion only a portion of all available ρ-data is employed. In the O-H system again $\Delta x = 16 \cdot \Delta x_{\mathrm{prop}}$ but this time $\Delta t = 2 \cdot \Delta t_{\mathrm{prop}}$. For both systems the inversion results from these lower resolution data are very encouraging.

The kernel matrices $\boldsymbol{A}$ for the double well condition H and T are shown in Fig. 4.2; similar plots apply to the cases L and R as well as the O-H system. The kernels are symmetric with values covering a large dynamic range from $\sim 10^3$ down to 10^{-8} on the plotted domain. Significant entries

are found predominantly on the matrix diagonal, close to the origin of the wavepacket, and also in the vicinity of the classical turning points. Beyond the classical turning points at distances of approximately ± 2.0 the kernel values fall off very rapidly since the wavepacket barely enters these areas.

The features of the kernel in Fig.4.2 coincide with the nature of the inverse problem mentioned earlier: symmetry, ill-posedness, and definition of the range where the PES may be be reliably extractable (i.e., where the kernel entries are large). For configuration H the relevant range is $-2 \lesssim x \lesssim 2$ and for configuration T only the vicinity of the barrier top should yield reliable PES information. In both cases reasonable solutions cannot be expected beyond ± 2.0, which coincides with the classical turning points given in table 4.1.

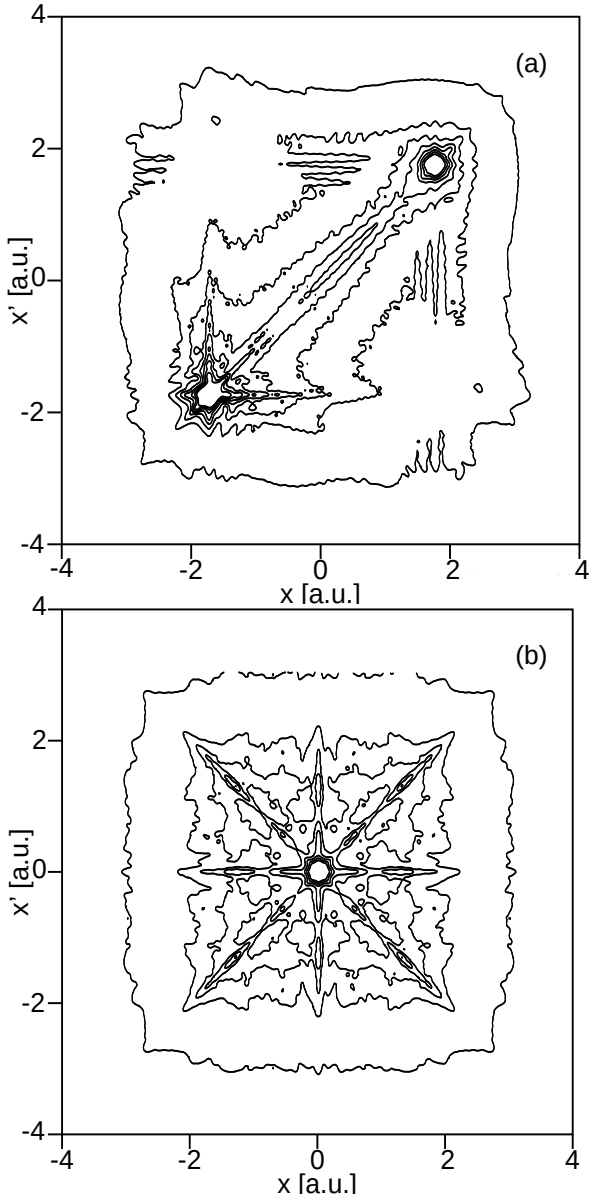

Figure 4.2: Contour plots of two kernel matrices $\boldsymbol{A}$ in the double well system. Comparable features can be observed for the Morse potential also. Panel (a) shows configuration H and panel (b) configuration T. The numerical values for the matrix entries range from $\sim 10^3$ on the diagonal to $\sim 10^{-8}$ on the boundaries. The contour levels correspond to: 1 (outer line), 31, 61, ... , 211.

Chapter 5

Improved Regularization

Tikhonov regularization [68] is straightforward to implement with simple control provided by suitable weight parameters. It provides a well defined means to stabilize the inversion and extract reliable PES information in those regions allowed by the data. This investigation goes beyond the initial work [81] to carefully explore various regularization options.

Regularization has the goal of improving the accuracy of the solution, assuring stability and ease of use including computational simplicity. To this end the functional J_0 was augmented by a regularization term involving a set of increasingly higher order differential operators acting on $u(x)$

$$J_1\{u(x)\} := J_0\{u(x)\} + \sum_{\nu=0}^{N} \alpha_\nu \xi^{-1} \int \left[\left(\xi \frac{\mathrm{d}}{\mathrm{d}x} \right)^\nu u(x) \right]^2 \mathrm{d}x \ , \tag{5.1}$$

with real coefficients $\alpha_\nu > 0$ and a reference length ξ. In practice ξ may be thought of as the spatial resolution of the data and in the present numerical simulation it was taken as Δx. For a multidimensional system, ξ and α_ν will become direction dependent tensors. The parameter ξ acts to ensure that all the new terms added to J_0 have the same units as $[u]^2$ as well as permits comparison of the roles of the dimensionless regularization parameters α_ν for different ν and different grid spacings Δx. Previous work [81] did not employ a reference length as only the $\nu = 0$ regularization term was considered with α_0 penalizing the value of $u(x)$. The new terms go beyond this order and impose extra pressure on the gradient ($\nu = 1$), the curvature of $u(x)$ ($\nu = 2$), etc..

Variation of J_1 with respect to $u(x)$ yields the modified inversion prescription

$$\int \left[A(x', x) + \delta(x - x') \cdot \sum_{\nu=0}^{N} \alpha_\nu \xi^{-1} \left(-\xi^2 \frac{\mathrm{d}^2}{\mathrm{d}x'^2} \right)^\nu \right] u(x') \, \mathrm{d}x' = b(x) \ . \tag{5.2}$$

The sum added to J_0 in Eq.(5.1) for regularization consisted of purely positive terms with derivatives of up to Nth order, now results in an alternating series of only even derivatives up to order $2N$ in Eq.(5.2). Moreover, the Fredholm integral equation of first kind has changed into an integro-differential equation for $u(x)$ with the added terms dominating in the regions where the kernel is singular.

Due to the rapid growth in the order of the derivatives it is often sufficient to set $N = 2$, i.e., retaining standard, gradient, and curvature Tikhonov regularization. For numerical application Eq.(5.2) may be transformed into the matrix problem[1)]

$$\left[\boldsymbol{A} + \alpha_0 \Delta x^{-2}\, \mathbb{1} - \alpha_1\, \boldsymbol{D} + \alpha_2 \Delta x^2\, \boldsymbol{Q}\right] \cdot \boldsymbol{u}\, \Delta x = \boldsymbol{b}\,, \tag{5.3}$$

employing the unit matrix $\mathbb{1}$, as well as the second

$$\boldsymbol{D} := \frac{1}{(\Delta x)^2} \begin{bmatrix} -2 & 1 & & & 0 \\ 1 & -2 & 1 & & \\ & \ddots & \ddots & \ddots & \\ & & 1 & -2 & 1 \\ 0 & & & 1 & -2 \end{bmatrix}, \tag{5.4}$$

and the forth order differentiation band matrices

$$\boldsymbol{Q} := \frac{1}{(\Delta x)^4} \begin{bmatrix} 6 & -4 & 1 & 0 & & & & \cdots & 0 \\ -4 & 6 & -4 & 1 & 0 & & & & \vdots \\ 1 & -4 & 6 & -4 & 1 & 0 & & & \\ 0 & 1 & -4 & 6 & -4 & 1 & 0 & & \\ \vdots & \ddots & \ddots & \ddots & \ddots & \ddots & \ddots & \ddots & \end{bmatrix}. \tag{5.5}$$

These are simple differencing expressions for the derivatives involved. Higher order expressions for the derivatives could be considered, but finite data resolution and laboratory noise will generally not warrant or support the added complexity.

To investigate the inverse solution's dependence on the various regularization parameters α_ν in Eq.(5.3), several parameter scans for all four double well configurations L, T, R, H and for the Morse potential were performed for different resolutions[2)] Δx and combinations of α_ν-parameters. Typical results were selected for the double well situations H and L as well as the Morse PES. The discussion will focus on the double well situation H first.

The curves in Figs. 5.1, 5.2, and 5.4 show the solution defect $|\Delta u|$ and the system defect $|\Delta s|$ as defined below in Eqs.(5.6) and (5.9). While only

[1)] Its dimension [length^{-1}] necessitates $\delta(x - x') \to \delta_{ij}/\Delta x$ if employing the matrix formulation.

[2)] On the issue of different inversion resolutions Δx consult Appendix D.2.

Configuration	α_1	x_a	x_b	$\lvert\Delta u\rvert \times 10^{-3}$	$\lvert\Delta s\rvert \times 10^{-3}$
H_1	3.3×10^{-5}	-4.0	4.0	384.58	0.03
H	1.0	-2.0	2.0	11.52	23.46
R	0.033	-1.5	1.5	7.16	1.06
T	0.007	-1.5	1.5	9.02	0.05
L	0.033	-1.5	1.5	6.53	1.07
Σ	100.0	-1.5	1.5	9.53	111.63
LTRH	0.333	-1.5	1.5	3.83	12.42
LTR	0.01	-1.5	1.5	2.78	0.70
LT	0.01	-1.5	1.5	3.10	0.49

Table 5.1: Inversion regularization information for the malonaldehyde system. The optimal regularization parameter value α_1 was identified by scanning its effect on the solution defect $|\Delta u|$. The inversion domains are $x_a \leqslant x \leqslant x_b$. $|\Delta s|$ is the system defect. The first five rows apply to the individual PES reconstructions shown in Fig. 5.3, and the last four rows refer to measurement combinations shown in Fig. 6.1. See the text for details.

$|\Delta s|$ is an experimentally accessible figure of merit, an investigation of $|\Delta u|$ here allows for quantifying the quality of the inverse solution. For both error measures reported, the plots are generated for each α_ν independently while the others are kept zero.

In panels (a) and (b) of Fig. 5.1 the solution defect

$$|\Delta u| := \left[\frac{1}{x_b - x_a}\int_{x_a}^{x_b} \left(\, u_{\text{exact}}(x) - u(x)\,\right)^2 \,\mathrm{d}x\right]^{1/2} \tag{5.6}$$

of configuration H is displayed. Figure 5.1a is computed with $x_a = -2.0$, $x_b = 2.0$ (i.e. the central domain indicated by the classical turning points in in Fig. 4.2a and table 4.1 within which the inversion is expected to be valid) and Fig. 5.1b with $x_a = -4.0$, $x_b = 4.0$ (i.e., the full simulation range). The differences between the two cases are striking: The corresponding solution defects show a completely different shape with minima that differ by several orders of magnitude in α_ν. In Fig. 5.1b the magnitude of the error in the active domain is overestimated. This behavior is due to large deviations between the exact gradient and the inversion solution for the gradient, which cannot recover the correct values at the domain's outer limits. Thus it can be concluded that $|\Delta u|$ scans should only be computed over the regions actually reached to a significant degree by the wavepacket (cf., Fig. 5.1a) to achieve reliable estimates of the inversion quality.

The latter point is illustrated in Figs. 5.3b and 5.3c for the purely α_1 regularized inversion of configurations H/H_1 with α_1 given in table 5.1. The

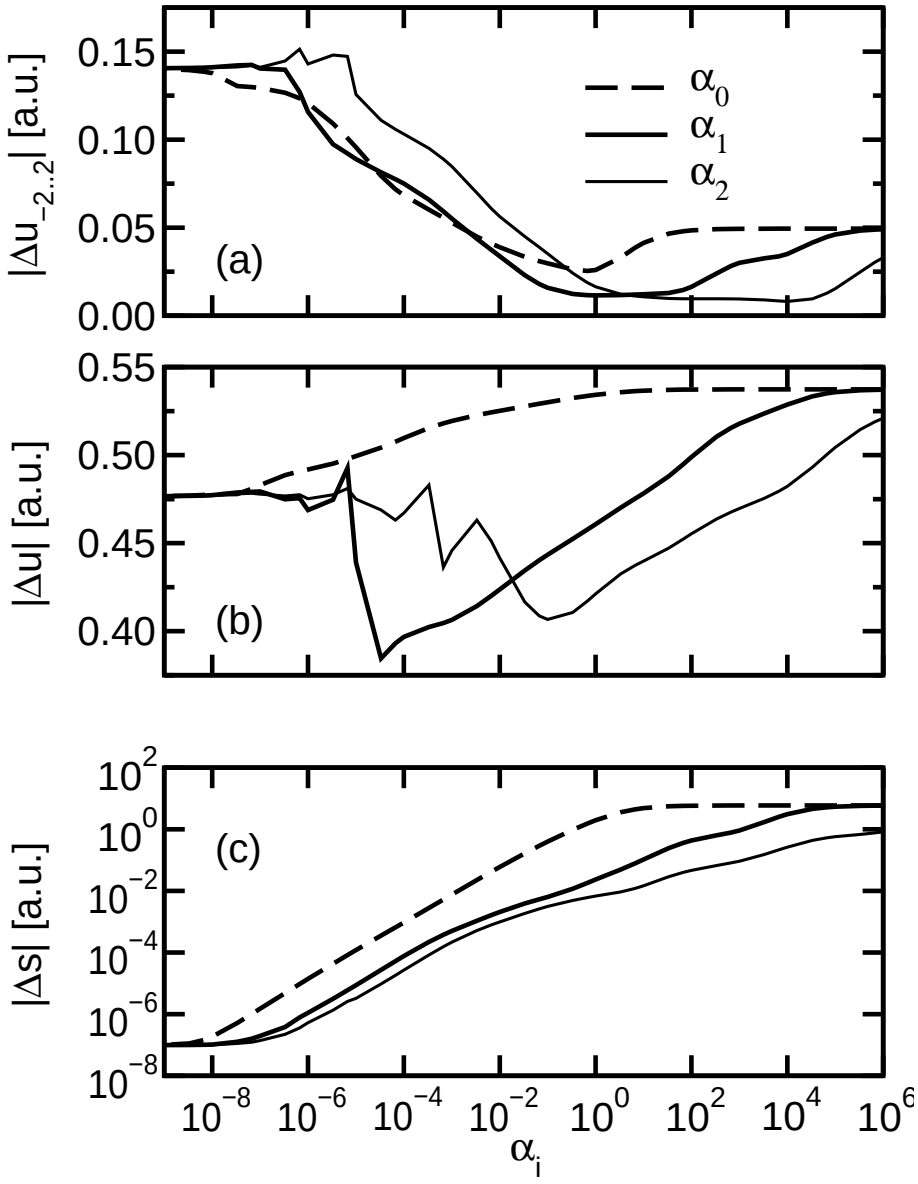

Figure 5.1: α_ν parameter scan performed with configuration H. Panels (a) and (b) display the solution defect $|\Delta u|$ with respect to two different inversion ranges: $-2 \leqslant x \leqslant 2$ and $-4 \leqslant x \leqslant 4$, respectively. Panel (c) shows the system defect $|\Delta s|$ for the entire domain $-4 \leqslant x \leqslant 4$.

two cases H/H$_1$ differ in the domain employed (i.e., the active domain for H and the full domain for H$_1$) to choose an optimal α_1, determined according to the $|\Delta u|$ scans. Thus it is further concluded that the inversion process should be confined to the active domain to maintain stability.

To find suitable inversion domains from the laboratory data the normalized lefthand

$$\sigma_\ell^2(t) := \int_{-\infty}^{\langle x\rangle} (x - \langle x\rangle)^2 \rho(x,t)\,\mathrm{d}x \Bigg/ \int_{-\infty}^{\langle x\rangle} 2\rho(x,t)\,\mathrm{d}x \tag{5.7}$$

and righthand variance

$$\sigma_\mathrm{r}^2(t) := \int_{\langle x\rangle}^{\infty} (x - \langle x\rangle)^2 \rho(x,t)\,\mathrm{d}x \Bigg/ \int_{\langle x\rangle}^{\infty} 2\rho(x,t)\,\mathrm{d}x \tag{5.8}$$

of the position operator can be helpful. The normalization is chosen in such a way that the usual variance is recovered[3)], i.e., $\sigma^2(t) = \sigma_\ell^2(t) + \sigma_\mathrm{r}^2(t)$ for symmetric probability density distributions $\rho(x + \langle x\rangle, t) = \rho(x - \langle x\rangle, t)$. Together with the position average $\langle x\rangle$ these two quantities can provide an estimate for the PES domain predominantly covered by the wavepacket motion. All three quantities ($\langle x(t)\rangle$ and $\sigma_\ell(t), \sigma_\mathrm{r}(t)$ as grey shaded regions) are presented in Fig. 5.3a. The results clearly show that for configuration H the range $-2 \lesssim x \lesssim 2$ is suitable. For configurations L, T, R an even smaller range is best (cf., table 5.1).

These results are supported by the findings for all the other configurations L, T, and R as well as the Morse potential. Some of the additional information is presented in Fig. 5.2 for situation L and in Fig. 5.4 for the OH system. In the latter case, the reliable inversion domain covered by the wavepacket motion is $1.0 \lesssim x \lesssim 8.0$. Table 5.2 presents optimal α_1-parameters found after $|\Delta u|$ scans. Corresponding inverse solutions $u(x)$ and their PES $V(x)$ are displayed in Fig. 5.5.

All the computations revealed that a gradient Tikhonov regularization based on α_1 generally performs better than the standard regularization based on α_0 utilized earlier [81]. There is some additional improvement in choosing the curvature regularization α_2, but it was found to be less stable for coarse grids, which will be the standard situation in actual application.

There also is little improvement in mixing the different regularization schemes. In general the α_ν regularization with the largest errors masks the positive effects of the others. Hence for all cases of the PES reconstruction presented only the generally best performing α_1 regularization was utilized

[3)] Depending on the situation in question the extra normalization could be dropped in favor of the standard relation $\sigma^2(t) = \sigma_\ell^2(t) + \sigma_\mathrm{r}^2(t)$ for arbitrary ρ.

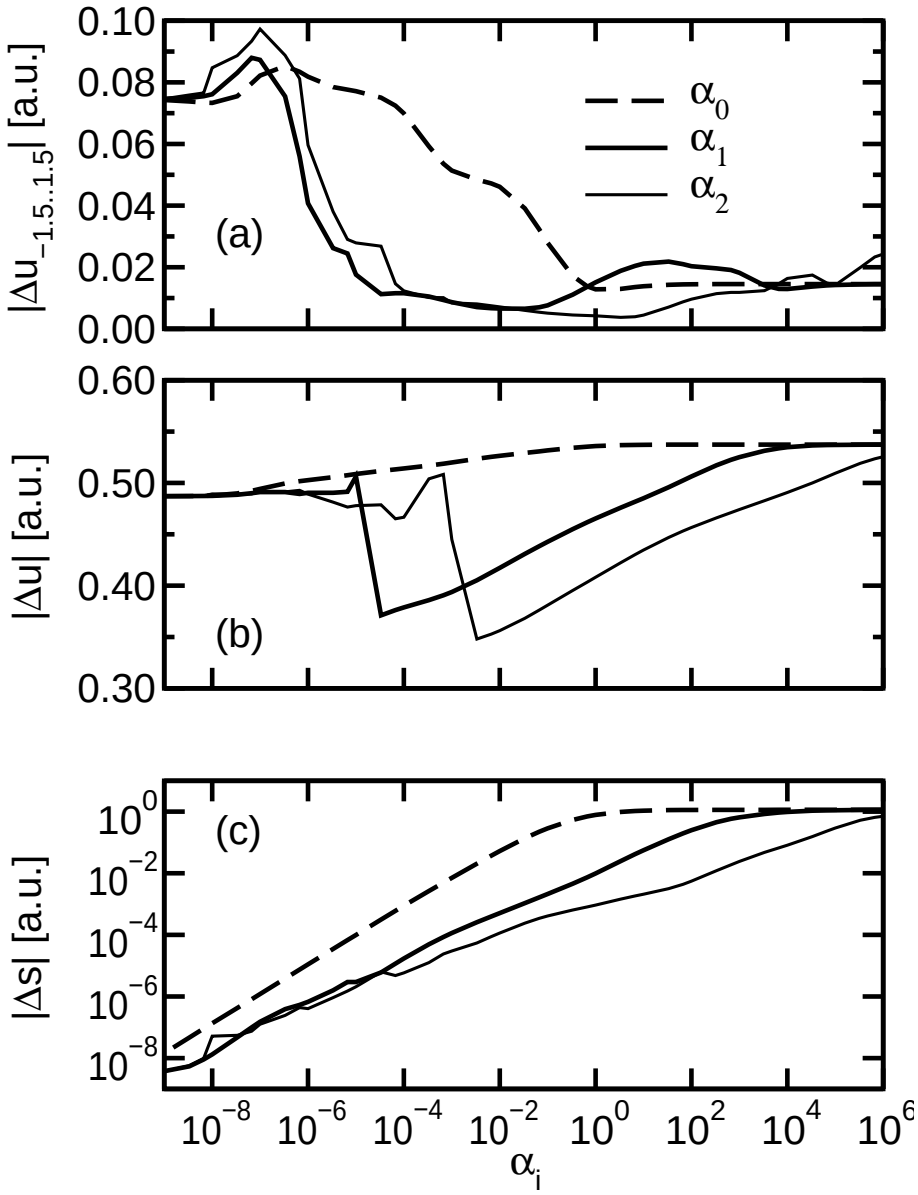

Figure 5.2: α_ν parameter scan performed with malonaldehyde configuration L. The two top panels display $|\Delta u|$ with respect to the inversion range $-1.5 \leqslant x \leqslant 1.5$ in (a) and $-4 \leqslant x \leqslant 4$ in (b). Panel (c) explores the system defect $|\Delta s|$.

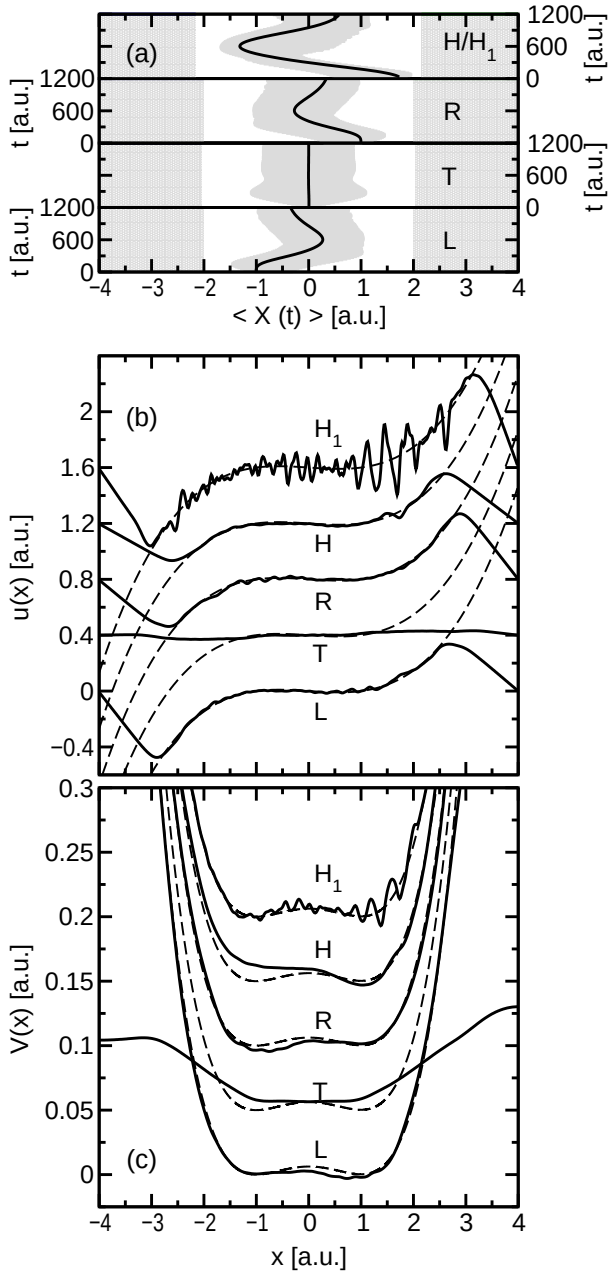

Figure 5.3: Extractions of the potential under the conditions given in table 5.1. Panel (a): The time evolution of the position average $\langle x(t)\rangle$ accompanied by the left- and righthand normalized variances (i.e., the shaded areas determined by Eqs.(5.7) and (5.8)) to indicate the regions predominantly covered by the probability densities. The grey domains on the extreme left and right mark classically forbidden areas (cf. table 4.1). Panel(b): The reconstructed gradient $u(x)$ and the corresponding potential $V(x)$ in panel (c). For comparison the exact solutions are included as dashed lines. The individual curves have been offset for graphical reasons and the presentation of $V(x)$ is restricted to $|x| \lesssim 2.5$ since the boundary regions will not be extracted correctly due to the lack of data sampling there.

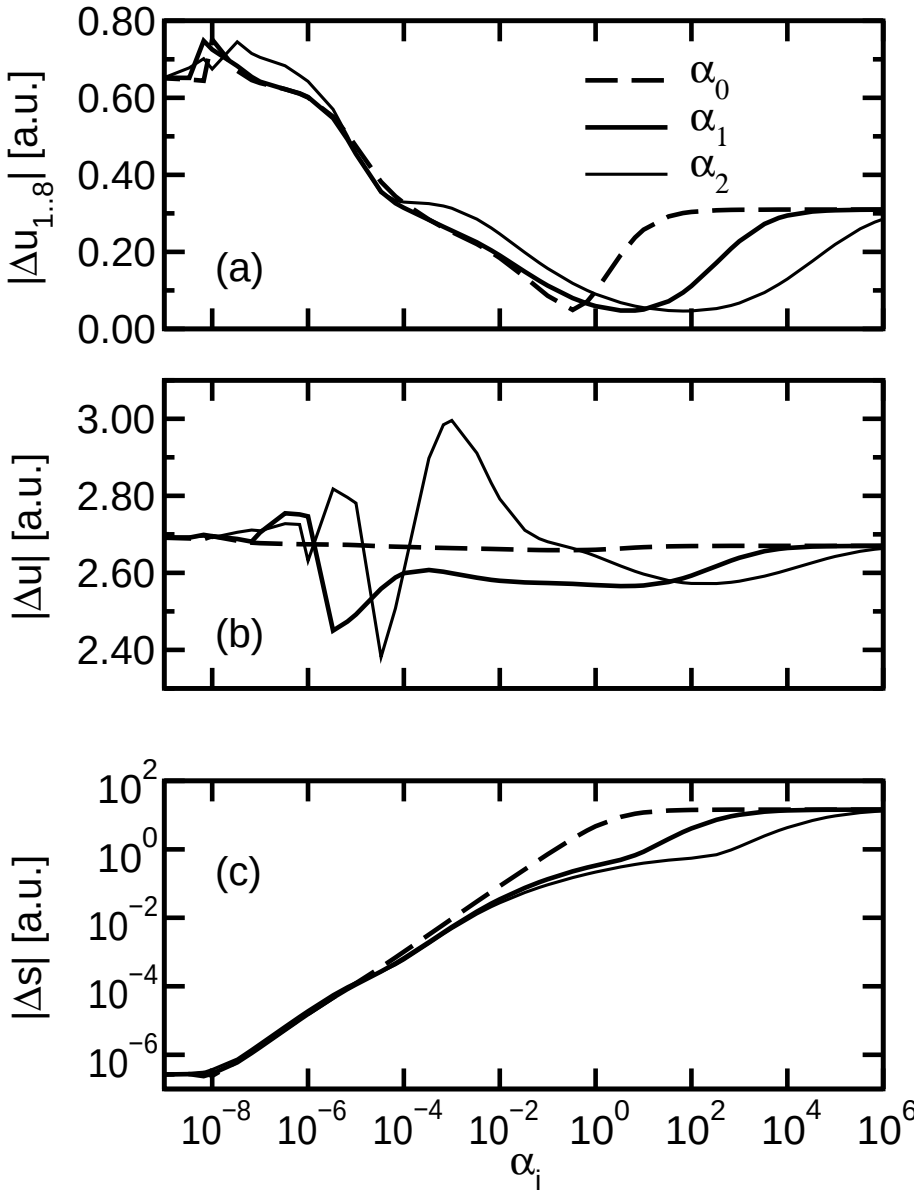

Figure 5.4: An α_ν parameter scan computed for the O-H Morse system. The solution defect $|\Delta u|$ is shown with respect to the reliable inversion range $1.0 \leqslant x \leqslant 8.0$ (a) and the entire range $0.1 \leqslant x \leqslant 16.484$ (b). Panel (c) displays the system defect $|\Delta s|$ for $0.1 \leqslant x \leqslant 16.484$.

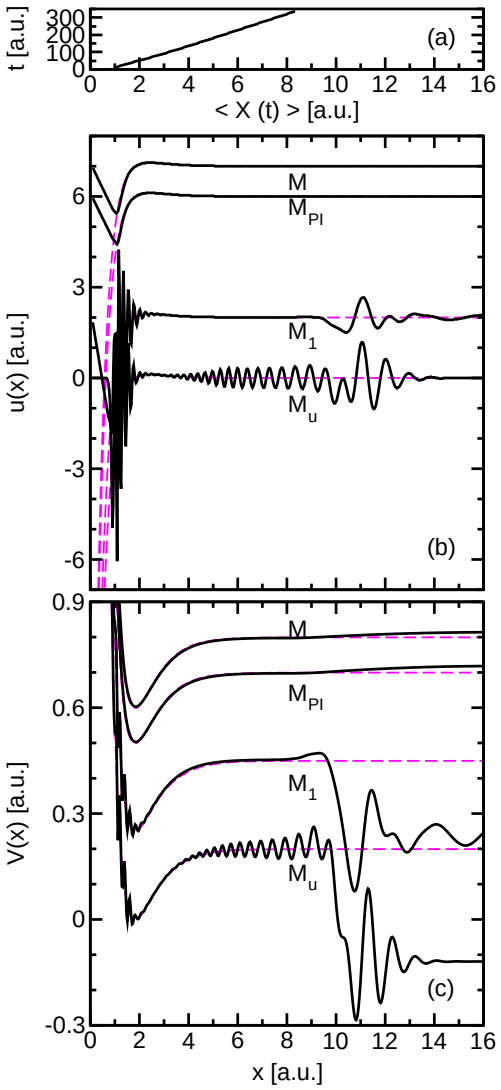

Figure 5.5: Extractions of the Morse potential with α_1 regularization (see table 5.2). (a) area covered by the wavepacket motion $1 \lesssim x \lesssim 8$ illustrated by the time evolution of the average position $\langle x(t) \rangle$. (b) reconstructed $u(x)$ and the corresponding potential $V(x)$ in (c). The individual curves have been offset for graphical clarity and exact solutions (colored dashed lines) were added for comparison. An additive constant was suitably chosen for $V(x)$ to make exact and reconstructed curves coincide. M: optimal α_1-parameter chosen according to Fig. 5.4a; $\mathrm{M_{PI}}$: employing partial integration for $b(x)$ (cf. Appendix D.1); $\mathrm{M_1}$: α_1-parameter chosen for the too large inversion domain in Fig. 5.4b; M_u: unregularized inversion.

Configuration	α_1	x_a	x_b	$\lvert\Delta u\rvert \times 10^{-3}$	$\lvert\Delta s\rvert \times 10^{-3}$
M_1	3.3×10^{-6}	0.1	16.484	254.00	465.70
M	6.667	1.0	8.0	47.69	671.51
M_{PI}	6.667	1.0	8.0	49.86	804.22
M_u	0.0	1.0	8.0	652.41	2.6×10^{-4}

Table 5.2: Inversion regularization information for the Morse potential, compare to table 5.1. The optimal regularization parameter value α_1 was identified by a parameter scan on $|\Delta u|$ with domain $x_a \leqslant x \leqslant x_b$. $|\Delta s|$ is the system defect. The rows apply to the different PES reconstructions shown in Fig. 5.5.

(see the inversions in Figs. 5.3 and 5.5 with the optimal parameters given in tables 5.1 and 5.2).

As a measure of inversion quality and the role of regularization, a quantity is desired that is strictly available from the laboratory data $\rho(x,t)$. A good choice is the system defect $|\Delta s|$ defined by the norm of satisfying the system equation (4.4) with the inverse solution $u(x)$ found via Eq. (5.2)

$$|\Delta s| := \left[\frac{1}{L}\int\left(b(x) - \int A(x,x')u(x')\,\mathrm{d}x'\right)^2 \mathrm{d}x\right]^{1/2} . \tag{5.9}$$

The values of $|\Delta s|$ will depend on the regularization parameters α_ν. Weak regularization will produce a small value of $|\Delta s|$, but likely artificial structures in the PES. Over regularization will result in a smooth PES, that is systematically in error but with a diminished influence from the kernel $A(x,x')$ on the inverse solution. The best choice for the α_ν is generally where $|\Delta s|$ has risen and leveled off in a stable region as shown in Fig. 5.1c, for example. The figure shows that $|\Delta s|$ naturally tends to zero as $\alpha_\nu \to 0+$ and monotonically rises until it reaches a plateau. There is very good agreement between the values of α_ν which show good results for $|\Delta u|$ in Fig. 5.1a and the stable regularization region identified in Fig. 5.1c. Thus $|\Delta s|$ should be of practical utility in assigning regularization parameter values.

The generally self-similar structures in Figs. 5.1a and 5.1c suggest that every regularization operator has a roughly similar effect. This added robustness is also attractive for practical application if it holds up regardless of the system. This issue and further, more technical details that should help in actual application are dealt with in Appendix D.

Chapter 6

Combining Distinct Sets of Laboratory Data

This chapter will cover different approaches to combining distinct sets of laboratory density data in Sections 6.1 and 6.2. Finally, Section 6.3 will explore the impact of data noise on the inversion.

6.1 Optimal Combination of Experimental Data

The functional $J_0\{u(x)\}$ in its original form in Eq.(4.3) has been formulated in terms of a uniform, continuous time integration of observed $\rho(x,t)$ data. However, experimental circumstances including measurements at discrete snapshots in time or changes in the quality of data sampling may necessitate employing a weight function $\omega(t)$ for a generalized approach to the time integration in the functional J_0. Thus a modified functional $\hat{J}_0$ is defined as

$$\hat{J}_0\{u(x)\} := \int_0^\infty \left[m\frac{\mathrm{d}^2}{\mathrm{d}t^2} \int x\,\rho(x,t)\,\mathrm{d}x + \int u(x)\,\rho(x,t)\,\mathrm{d}x \right]^2 \omega(t)\,\mathrm{d}t\ . \tag{6.1}$$

The choice $\omega(t) = [\,\Theta(t) - \Theta(t-T)\,]/T$, with the Heaviside step function Θ, will reduce $\hat{J}_0$ to J_0.

Variation of Eq.(6.1) leads to a modified inverse problem

$$\frac{\delta \hat{J}_0\{u(x)\}}{\delta u(x)} \stackrel{!}{=} 0 \quad \Rightarrow \quad \int \hat{A}(x',x)\,u(x')\,\mathrm{d}x' = \hat{b}(x)\ , \tag{6.2}$$

with the new kernel

$$\hat{A}(x',x) := \int_0^\infty \rho(x',t)\rho(x,t)\,\omega(t)\,\mathrm{d}t \tag{6.3}$$

and RHS

$$\hat{b}(x) := -m \int_0^T \omega(t)\, \rho(x,t)\, \frac{\mathrm{d}^2}{\mathrm{d}t^2} \int x'\, \rho(x',t)\, \mathrm{d}x'\, \mathrm{d}t\ . \tag{6.4}$$

The weight $\omega(t)$ does not alter the regularization terms in Eq.(5.2). However, if $\hat{b}(x)$ is rewritten using partial integration over time, then the weight function must be considered appropriately[1)].

The above equations were applied to two generic cases. First, an experimental situation was considered with data gathered as snapshots in time, i.e., $\omega(t) := \frac{1}{N} \sum_{j=1}^{N} \delta(t_j - t)$, and Equations (6.3) and (6.4) were evaluated with this weight. All time integrations in both equations turned into sums over the $\rho(x,t)$-data gathered.

Next, was case in which the measurement process has been divided into two continuous time intervals of length T_1 and T_2 separated by a period of time τ. An appropriate choice of weights would either be

$$\omega(t) := \frac{\Theta(t) - \Theta(t - T_1)}{T_1 + T_2} + \frac{\Theta(t - \tau - T_1) - \Theta(t - \tau - T_1 - T_2)}{T_1 + T_2} \tag{6.5}$$

or

$$\omega(t) := \frac{\Theta(t) - \Theta(t - T_1)}{T_1} + \frac{\Theta(t - \tau - T_1) - \Theta(t - \tau - T_1 - T_2)}{T_2}\ . \tag{6.6}$$

The selection depends on the desired emphasis to be given to the two data intervals. Here, it was chosen to give the longer interval a larger contribution in $\hat{A}(x,x')$ than the short one. This can be better achieved with using Eq.(6.5); this choice is reasonable, provided the measured data $\rho(x,t)$ in both intervals are of comparable quality. Clearly many other issues can be incorporated into the design of $\omega(t)$ dictated by what is known about the nature of the data and the information sought about the PES.

The kernel is now

$$\hat{A}(x',x) = \frac{1}{T_1 + T_2} \left(\int_0^{T_1} + \int_{T_1+\tau}^{T_1+\tau+T_2} \right) \rho(x',t) \rho(x,t)\, \mathrm{d}t \tag{6.7}$$

and the RHS reads

$$\hat{b}(x) = -\frac{m}{T_1 + T_2} \left(\int_0^{T_1} + \int_{T_1+\tau}^{T_1+\tau+T_2} \right) \rho(x,t)\, \frac{\mathrm{d}^2}{\mathrm{d}t^2} \int x'\, \rho(x',t)\, \mathrm{d}x'\, \mathrm{d}t\ . \tag{6.8}$$

[1)] Consult Appendix D.1 on the issue of employing partial integration in time.

The interpretation of the weight in Eq.(6.5) up to this point was with reference to performing the inversion with an interrupted gathering of data from a *single* experiment. To explore this point further it is useful to rewrite the inverse problem in Eq. (6.2) with the help of Eqs.(6.7) and (6.8) as

$$\int \left[\, A_1(x,x') + A_2(x,x') \,\right] u(x')\,\mathrm{d}x' = \left[b_1(x) + b_2(x)\right] . \tag{6.9}$$

The indices "1" and "2" denote the evident two data time domains. In this form the gathering of data from *one interrupted* experiment can also be interpreted as finding the simultaneous solution to the inverse problem of *two different* experiments. These two experiments prepared with possibly distinct controls could, for example, explore different regions of the PES.

It was found that it is optimal to simply combine these distinct sets of data by addition as indicated the square braces in Eq.(6.9). This procedure will yield an inverse solution $u_0(x)$ with accuracy greater than a linear combination $u(x) = \mu\, u_1(x) + \nu\, u_2(x)$ of separate solutions to the individual problems "1" and "2" as explained below.

Consider two experiments that yield two different inverse solutions satisfying their respective system equation

$$\int A_{1,2}(x,x') u_{1,2}(x')\,\mathrm{d}x' = b_{1,2}(x) . \tag{6.10}$$

Naturally there should be only a unique exact $u_{\mathrm{ex.}}(x)$ for the physical system. Hence both system solutions $u_{1,2}$ in Eq.(6.10) can be decomposed into the exact solution and contamination pieces from the kernel's nullspace

$$u_{1,2}(x) = u_{\mathrm{ex.}}(x) + a_{1,2}(x) + r_{1,2}(x) . \tag{6.11}$$

The functions $a_{1,2}$ and $r_{1,2}$ are associated with the nullspace of the two kernels with $a_{1,2}(x) \in \ker(A_1) \cap \ker(A_2)$ being the contamination from the common nullspace of A_1 and A_2 and $r_{1,2}(x)$ the residual contribution unique to the respective kernel "1" or "2". The goal is to use the data to find an optimal solution $u_0(x)$ with the smallest possible nullspace contribution, i.e., eliminate a and r as far as possible.

Exploiting the linearity of the inverse problem we may add the two pieces of Eq.(6.10) to get

$$\int A_1(x,x') u_1(x')\,\mathrm{d}x' + \int A_2(x,x') u_2(x')\,\mathrm{d}x' = b_1(x) + b_2(x) . \tag{6.12}$$

This doesn't fully satisfy Eq.(6.9) and it is in general not possible to construct the optimal solution $u_0(x)$ as a linear combination

$$u_0(x) = \mu\, u_1(x) + \nu\, u_2(x) \tag{6.13}$$

with constant coefficients μ, ν. To elucidate this point, $u_0(x)$ is inserted into Eq.(6.9) and with the help of Eqs.(6.10) and (6.11) this yields cross terms proportional to

$$\int A_1(x,x')u_2(x')\,\mathrm{d}x' = b_1(x) + \int A_1(x,x')r_2(x')\,\mathrm{d}x' =: b_1(x) + {}_1\varepsilon_2(x) \tag{6.14a}$$

$$\int A_2(x,x')u_1(x')\,\mathrm{d}x' = b_2(x) + \int A_2(x,x')r_1(x')\,\mathrm{d}x' =: b_2(x) + {}_2\varepsilon_1(x)\,. \tag{6.14b}$$

Prefactors μ, ν have been omitted for simplicity. Hence $u_0(x)$ in Eq.(6.13) is not an optimal solution of Eq.(6.9) since it leaves errors proportional to ${}_i\varepsilon_j(x)$ that cannot be eliminated. However, by employing Eq. (6.9) and adding the kernels and the RHSs we can improve the inversion's quality. No error terms like ${}_i\varepsilon_j(x)$ will appear since by construction the then resulting $u_0(x)$ can be decomposed as $u_0(x) = u(x) + a_0(x)$ only. A contribution from $r_0(x)$ as in Eq.(6.11) will not arise, as proved in Appendix C. Thus, the solution of the combined problem will gain in quality by virtue of the reduced nullspace of the new kernel $A_1 + A_2$.

These optimality results are rigorous but it must be added that in general any combination of a finite amount of data will not fully eliminate the nullspace. However in the cases under comparison the assumption that a high degree of robustness can be attained holds true.

As argued above, the weighting function in Eq.(6.5) was chosen to result in observation-duration proportional entries in $A_1(x,x')$ and $A_2(x,x')$. Hence it is quite natural to add $A = A_1 + A_2$. On the other hand, choosing the approach Eq.(6.6) normalizes each data set independently. This logic naturally leads to considering the optimal combination of data to form $A = \sigma A_1 + \delta A_2$ where σ and δ are positive constants. This specially weighted form, or a convex combination $A = (1-\beta)A_1 + \beta A_2$ with $\beta \in (0,1)$, might be useful especially in the presence of different degrees of noise in the two data sets. A numerical scheme in β could then help to improve the solution by minimizing the effects of contamination by nullspace.

The optimal combination of data by addition of kernels $A_i(x,x')$ and RHSs $b_i(x)$ presented above was applied to the double well system with results for the gradient $u(x)$ and PES $V(x)$ shown in Fig. 6.1. Information was successively added to the kernel $A(x,x')$ by combining the data sets to form LT, LTR, and LTRH with the notation based on the initial conditions shown in Fig. 4.1. In each case all configurations are weighted equally. The optimal α_1 values employed and defect measures are given in table 5.1.

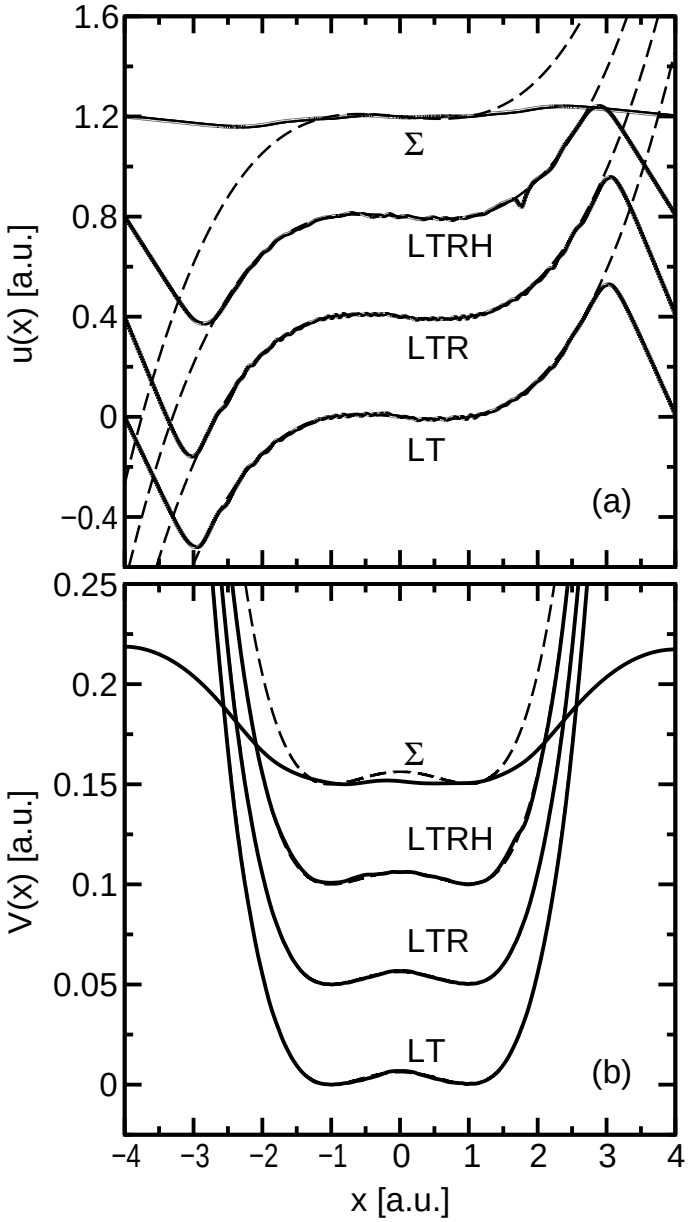

Figure 6.1: Extraction of PES for optimally combined (LT, LTR, and LTRH) as well as ρ-combined data (Σ). See the text and table 5.1 for further details. The curves for the potential's derivative $u(x)$ in (a) and the PES in (b) have been offset for graphical clarity and exact solutions (dashed lines) added for comparison. For several optimal combinations of the data the original and reconstructed PES are almost indistinguishable.

While the individual inverse problem solutions based on L, T, R, and H reproduce the potential in their respective neighborhoods quite well, they fail to give adequate results for the other portions of the potential. On the other hand, the reconstruction of large parts of the PES is successful if we optimally combine the data of the three experiments LTR. However, contrary to intuition, the solution is less satisfactory for combining all the data LTRH; some additional oscillations appear along with a dip in the vicinity of the initial wavepacket for H. Apparently the nullspace of the expanded domain cannot be fully managed by α_1 regularization alone; no attempt was made to simultaneously introduce α_0 and α_2 regularization or to weight the combination differently.

6.2 Other Combinations of Data

Several other schemes for combining the raw density data can be envisioned, apart from the approach in Chapter 6.1. One candidate would be the direct combination of $\rho(x,t)$ data from different experiments. As an illustration the case will be treated of two different ρ's with

$$\rho(x,t) := \rho_1(x,t) + \varepsilon\rho_2(x,t) \tag{6.15}$$

and ε being a positive constant. This combination is inspired by the linearity of Ehrenfest's theorem in the probability density (see Eq.(4.2)).

Insertion of this sum into the functional $J_0\{u(x)\}$ and variation with respect to $u(x)$ will yield a formulation analogous to the one describing inversion under the influence of noise in data in Eq.(6.19) upon comparison of Eqs.(6.17) and (6.15) (see the following section).

The terms proportional to ε^0 and ε^2 will exactly correspond to what was found earlier in Eq.(6.9). However, the terms proportional to ε represent a cross correlation between ρ_1 and ρ_2. These cross terms can be significant, and they act to introduce an element of undesirable structure, often oscillatory, in the equations determining $u(x)$. On physical grounds it is also artificial to directly correlate the independent experimental data ρ_1 and ρ_2 when seeking $u(x)$. Hence, the scheme of adding together the bare ρ-data is expected to produce unreliable results.

To support this argument a test on such a ρ-combination consisting of the sum of all four densities of the initial configurations L, T, R, and H was performed

$$\rho_\Sigma(x,t) := \rho_L(x,t) + \rho_T(x,t) + \rho_R(x,t) + \rho_H(x,t)\ . \tag{6.16}$$

The corresponding inverted gradient and respective PES are shown in Figs. 6.1a and 6.1b. The solution is rather poor and far worse than the LTRH combination using the same input data. This result should not be taken to

construe that other combinations of data might not give satisfactory results. However, the combination of A_i and b_i in Chapter 6.1 are quite natural and produce excellent inversion results.

6.3 The Influence of Noise on the Inversion

Any real ρ-data will always be contaminated by some degree of noise. In an additive model this noise contaminated data $\rho_{\mathrm{n}}(x,t)$ can be represented as

$$\rho_{\mathrm{n}}(x,t) = \rho(x,t) + \varepsilon\gamma(x,t) \;, \tag{6.17}$$

where $\varepsilon > 0$ is a small ordering parameter and the Markovian noise is described by the spatio-temporal function $\gamma(x,t)$. It is assumed that $\gamma(x,t)$ is a randomly varying function with vanishing average contribution and free from systematic error such that

$$\frac{1}{T}\int_0^T \gamma(x,t)\sigma(x,t)\,\mathrm{d}t \quad \stackrel{T\to\infty}{\longrightarrow} \quad 0 \tag{6.18}$$

for any function $\sigma(x,t)$ of bounded norm over time that is not correlated with $\gamma(x,t)$.

Inserting the ansatz in Eq.(6.17) into the functional $J_0\{u(x)\}$ in Eq.(4.3) and taking the first variation the equation determining $u(x)$ is obtained

$$\begin{aligned}
&\frac{1}{T}\int\!\!\int_0^T \rho(x',t)\rho(x,t)\,\mathrm{d}t\,u(x')\;\mathrm{d}x' + \frac{\varepsilon}{T}\int\!\!\int_0^T \rho(x',t)\gamma(x,t)\,\mathrm{d}t\;u(x')\,\mathrm{d}x' \\
&+ \frac{\varepsilon}{T}\int\!\!\int_0^T \gamma(x',t)\rho(x,t)\,\mathrm{d}t\,u(x')\;\mathrm{d}x' + \frac{\varepsilon^2}{T}\int\!\!\int_0^T \gamma(x',t)\gamma(x,t)\,\mathrm{d}t\;u(x')\,\mathrm{d}x' \\
&= -\frac{m}{T}\int_0^T \rho(x,t)\;\left[\frac{\mathrm{d}^2}{\mathrm{d}t^2}\int x'\rho(x',t)\,\mathrm{d}x' - \varepsilon\frac{\mathrm{d}^2}{\mathrm{d}t^2}\int x'\gamma(x',t)\,\mathrm{d}x'\right]\;\mathrm{d}t \\
&\quad - \frac{m}{T}\int_0^T \gamma(x,t)\;\left[\varepsilon\frac{\mathrm{d}^2}{\mathrm{d}t^2}\int x'\rho(x',t)\,\mathrm{d}x' - \varepsilon^2\frac{\mathrm{d}^2}{\mathrm{d}t^2}\int x'\gamma(x',t)\,\mathrm{d}x'\right]\;\mathrm{d}t \;.
\end{aligned} \tag{6.19}$$

The terms proportional to ε^0 recover the original unperturbed system in Eqs.(4.4–4.6). Assuming the data noise level to be small, the terms in ε^2 on both sides of Eq.(6.19) can be neglected.

We first turn to the kernel side of Eq.(6.19) and denote all terms in ε^1 as the error kernel $\delta A(x,x')$. Each term involves the computation of two-point

spatial correlations between functions. However, the functions γ and ρ are uncorrelated, and the temporal integral of their product is expected to result in only small random contributions to the kernel over x and x'. Longer time integration should further diminish the significance of $\delta A(x, x')$ which is a consequence of Eq.(6.18)

$$\delta A(x,x') := \frac{\varepsilon}{T}\int_0^T \gamma(x',t)\rho(x,t)\,\mathrm{d}t + \frac{\varepsilon}{T}\int_0^T \gamma(x,t)\rho(x',t)\,\mathrm{d}t \quad \stackrel{T\to\infty}{\longrightarrow} \quad 0 \tag{6.20}$$

Following similar logic, the complete second time integral on the rhs of Eq.(6.19) should be negligible, especially for long time integration. Also, the first term in ε^1 that involves the position average with respect to $\gamma(x,t)$ should vanish. In the end, for long time integration, only the first term of the rhs is left.

Hence, the functional J_0 exhibits some inherent capability to deal with slightly noisy systems. The time integration process averages out these noise effects so that they should have a decreasing impact on the inversion solution $u(x)$. Longer periods of temporal data should make their behavior better.

These results are also in accordance with the stability analysis presented in [81]. Resorting to the matrix version of the inverse problem (cf. Eq.(5.3)) the authors proved (Eq.(25) in Ref. [81]) that the relative error in the solution $\boldsymbol{u}$ after regularization is bounded by the relative errors in the data $\boldsymbol{\delta b}$ and $\boldsymbol{\delta A}$

$$\frac{\|\boldsymbol{\delta u}\|}{\|\boldsymbol{u}\|} \leqslant \frac{\mathrm{cond}(\boldsymbol{A}+\boldsymbol{\alpha})}{1-\|(\boldsymbol{A}+\boldsymbol{\alpha})^{-1}\,\boldsymbol{\delta A}\|}\left(\frac{\|\boldsymbol{\delta b}\|}{\|\boldsymbol{b}\|}+\frac{\|\boldsymbol{\delta A}\|}{\|\boldsymbol{A}\|}\right)\,. \tag{6.21}$$

In the above equation $\boldsymbol{\alpha}$ denotes the regularization terms, $\|\boldsymbol{v}\|^2 := \sum_{i=1}^N v_i^2$ is the square of the Euclidean vector norm, $\|\boldsymbol{A}\|^2 := \sum_{i,j}^N A_{ij}^2$ implies the square of the Frobenius matrix norm, and $\mathrm{cond}(\boldsymbol{A}) := \|\boldsymbol{A}\|\,\|\boldsymbol{A}^{-1}\|$ defines the condition number of a matrix.

Moreover, it was found (Eqs.(41) and (49) in [81]) that small perturbations $\varepsilon\boldsymbol{\gamma}$ will result in small proportional perturbations in $\boldsymbol{b}$ and $\boldsymbol{A}$. For example, the kernel matrix error is bound by

$$\frac{\|\delta\boldsymbol{A}\|}{\|\boldsymbol{A}\|} \leqslant 2\varepsilon\frac{\|\boldsymbol{\gamma}\|}{\|\boldsymbol{\rho}\|}\frac{\|\boldsymbol{\rho}\|^2}{T\|\boldsymbol{A}\|}\,. \tag{6.22}$$

Similar arguments apply to the RHS $\boldsymbol{b}$.

Hence for any application with finite time integration the excellent news is that the error will remain finite and bounded by the amount of noise inherent to the data. These results can now be extended to the long time integration limit. Equation (6.20) shows the relative influence of the noise on

the inversion process to become less significant for $T \to \infty$. Hence repeated measurements under the same initial conditions can improve the inversion process by enhancing the signal to noise ratio.

Equation (6.20) also demonstrates why the direct combination of bare $\rho(x,t)$ data discussed in Chapter 6.2 performs less satisfactory than the optimal combination scheme in Chapter 6.1. In contrast to the slightly perturbed system the cross term $\delta A(x,x')$ will not vanish for the ρ-combination. This will introduce an undesirable contribution to the inverse problem. On the other hand, the optimal combination scheme for different sets of data should profit from the inherent stability of the inversion procedure to deal with slightly noisy systems since this technique involves a sequence of separate time integrations.

Chapter 7

Summary and Outlook for Part II

Part II of the thesis presented new results improving and extending a recently suggested algorithm [81] to extract potential energy surfaces from the emerging experimental probability density $|\psi(x,t)|^2$ data. Since the required data with high spatio-temporal resolution is not yet available the extraction method has been successfully applied to simulated data for two 1-D model systems: The double well model of intramolecular proton transfer in substituted malonaldehyde systems proposed by Došlić *et al.* [11] and a dissociating O-H molecule represented by the Morse potential taken from the seminal work by Zhu and Rabitz [81].

An easy to implement improved regularization scheme was introduced which increases the accuracy of the computed PES without loss of numerical stability or speed. To quantify inversion accuracy and performance and to find optimal regularization parameters two error measures were provided. One of them is fully accessible through observed data, hence suitable for laboratory application. Ideas which should further help to speed up locating optimal regularization parameters are discussed as well.

Furthermore, an optimal combination method was presented. It combines data from different measurements and is argued to be optimal in the sense of reducing the ill-posedness of the inverse problem. In addition, a combination of distinct sets of data exploring different portions of the PES offers the possibility to increase the domain of the extracted PES. Evidence was presented that this scheme is stable under the influence of noise, but further investigations will be necessary to confirm these results. Another scheme combining measurements on the level of bare $|\psi(x,t)|^2$ was introduced as well but it was shown to yield less satisfactory results.

Some things already done, there still remains a plethora of interesting open questions:

- Up to now, the singular value decomposition has been employed for solving the linear equation of the inverse problem. This is very stable but will lead to a computational bottleneck in application to multi-dimensional system. Matrix dimensions will increase dramatically for larger molecules.
- In addition to $|\Delta s|$ an alternative experimentally accessible error measure to locate good regularization parameters might be helpful for laboratory application. An accurate scheme including an algorithm providing automated search capabilities would be desirable.
- To speed up inversion a reliable method that accepts only information from the PES domain predominantly covered by the wavepacket motion is useful. This procedure results in cutting the kernel $A(x, x')$ and the RHS $b(x)$ appropriately into dominant parts and an irrelevant remainder. From a numerical point of view this question is equivalent to the problem of quantum mechanical simulations how to choose the size of the simulation grid.
- Closely related to the cutting process would be a combination scheme that creates a patchwork PES. Different experiments might explore different portions of the surface and extract only these parts. The resulting surface fractions would then be combined to form a full PES. This should circumvent the drawback of the optimal combination scheme to always employ the full matrices for every experiment, which might lead to a numerical bottleneck for large molecules.
- Similar to cutting the matrix is the idea of a smooth regularization guided by the magnitude of the $\rho(x, t)$ data. While dominant parts of the kernel require less regularization, areas that are not covered by the wavepacket motion will call for more.
- It should be tested how the optimal combination scheme might enhance the performance of inverting dipole moments with the algorithm presented in [80].
- An algorithm that operates on time dependent as well as time independent probability density data might be helpful. The inclusion of already available spectroscopic data could also help increasing the quality of the inversion process [82, 83].
- An issue this work has not dealt with is decoherence. How might this enter the algorithm? How can it be compensated for in laboratory application? Compensation would provide an interesting means to learn from experimental data about the mechanisms leading to decoherence.

- If the extraction method wants to be considered for realistic laboratory application it must be able to cope with multidimensional systems. The inversion of 2-D data should be first. A good candidate would be the two dimensional potential energy surface of the ESIPT process of HBT discussed in Part I. The multidimensional application is closely related to the issue of finding fast computational means solving the inversion's matrix problem. Parallelized numerical code could help.

- A big open questions connected to multidimensional problems is, why is chemistry "local"? How can the inversion algorithm be understood to possibly brake down many dimensions into few and to construct effective coordinates from them?

Conclusion

This thesis dealt with two complementary approaches that connect experimental data to the theoretical modeling of ultrafast reactions employing potential energy surfaces.

Part I was devoted to a *direct* approach that relates experimental findings to characteristic *local* traits of quantum chemically obtained reaction surfaces. To this end normal mode analysis (NMA) was developed as a computational tool. It connects the dominant frequencies extracted from the coherent beat of a wavepacket which is monitored in transient absorption to the normal modes of an equilibrium structure on an *ab initio* surface.

This scheme has been applied to two photoinduced ultrafast reactions. First, the ringopening reaction of CHD was investigated. After photoexcitation the molecule returns to the groundstate surface via several conical intersections and relaxes back to either CHD or cZc-HT. To better understand the molecules ultrafast dynamics on the S_1 surface and the resulting groundstate surface dynamics NMA followed two distinct minimum energy paths toward two prominent S_1-S_0 conical intersections: C_2-CoIn and $CoIn_{Min}$. The computations revealed several significant modes that are characteristic to the path followed and to the CoIn passed for reaching the groundstate surface. These modes are assumed to be activated after the molecule returns to the groundstate surface. Based on some of these indicator modes feedback signals were proposed for an optimal control experiment selectively steering the molecule through a specific conical intersection and influencing the product yield.

Next, was the application of NMA to the excited state intramolecular proton transfer in HBT. Photoexcitation of the enol species leads to an ultrafast proton transfer in the excited state. The radiationless decay back to the groundstate keto tautomer is followed by a final proton back-transfer completing the cycle. Following a minimum energy path projected on a recently developed 2-D excited state reaction surface, NMA correctly determined three to four low-frequency skeleton modes driving the reaction. The computations unambiguously ruled out a simple high-energy single-mode driven transfer model in which the hydrogen is the active player. This is in excellent agreement with experimental findings and supports a recently published novel model for the hydrogen transfer process in HBT. The agreement

also justifies future applications of NMA to ultrafast reactions in which a long-living confined wavepacket follows a distinct reaction path and is monitored for longer times.

Part II was concerned with the *inverse* connection of experimentally accessible quantities to reaction surfaces. A novel algorithm was put forth recently that employs the time dependent probability density data $|\psi(x,t)|^2$ to construct an inverse problem that yields the entire reaction surface involved in the process. The practical utility and accuracy of this algorithm were enhanced via extended Tikhonov regularization and a new optimal scheme was introduced that combines multiple data sets to yield a larger reliable inversion range. These distinct sets represent the exploration of different portions of the potential surface with different experiments. The optimal combination scheme was shown to be based on the reduction of the ill-posedness of the problem and first results suggest the stability of this combination method under the influence of data noise.

The inversion algorithm, being a rather recent development, still leaves many questions open for future investigations. Some of them are related to algorithmic issues and to ease of use, others lead to issues on how the inversion process might be exploited further to learn about basic physical and chemical questions. I hope this work stimulates further research on this topic and especially hope for the experimental generation of appropriate probability density data that would turn simulations into reality.

Appendix A

Selected Normal Modes of Cyclohexadiene and Hexatriene

To improve the microscopical understanding this section is included to illustrate CHD's and cZc-HT's motion in several selected groundstate normal modes. The ones discussed have a large contribution to the spectra and/or serve as fingerprint modes to determine a specific reaction mechanism (consult tables 1.1a and 1.1b on p. 21).

For illustration purposes the vibration's amplitude is chosen rather large. Each mode's picture shows the molecule at both turning points, printed in black and grey respectively. To simplify the plots, bold lines are used for double bonds. The carbon atom's labels in the text refer to those introduced in Fig. 1.2 on page 10. Since the molecule's dynamics is predominantly governed by the motion of its carbon skeleton hydrogen atoms are omitted in most figures. However for some modes both methylene groups are included if this helps to clarify the vibrational motion and its symmetry with respect to the Woodward-Hoffmann coordinate.

For CHD the dominant modes 196 cm^{-1}, 1153 cm^{-1}, and the fingerprint vibrations 539 cm^{-1}, 1401 cm^{-1} are discussed.

Modes 196 cm^{-1} and 1153 cm^{-1} most likely are Frank-Condon active and contribute strongly to the motion of CHD along both paths already from the beginning.

In Fig. A.1, for mode 196 cm^{-1} a perspective is chosen looking at the 1-6 σ-bond from a position only slightly above the molecule's plane (front view). Top view was selected for eigenmode 1153 cm^{-1}.

Mode 196 cm^{-1} increases the non-planarity of the molecule affecting especially the dihedral angle φ. The resulting motion is an out-of-plane twist

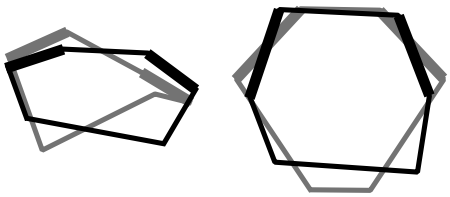

Figure A.1: CHD modes 196 cm^{-1} (left) and 1153 cm^{-1} (right).

with the σ-bonds 1-6 and 3-4 exhibiting an out-of-phase seesaw movement. Bond lengths stay nearly constant, only the angles are varied. On the other hand, eigenvibration 1153 cm^{-1} drives the 1-6 σ-bond break by large, synchronous bond length changes predominantly in the σ-bonds 1-6, 3-4 and 1-2, 5-6. Both double bonds do not demonstrate these large variations.

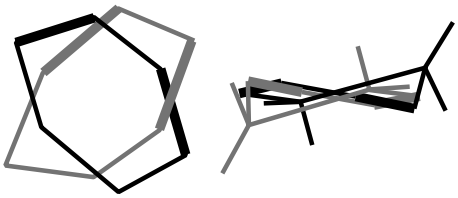

Figure A.2: CHD mode 539 cm^{-1}. Left: top view; right: front view.

Fingerprint modes 539 cm^{-1}, 1401 cm^{-1} are shown in Figs. A.2 and A.3 in top and front view. Both methylene groups are included in the latter. Eigenmode 539 cm^{-1} is the asymmetric stretching vibration along diagonals 2-4 and 3-6. Conversely, vibration 1401 cm^{-1} reflects the out-of-plane ringopening along the dihedral angle φ. Here, not a diagonal motion but minute variations of all bond-lengths are seen.

Both modes include a rotation of the CH_2-groups. The front view reveals the microscopical explanation of the two modes' ability to serve as a fingerprint to distinguish between the two CoIns. While vibration 539 cm^{-1} shows a disrotatory motion of the methylene groups, eigenmode 1401 cm^{-1} supports their conrotatory movement. As a consequence, any photochemical reaction path conserving C_2-symmetry must support this conrotatory mo-

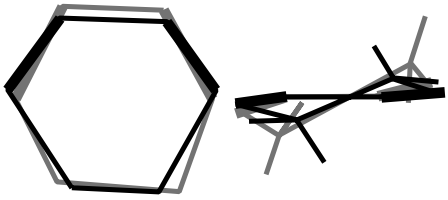

Figure A.3: Mode 1401 cm^{-1}. Right: front; left: top view.

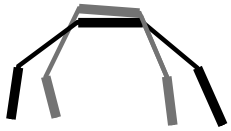

Figure A.4: cZc-HT mode 184 cm^{-1} from above.

tion. Correspondingly, NMA reveals large contributions of mode 1401 cm^{-1} and the suppression of mode 539 cm^{-1} at C_2-CoIn. On the other hand, the path heading toward $CoIn_{Min}$ does not conserve C_2-symmetry and there is no need to suppress mode 539 cm^{-1} (compare to Fig. 1.8 and table 1.1a).

For cZc-HT modes 97 cm^{-1}, 106 cm^{-1}, 184 cm^{-1}, and 326 cm^{-1}, 338 cm^{-1} were selected for discussion (cf. table 1.1b on page 21).

Mode 184 cm^{-1} is the major mode involved in all MEP positions investigated with NMA (see Fig. 1.9). Like CHD's modes 196 cm^{-1} and 1153 cm^{-1} it most likely is Frank-Condon active and predominantly affects the symmetric angle ϑ. It is a vibration resulting from the pseudoplanar 1-6 σ-bond cleavage.

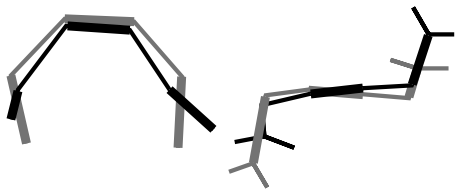

Figure A.5: cZc-HT mode 97 cm^{-1} from above (left) and in frontal perspective (right).

Indicator modes 97 cm^{-1} and 106 cm^{-1} are shown in Figs. A.5 and A.6 in top and front view. The first mode is a motion along φ and originates from the out-of-plane ringopening, the second predominantly involves the torsional angle ϑ with asymmetrically stretching diagonals 1-4 and 3-6. Similar to CHD's modes 539 cm^{-1}, 1401 cm^{-1} the frontal perspective of both cZc-HT vibrations reveals a minute effective conrotatory methylene movement in eigenmode 97 cm^{-1} and the small disrotatory CH_2-motion in

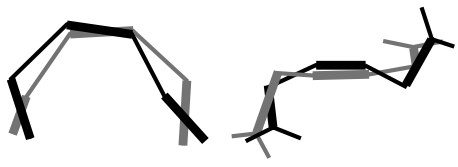

Figure A.6: cZc-HT mode 106 cm^{-1}. Top left, frontal right.

Figure A.7: cZc-HT vibration 326 cm^{-1} from above (left) and frontal (right).

eigenmode 106 cm^{-1}. Accordingly, latter eigenmode is suppressed at the C_2-CoIn (comp. Fig. 1.9 and table 1.1b).

Although in reverse order, a similar behavior is observed for fingerprint modes 326 cm^{-1} (Fig. A.7) and 338 cm^{-1} (Fig. A.8). At 326 cm^{-1} cZc-HT exhibits a stretching of the diagonals 1-4 and 3-6, plus a small disrotatory motion of both CH_2-groups. This time it shows in eigenvibration 338 cm^{-1} a behavior similar to mode 97 cm^{-1}. A large effect on φ and a conrotatory methylene motion is seen. Hence eigenmode 326 cm^{-1} appears at the non-symmetric $CoIn_{Min}$ while at the C_2-CoIn mode 338 cm^{-1} prevails.

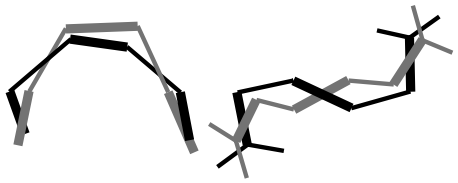

Figure A.8: cZc-HT mode 338 cm^{-1}. Top view left, frontal view right.

Appendix B

Preparatory Rotations

Quantum chemical computations of molecules with numerical packets like GAUSSIAN [23, 24] lead to configurations that often have to be manipulated prior to NMA: Atomic positions can be arbitrarily ordered, the coordinate system's origin can be shifted, the coordinate system itself can be mirrored or rotated. All these difficulties have to be taken care of to ensure all remaining differences between two molecular structures A, B to be purely due to internal degrees of freedom. This appendix presents an improved algorithm dealing with the rotational aspects. It outperforms the previously introduced approach [42] in terms of accuracy and computational speed and has been successfully applied to the ESIPT process in HBT and to CHD's ringopening reaction.

Badly ordered atoms and mirrored coordinates can easily be taken care of. For this purpose visualization tools like GOPENMOL [44] are very helpful. Equally simple is the proper shift of the position of the center of mass. This leaves the rotation of the improved molecular configuration B within closest distance of A as remaining problem (see Fig. B.1).

It is natural to assume such a unique optimal rotation to exist but this need not always be the case (e.g., in highly symmetric molecules). However,

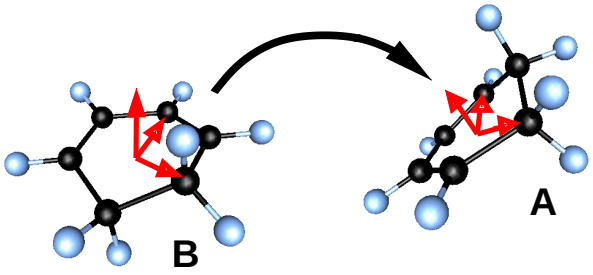

Figure B.1: CHD subject to translation and rotation apart from internal degrees of freedom.

this is not a problem for CHD, cZc-HT, or HBT. Enforcing a one-to-one correspondence between the atoms of the configurations A and B should take care of this. The optimal rotation is also expected to coincide with a minimum in vibrational energy (i.e., smallest Fourier coefficients in NMA) which can serve as an additional check.

The problem can be expressed as seeking a rotation $\boldsymbol{U}$ minimizing the distance

$$\rho := \sum_{i=1}^{N} \big[\, \boldsymbol{q}_i(A) - \boldsymbol{U} \cdot \boldsymbol{q}_i(B) \,\big]^2 \,. \tag{B.1}$$

In principle, Eq. (B.1) could be solved by a rotation in all three Euler angles (ψ, θ, ϕ), which unfortunately leads to a three parameter search. However, two Euler angles (say, ψ and θ) are used to fix the direction of the rotation axis and only ϕ then performs an actual in-plane rotation. The algorithm developed here reduces the problem to the ϕ-rotation only plus a fast search for the rotation axis based on physical insight.

For planar molecules like HBT the easiest way to find this axis is via the two tensors of inertia for configurations A, B

$$\boldsymbol{M}(A,B) := \sum_{i=1}^{N} m_i \big[\, \boldsymbol{q}_i(A,B)^2 \cdot \mathbb{1} - \boldsymbol{q}_i(A,B) \otimes \boldsymbol{q}_i(A,B) \,\big] \,. \tag{B.2}$$

The principal axes frame for either configuration is determined and each configuration is transfered into this frame

$$\boldsymbol{q}'_i(A) = \boldsymbol{Q}(A) \cdot \boldsymbol{q}_i(A) \quad \text{and} \quad \boldsymbol{q}'_i(B) = \boldsymbol{Q}(B) \cdot \boldsymbol{q}_i(B) \,. \tag{B.3}$$

Subsequently the directions of the largest moment of inertia of both configurations are identified to be the common $\hat{z}$-axis for *both* configurations A' and B'. The method proceeds with the one parameter search in the resulting x', y'-plane determining a rotation angle ϕ that yields an optimal frame B'' (see below for details on searching). Finally, B'' is transferred with the help of $\boldsymbol{Q}^{\mathrm{T}}(A)$ to a configuration that is in closest distance of A, completing the procedure for planar molecules.

For non-planar molecules like CHD and cZc-HT this $\hat{z}$-axis identification is not accurate enough and an iterative scheme to choose the rotation axis is required.

In classical mechanics the infinitesimal rotation of a vector $\boldsymbol{r}(t)$ can be expressed as

$$\boldsymbol{r}(t + \mathrm{d}t) = \boldsymbol{r}(t) + \boldsymbol{\Omega} \times \boldsymbol{q}_i(t)\, \mathrm{d}t \,, \tag{B.4}$$

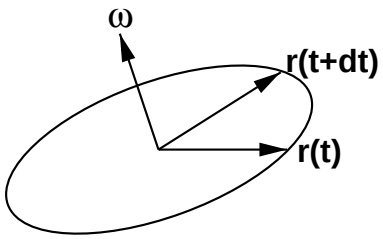

Figure B.2: Determining the axis of rotation.

where $\boldsymbol{\Omega}$ is the rotation vector parallel to the rotation axis $\hat{\boldsymbol{\omega}}$. From the sketch (Fig. B.2) this rotation axis can be determined in a straightforward fashion. Obviously, $\boldsymbol{r}(t)$ and the displacement vector $\boldsymbol{r}(t + \mathrm{d}t) - \boldsymbol{r}(t)$ both lie in the plane of rotation. Hence one constructs a new $\hat{z}$-axis parallel to $\hat{\boldsymbol{\omega}}$ with the help of

$$\hat{\boldsymbol{z}} = \frac{\boldsymbol{r}(t) \times \big[\, \boldsymbol{r}(t + \mathrm{d}t) - \boldsymbol{r}(t) \,\big]}{\| \cdots \|} \,. \tag{B.5}$$

By defining a quasi total angular momentum [5] this dynamical approach can be applied to all the nuclei in the static molecular configurations A, B as well

$$\boldsymbol{L} := \sum_{i=1}^{N} m_i \boldsymbol{q}_i(A) \times \big[\, \boldsymbol{q}_i(B) - \boldsymbol{q}_i(A) \,\big] \,. \tag{B.6}$$

The atomic masses help to average over the contributions of all atoms in the molecule. Similar to dynamics, where the angular momentum is the generator of rotations, a subsequent $\boldsymbol{\Omega} = \boldsymbol{M}^{-1} \cdot \boldsymbol{L}$ is necessary to find the actual rotation axis with the help of the inverse tensor of inertia.

The algorithm continues by defining the new $\hat{z}$-axis $\hat{\boldsymbol{z}} := \boldsymbol{\Omega}/\|\boldsymbol{\Omega}\|$ and by completing the new coordinate system "#" with the help of Gram-Schmidt orthogonalization applied to two arbitrary vectors. Both configurations A and B are then transferred into this new system. Hereafter, the two configurations' distance is minimized with the help of a rotation in the new xy-plane. That is, rewriting Eq. (B.1), minimize in the new system #

$$\rho(\phi) = \sum_{i=1}^{N} \Big[\, \boldsymbol{q}_i^{\#}(A) - \boldsymbol{U}(\phi) \cdot \boldsymbol{q}_i^{\#}(B) \,\Big]^2 \quad \text{with} \quad \frac{\delta \rho(\phi)}{\delta \phi} \stackrel{!}{=} 0 \,. \tag{B.7}$$

The rotation matrix is the same already employed for planar molecules

$$\boldsymbol{U}(\phi) = \begin{bmatrix} \cos(\phi) & \sin(\phi) & 0 \\ -\sin(\phi) & \cos(\phi) & 0 \\ 0 & 0 & 1 \end{bmatrix} \,. \tag{B.8}$$

This one-parameter search is taken care of with a Newton-Raphson gradient search method in which the improved solution angle $\phi_{\text{better}} = \phi_{\text{old}} + \delta\phi$ is determined via

$$\delta\phi = -\left[\frac{\partial^2\rho(\phi)}{\partial\phi^2}\right]^{-1} \cdot \frac{\partial\rho(\phi)}{\partial\phi}\bigg|_{\phi=\phi_{\text{old}}} . \tag{B.9}$$

A starting angle ϕ_{start} is found with the help of

$$\sum_{i=1}^{N} \frac{\boldsymbol{q}_i^{\#}(A)\cdot\boldsymbol{q}_i^{\#}(B)}{\|\cdots\|} = \sum_{i=1}^{N}\cos(\phi_i) \approx N\cos(\phi_{\text{start}}) . \tag{B.10}$$

On convergence, configuration $B^{\#}$ is transferred back to its original coordinate system in a final step. In general, the entire process has to be repeated a few times until A and B are closest to one another.

To test the method several molecular configurations A were selected. Suitable configurations B were generated from the As after a well-defined rotation around an arbitrary axis. The iterative algorithm for CHD as well as the principal axis scheme for HBT could both easily compensate for this artificial rotation. The iterative algorithm works on CHD but was also proven to readjust the planar molecule HBT in just a few steps.

This improved rotation method is rather fast and after 4–5 iterations convergence in the rotation angle is achieved. Iteration in the rotation axis requires another, say, ten steps. All in all, the entire process can be accomplished within a few minutes on a small desktop PC, compared to several hours beforehand [42].

Appendix C

Optimality Proof

This appendix presents the lemma and its proof underlying the optimal combination of data from different measurements presented in Chapter 6.1.

Lemma. *Given two Hermitian, positive semidefinite operators active on the Hilbert space $\mathcal{H}$, $\boldsymbol{A}_1, \boldsymbol{A}_2 : \mathcal{H} \to \mathcal{H}$, and their sum $\boldsymbol{A} := \mu\boldsymbol{A}_1 + \nu\boldsymbol{A}_2$ with coefficients $\mu, \nu \in \mathbb{R} > 0$. It then holds for the operators' nullspaces*

$$\ker(\boldsymbol{A}) = \ker(\boldsymbol{A}_1) \cap \ker(\boldsymbol{A}_2) \; .$$

For finite dimensional ranges this implies that

$$\operatorname{rank}(\boldsymbol{A}) = \operatorname{rank}(\boldsymbol{A}_1) + \operatorname{rank}(\boldsymbol{A}_2) - \dim\left(\operatorname{Range}(\boldsymbol{A}_1) \cap \operatorname{Range}(\boldsymbol{A}_2)\right) \; .$$

In other words: Adding two positive semidefinite, Hermitian operators will in general reduce the nullspace of the combined operator to being the intersection of both nullspaces. The generalization to a finite sum of operators $\boldsymbol{A} := \sum_{k=1}^{N} \alpha_k \boldsymbol{A}_k$ with constant $\alpha_k > 0$ is evident.

Proof: As both operators $\boldsymbol{A}_1$ and $\boldsymbol{A}_2$ are Hermitian, they have diagonal representations with respect to their eigenvectors $\boldsymbol{A}_1|\lambda_{1,i}\rangle = \lambda_{1,i}\,|\lambda_{1,i}\rangle$ and $\boldsymbol{A}_2|\lambda_{2,j}\rangle = \lambda_{2,j}\,|\lambda_{2,j}\rangle$. Without loss of generality the normalized eigenvectors $\{|\lambda_{1,i}\rangle\}$ are chosen as the basis of $\mathcal{H}$.

Clearly, $\mathcal{H}$ can be decomposed in the following two ways into orthogonal subspaces

$$\mathcal{H} = \ker(\boldsymbol{A}_1) \oplus \operatorname{Range}(\boldsymbol{A}_1) \tag{C.1}$$

and also

$$\mathcal{H} = \ker(\boldsymbol{A}_2) \oplus \operatorname{Range}(\boldsymbol{A}_2) \; . \tag{C.2}$$

In a similar fashion we can partition the spectrum of $\boldsymbol{A}_1$, and hence $\mathcal{H}$'s basis, into all eigenvectors that form a basis of $\operatorname{Range}(\boldsymbol{A}_1)$ and those that

generate $\ker(\boldsymbol{A}_1)$. Since $\mathcal{H}$ is a complete linear space and $\boldsymbol{A}_1, \boldsymbol{A}_2, \boldsymbol{A}$ are linear operators, it is sufficient to consider the basis states only. For any such state $|\lambda_{1,i}\rangle$ we find

$$\begin{aligned} \langle\lambda_{1,i}|\boldsymbol{A}|\lambda_{1,i}\rangle &= \mu\langle\lambda_{1,i}|\boldsymbol{A}_1|\lambda_{1,i}\rangle + \nu\langle\lambda_{1,i}|\boldsymbol{A}_2|\lambda_{1,i}\rangle \\ &= \mu\lambda_{1,i} + \nu\Lambda_i \ , \end{aligned} \tag{C.3}$$

where the mean Λ_i is defined

$$\Lambda_i := \langle\lambda_{1,i}|\boldsymbol{A}_2|\lambda_{1,i}\rangle = \sum_j |\langle\lambda_{2,j}|\lambda_{1,i}\rangle|^2 \ \lambda_{2,j} \geq 0 \ . \tag{C.4}$$

This quantity is always positive (or zero) by virtue of $\boldsymbol{A}_2$ being positive semidefinite.

In accordance with the decomposition in Eqs.(C.1) and (C.2) four different cases are to be distinguished:

$$|\lambda_{1,i}\rangle \in \mathrm{Range}(\boldsymbol{A}_1) : \quad \begin{cases} |\lambda_{1,i}\rangle \notin \ker(\boldsymbol{A}_2) & \Rightarrow \langle\lambda_{1,i}|\boldsymbol{A}|\lambda_{1,i}\rangle = \mu\lambda_{1,i} + \nu\Lambda_i > 0 \\ |\lambda_{1,i}\rangle \in \ker(\boldsymbol{A}_2) & \Rightarrow \langle\lambda_{1,i}|\boldsymbol{A}|\lambda_{1,i}\rangle = \mu\lambda_{1,i} + 0 > 0 \end{cases} \tag{C.5a}$$

$$|\lambda_{1,i}\rangle \in \ker(\boldsymbol{A}_1) : \quad \begin{cases} |\lambda_{1,i}\rangle \notin \ker(\boldsymbol{A}_2) & \Rightarrow \langle\lambda_{1,i}|\boldsymbol{A}|\lambda_{1,i}\rangle = 0 + \nu\Lambda_i > 0 \\ |\lambda_{1,i}\rangle \in \ker(\boldsymbol{A}_2) & \Rightarrow \langle\lambda_{1,i}|\boldsymbol{A}|\lambda_{1,i}\rangle = 0 + 0 \end{cases} \tag{C.5b}$$

Therefore only (basis) vectors that lie in *both* nullspaces will belong to the nullspace of $\boldsymbol{A}$, which proves the first part of the Lemma. The second part directly follows from the linear algebraic dimension relation

$$\begin{aligned} &\dim\left(\,\mathrm{Range}(\boldsymbol{A}_1) + \mathrm{Range}(\boldsymbol{A}_2)\,\right) \\ &\quad = \mathrm{rank}(\boldsymbol{A}_1) + \mathrm{rank}(\boldsymbol{A}_2) - \dim\left(\,\mathrm{Range}(\boldsymbol{A}_1) \cap \mathrm{Range}(\boldsymbol{A}_2)\,\right) \ , \end{aligned} \tag{C.6}$$

where "+" on the lefthand side denotes all linear combinations of the vectors in both ranges.

Now, any vector that lies either in $\mathrm{Range}(\boldsymbol{A}_1)$ or in $\mathrm{Range}(\boldsymbol{A}_2)$ will, with an argument similar to Eq.(C.5), always be in $\mathrm{Range}(\boldsymbol{A})$. We are thus allowed to replace

$$\dim\left(\,\mathrm{Range}(\boldsymbol{A}_1) + \mathrm{Range}(\boldsymbol{A}_2)\,\right) = \mathrm{rank}(\mu\boldsymbol{A}_1 + \nu\boldsymbol{A}_2) \tag{C.7}$$

which completes the proof.

Clearly, the lemma's first part could have been proved without using a basis. The decomposition Eq.(C.1) and the differentiation in Eq.(C.5) into

$|\phi\rangle \in \ker(\boldsymbol{A}_1)$ or $|\phi\rangle \notin \ker(\boldsymbol{A}_1)$ for any $|\phi\rangle \in \mathcal{H}$ suffice. However, the second part of the lemma requires counting the basis vectors.

It is further noted that neither positivity nor Hermiticity can be omitted. Without the former criterion, a counterexample is $\boldsymbol{A}_2 = -\boldsymbol{A}_1$, with $\mu = \nu = 1$. Without the latter criterion, the two $\mathbb{R}^{3\times 3}$ operators

$$\boldsymbol{A}_1 = \begin{bmatrix} 1 & 1 & 1 \\ 0 & 1 & 1 \\ 0 & 0 & 1 \end{bmatrix}, \; \boldsymbol{A}_2 = \begin{bmatrix} 0 & 0 & 0 \\ 1 & 0 & 0 \\ 1 & 1 & 0 \end{bmatrix} \quad \Rightarrow \; \boldsymbol{A}_1 + \boldsymbol{A}_2 = \begin{bmatrix} 1 & 1 & 1 \\ 1 & 1 & 1 \\ 1 & 1 & 1 \end{bmatrix} \tag{C.8}$$

with ranks 3, 2, and 1 lead to the contradiction $1 = 3 + 2 - 2$.

Appendix D

Other Means of Improving the Inversion

The following two sections provide some notes that are intended to help in application and numerical implementation of the inversion algorithm. The first deals with an approach to compute the RHS $b(x)$ by means of partial integration in time. Subsequently Section D.2 suggests to exploit scale invariant features when determining optimal regularization parameters. This should help saving computational time.

D.1 Avoiding Partial Integration for $b(x)$

In the original work of Zhu and Rabitz [81] it has been pointed out that the computation of the RHS $b(x)$ in Eq. (4.5) on p. 47 requires taking the second time derivative of the probability density. In view of the disadvantages entailed, an approach based on partial integration over time has been proposed calling for a first order time derivative only

$$\begin{aligned} b(x) &= -\frac{m}{T}\int_0^T \rho(x,t)\,\frac{\mathrm{d}^2}{\mathrm{d}t^2}\int x'\,\rho(x',t)\,\mathrm{d}x'\,\mathrm{d}t \\ &= -\frac{m}{T}\rho(x,t)\,\frac{\mathrm{d}\,\langle x(t)\rangle}{\mathrm{d}t}\,\Big|_0^T + \frac{m}{T}\int_0^T \frac{\mathrm{d}\,\rho(x,t)}{\mathrm{d}t}\,\frac{\mathrm{d}\,\langle x(t)\rangle}{\mathrm{d}t}\,\mathrm{d}t\,. \end{aligned} \tag{D.1}$$

This approach produces good results that are slightly less accurate than the usual method in Eq.(4.5) on p.47. An example that utilizes partial integration is situation $\mathrm{M_{PI}}$ shown in Fig. 5.5 on p. 61. The lower inversion accuracy is expressed in the slightly larger $|\Delta u|$-error given in table 5.2 on p. 62. Compare situation $\mathrm{M_{PI}}$ to the conventional second order approach M.

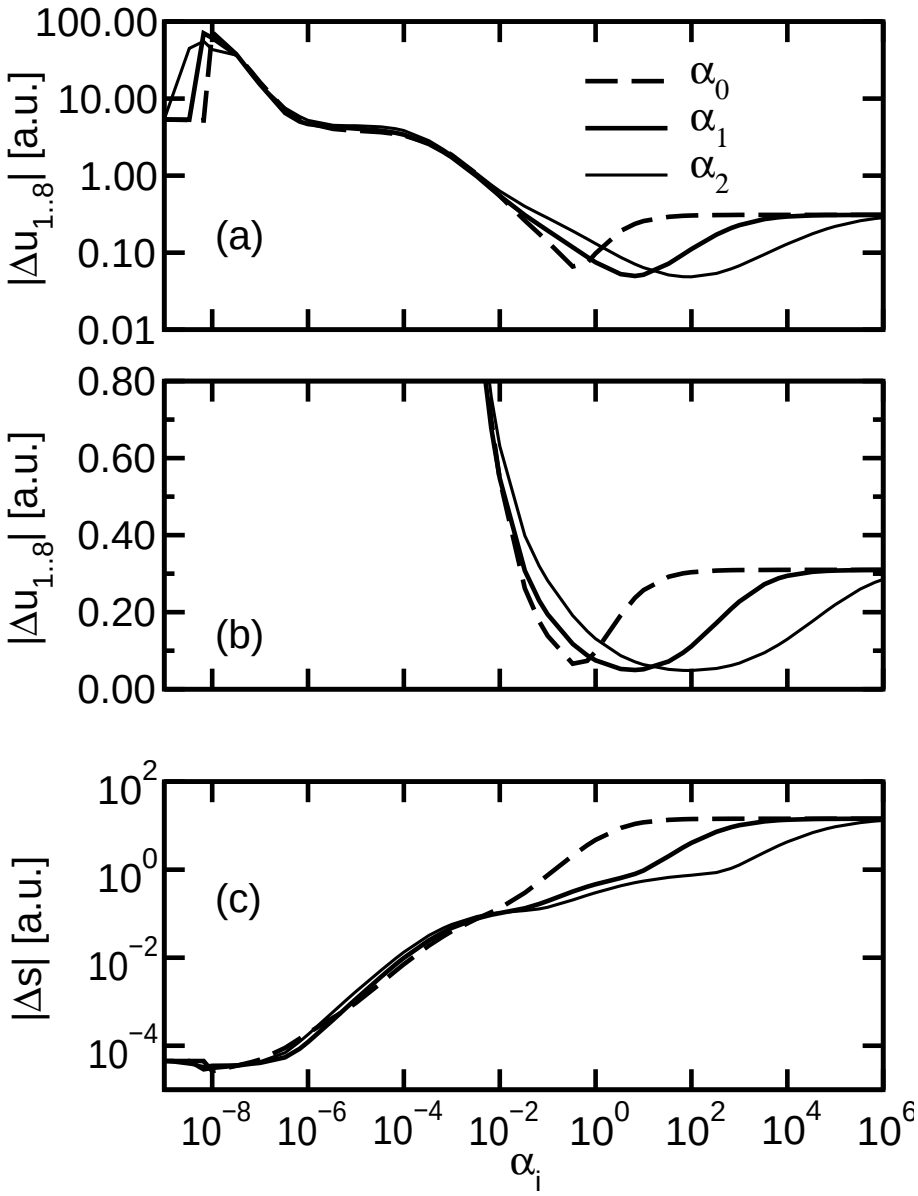

Figure D.1: The α_ν parameter scan computed for the Morse potential employing partial integration for $b(x)$. The solution defect $|\Delta u|$ is shown in both top panels with respect to the reliable inversion range $1.0 \leqslant x \leqslant 8.0$. (a) uses a logarithmic scale and (b) shows the vicinity of the minima only. The system defect $|\Delta s|$ is given in (c) (comp. Fig. 5.4 on p. 60). Similar results were found for the double well system.

However, a thorough test of the overall inversion performance produced unsatisfactory results since it has a very small range of stable regularization parameters. In laboratory application only $|\Delta s|$ is accessible for finding good regularization parameters. This can be difficult and Fig. D.1 proves it very likely to miss the area of stable α_ν-parameters. The figure also shows that insufficient regularization will lead to poor results and dramatic inversion errors compared to the conventional approach.

This behavior most likely is effected by the compromise accepted for the numerical implementation of Eq.(D.1). It will always be extremely difficult to reliably compute the boundary terms on only few $\rho(x,t)$ snapshots in time. Unless one is willing to discard data one inevitably needs to work with one-sided derivatives at $t = 0$ and T, which diminishes the accuracy.

D.2 Scale Invariance and Search for Regularization Parameters

Certain self similar features with respect to the regularization α-parameters have already been mentioned on p. 62. It has been stated that in laboratory application the similar shapes of all the $|\Delta s|(\alpha_\nu)$ curves could be exploited to locate good regularization parameters since the area in which all these curves show a "knee" coincides with a region of small solution defects $|\Delta u|(\alpha_\nu)$.

The reason for the similar behavior of the different regularization levels can be deduced from the matrix formulation in Eq.(5.3). Redefining the differentiation band matrices $\widehat{\boldsymbol{D}} := \Delta x^2 \boldsymbol{D}$ and $\widehat{\boldsymbol{Q}} := \Delta x^2 \boldsymbol{Q}$ (consult the Eqs.(5.4) and (5.5) on p. 54) the inversion's regularized matrix problem can be stated as

$$\left[\boldsymbol{A} + \frac{\alpha_0}{\Delta x^2}\mathbb{1} - \frac{\alpha_1}{\Delta x^2}\widehat{\boldsymbol{D}} + \frac{\alpha_2}{\Delta x^2}\widehat{\boldsymbol{Q}}\right] \cdot \boldsymbol{u}\,\Delta x = \boldsymbol{b}\,. \tag{D.2}$$

Since all the regularization matrices are diagonal dominant it is natural to expect *to leading order* a comparable regularization capability for the individual levels.

Another effect often observed was the appearance of scale invariant features in the defects $|\Delta s|$ and $|\Delta u|$ considered at different spatial inversion resolutions $\kappa := \Delta x/\Delta x_{\text{prop}}$. $|\Delta u|(\alpha_\nu)$ curves as well as $|\Delta s|(\alpha_\nu)$ scans overlap for different κ-values. Examples are given in Fig. D.2 for the κ-values 16,32, and 64. The standard value for all the other parameter scans presented in this work is $\kappa = 16$, i.e., only every 16th propagation gridpoint was considered for the inversion process (highlighted curves in Fig. D.2).

The reason can be found on inspection of Eq.(D.2). Consider two inversion resolutions, say, $\Delta x = \Delta x_{\text{prop}}$ and $\Delta x_{\text{new}} = \kappa \cdot \Delta x$ with a constant

$\kappa > 0$. Inserting Δx_{new} into the kernel part of Eq.(D.2) yields

$$\begin{aligned} &\boldsymbol{A} + \frac{\alpha_0}{\Delta x_{\text{new}}^2}\mathbb{1} - \frac{\alpha_1}{\Delta x_{\text{new}}^2}\widehat{\boldsymbol{D}} + \frac{\alpha_2}{\Delta x_{\text{new}}^2}\widehat{\boldsymbol{Q}} \\ &= \boldsymbol{A} + \underbrace{\frac{\alpha_0}{\kappa^2}}_{\alpha_{0\,\text{new}}}\frac{1}{\Delta x^2}\mathbb{1} - \underbrace{\frac{\alpha_1}{\kappa^2}}_{\alpha_{1\,\text{new}}}\frac{1}{\Delta x^2}\widehat{\boldsymbol{D}} + \underbrace{\frac{\alpha_2}{\kappa^2}}_{\alpha_{2\,\text{new}}}\frac{1}{\Delta x^2}\widehat{\boldsymbol{Q}}\,. \end{aligned} \tag{D.3}$$

Hence the problem in Δx_{new} can be expressed as the old problem in Δx but with rescaled regularization parameters $\alpha_{\nu\,\text{new}}$. $|\Delta u|(\alpha_\nu)$ and $|\Delta s|(\alpha_\nu)$ show only a weak dependence on the individual regularization parameters, hence

$$\log(\alpha_{\nu\,\text{new}}) = \log\left(\frac{\alpha_\nu}{\kappa^2}\right) = \log(\alpha_\nu) - 2\log(\kappa)\,. \tag{D.4}$$

Thus there only is a small offset and the error functions $|\Delta u|(\alpha_\nu)$ and $|\Delta s|(\alpha_\nu)$ should tend to overlap for different grid spacings. This argument holds best in the vicinity of the $|\Delta u|$ minima and the $|\Delta s|$ "knees" when all these functions are slowly varying. It corresponds to the behavior observed in Fig. D.2.

It can be concluded that in laboratory application computational time could be saved and suitable regularization parameter ranges could be determined on a low resolution grid. Only a final stage should require as many data points as available. However, further studies and especially laboratory applications are needed to support the above argumentation. It might well be that the scale invariance is only a numerical artefact: Choosing a dense grid for propagation leads to well converged wavefunctions $\psi(x,t)$, and consequently kernels $A(x,x')$ and RHSs $b(x)$. Thus there could be invariance with respect to coarse graining the grid spacing Δx as long as this propagational convergence is not destroyed.

Note that this argumentation is complementary to the scale invariance for $\Delta x \to 0+$. As already stated in [81] only a limited amount of information is extractable by the inversion algorithm. This limit is set by the number of eigenstates involved in the generation of the $\psi(x,t)$ exploring the reaction surface. The extracted PES will not improve by a simple increase in the number of inversion points.

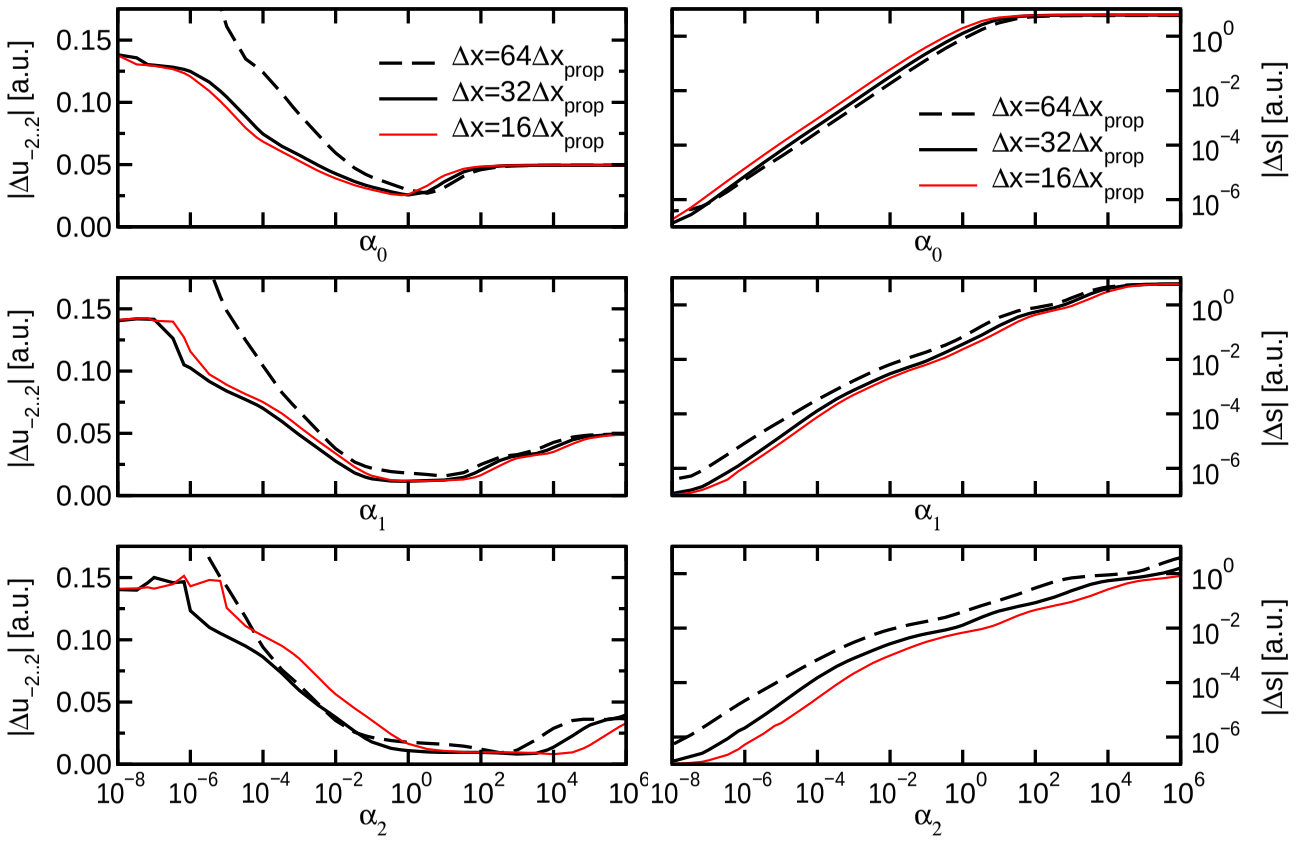

Figure D.2: The α_ν parameter scan computed for the double well situation H for different inversion grid spacings Δx. The lefthand side shows the solution defect $|\Delta u|$, each panel representing the dependence on a different regularization parameter α_ν. The reliable inversion domain is $-2.0 \leqslant x \leqslant 2.0$. The system defect $|\Delta s|$ is given on the righthand side in a similar fashion. Colored curves correspond to $\Delta x = 16 \cdot \Delta x_{\text{prop}}$ already shown Fig. 5.1 on p. 56.

Bibliography

[1] A. Assion, T. Baumert, M. Bergt, T. Brixner, B. Kiefer, V. Seyfried, M. Strehle and G. Gerber, *Control of chemical reactions by feedback-optimized phase-shaped femtosecond laser pulses*, Science **282**, 919 (1998).

[2] A. Assion, M. Geisler, J. Helbing, V. Seyfried and T. Baumert, *Femtosecond pump-probe photoelectron spectroscopy: Mapping of vibrational wave-packet motion*, Physical Review A **54**, R4605 (1996).

[3] F. Bernardi, M. Olivucci and M. A. Robb, *The role of conical intersections and excited state reaction paths in photochemical pericyclic reactions*, Journal of Photochemistry and Photobiology A: Chemistry **105**, 365 (1997).

[4] M. Born and J. R. Oppenheimer, Annalen der Physik **84**, 457 (1927).

[5] E. Bright Wilson, Jr., J. C. Decius and P. C. Cross, *Molecular Vibrations*, McGraw-Hill Book Company, New York (1955).

[6] P. Celani, F. Bernardi, M. A. Robb and M. Olivucci, *Do photochemical ring-openings occur in the spectroscopic state? B-1(2) pathways for the cyclohexadiene/hexatriene photochemical interconversion*, Journal of Physical Chemistry **100**, 19364 (1996).

[7] C. Chudoba, E. Riedle, M. Pfeiffer and T. Elsaesser, *Vibrational coherence in ultrafast excited state proton transfer*, Chemical Physics Letters **263**, 622 (1996).

[8] R. de Vivie-Riedle, K. Sundermann and M. Motzkus, *Laser control strategies for energy transfer reactions in atom molecule collisions*, Faraday Discussions **113**, 303 (1999).

[9] V. de Waele, private communication.

[10] V. de Waele, L. Kurtz, E. Riedle and R. de Vivie-Riedle, *Ab initio investigation of structure and vibrational motions driving the excited state proton transfer of HBT*, in preparation .

[11] N. Došlić, O. Kühn, J. Manz and K. Sundermann, *The "hydrogen-subway" – a tunneling approach to intramolecular hydrogen transfer reactions controlled by ultrashort laser pulses*, Journal of Physical Chemistry A **102**, 9645 (1998).

[12] C. Eckart, *The kinetic energy of polyatomic molecules*, Physical Review **46**, 383 (1934).

[13] C. Eckart, *Some studies concerning rotating axes and polyatomic molecules*, Physical Review **47**, 552 (1935).

[14] P. Ehrenfest, Zeitschrift für Physik **45**, 455 (1927).

[15] R. Fabiano, R. Knobel and B. Lowe, *A finite-difference algorithm for an inverse Strum-Liouville problem*, IMA Journal or Numerical Analysis **15**, 75 (1995).

[16] M. D. Feit and J. A. Fleck, *Light propagation in graded-index optical fibers*, Applied Optics **17**, 3990 (1978).

[17] M. D. Feit, J. A. Fleck and A. Steiger, *Solution of a Schrodinger equation by a spectral method*, Journal of Computational Physics **47**, 412 (1982).

[18] A. Ferretti, A. Lami and G. Villani, *Interference effects in molecular system with curve crossing*, Chemical Physics Letters **290**, 131 (1998).

[19] A. Ferretti, A. Lami and G. Villani, *Quantum dynamics at a conical intersection: The role of the variation of oscillator frequencies in the diabatic transition*, Journal of Chemical Physics **109**, 9002 (1998).

[20] A. Ferretti, A. Lami and G. Villani, *Transition probability due to a conical intersection: On the role of the initial conditions and of the geometric setup of the crossing surfaces*, Journal of Chemical Physics **111**, 916 (1999).

[21] V. A. Fock, Zeitschrift für Physik **61**, 126 (1930).

[22] V. A. Fock, Zeitschrift für Physik **62**, 795 (1930).

[23] M. J. Frisch, G. W. Trucks, H. B. Schlegel, P. M. W. Gill, B. G. Johnson, M. A. Robb, J. R. , Cheeseman, T. Keith, G. A. Petersson, J. A. Montgomery, K. Raghavachari, M. A. Al-Laham, V. G. Zakrzewski, J. V. Ortiz, J. B. Foresman, J. Cioslowski, B. B. Stefanov, A. Nanayakkara, M. Challacombe, C. Y. Peng, P. Y. Ayala, W. Chen, M. W. Wong, J. L. Andres, E. S. Replogle, R. Gomperts, R. L. Martin, D. J. Fox, J. S. Binkley, D. J. Defrees, J. Baker, J. P. Stewart, M. Head-Gordon, C. Gonzalez and J. A. Pople, GAUSSIAN94 *Rev. E.2* (1998).

[24] M. J. Frisch, G. W. Trucks, H. B. Schlegel, G. E. Scuseria, M. A. Robb, J. R. Cheeseman, V. G. Zakrzewski, J. A. Montgomery, Jr., R. E. Stratmann, J. C. Burant, S. Dapprich, J. M. Millam, A. D. Daniels, K. N. Kudin, M. C. Strain, O. Farkas, J. Tomasi, V. Barone, M. Cossi, R. Cammi, B. Mennucci, C. Pomelli, C. Adamo, S. Clifford, J. Ochterski, G. A. Petersson, P. Y. Ayala, Q. Cui, K. Morokuma, D. K. Malick, A. D. Rabuck, K. Raghavachari, J. B. Foresman, J. Cioslowski, J. V. Ortiz, A. G. Baboul, B. B. Stefanov, G. Liu, A. Liashenko, P. Piskorz, I. Komaromi, R. Gomperts, R. L. Martin, D. J. Fox, T. Keith, M. A. Al-Laham, C. Y. Peng, A. Nanayakkara, C. Gonzalez, M. Challacombe, P. M. W. Gill, B. Johnson, W. Chen, M. W. Wong, J. L. Andres, C. Gonzalez, M. Head-Gordon, E. S. Replogle and J. A. Pople, GAUSSIAN98 *Rev. A.7* (1999).

[25] W. Fuß, T. Schikarski, W. E. Schmid and K. L. Kompa, *Ultrafast dynamics of the photochemical ring opening of 1,3-cyclohexadiene studied by multiphoton ionization*, Chemical Physics Letters **262**, 675 (1996).

[26] M. Garavelli, F. Bernardi, P. Celani, R. M. A. and M. Olivucci, *Minimum energy paths in the excited and ground states of short protonated Schiff bases and of the analogous polyenes*, Journal of Photochemistry and Photobiology A: Chemistry **114**, 109 (1998).

[27] M. Garavelli, F. Bernardi, M. Olivucci, T. Vreven, S. Klein, P. Celani and M. A. Robb, *Potential-energy surfaces for ultrafast photochemistry*, Faraday Discussions **110**, 51 (1998).

[28] M. Garavelli and M. Olivucci, private communication.

[29] J. D. Geiser and P. M. Weber, *Pump-probe diffraction imaging of vibrational wave functions*, Journal of Chemical Physics **108**, 8004 (1998).

[30] R. B. Gerber, M. Shapiro, U. Buck and J. Schleusener, *Quantum-mechanical inversion of the differential cross section: Determination of the He-Ne potential*, Physical Review Letters **41**, 236 (1978).

[31] P. E. Gill and G. F. Miller, *An algorithm for the integration of unequally spaced data*, The Computer Journal **15**, 80 (1972).

[32] D. R. Hartree, Proceedings of the Cambridge Philosophical Society **24**, 89 (1928).

[33] T. Ho, H. Rabitz, S. Choi and M. Lester, *Application of an inverse method to the determination of a two-dimensional intermolecular potential energy surface for the Ar-OH($A^2\Sigma^+, \nu = 0$) complex from rovibrational spectra*, Journal of Chemical Physics **104**, 1187 (1996).

[34] T.-S. Ho and H. Rabitz, *Inversion of experimental data to extract intermolecular and intramolecular potentials*, Journal of Physical Chemistry **97**, 13447 (1993).

[35] A. Hofmann, *Ultraschnell molekulrae Quantendynamik durch konische Durchschneidungen*, PhD. Thesis, Fakultät für Physik, LMU, München (2001).

[36] A. Hofmann and R. de Vivie-Riedle, *Quantum dynamics of photoexcited cyclohexadiene introducing reactive coordinates*, Journal of Chemical Physics **112**, 5054 (2000).

[37] A. Hofmann, L. Kurtz and R. de Vivie-Riedle, *Interaction of electronic structure and nuclear dynamics on the S_1 reaction surface for the ringopening of cyclohexadiene*, Applied Physics B **71**, 391 (2000).

[38] A. Hofmann and R. d. Vivie-Riedle, *Adiabatic approach for ultrafast quantum dynamics mediated by simultaneously active conical intersections*, Chemical Physics Letters (2001).

[39] R. R. Jones, *Measurement of electronic radial probability distributions using time-resolved isolated core excitation*, Physical Review A **57**, 446 (1998).

[40] R. S. Judson and H. Rabitz, *Teaching lasers to control molecules*, Physical Review Letters **68**, 1500 (1992).

[41] J. L. Krause, K. J. Schafer, M. Ben-Nun and K. R. Wilson, *Creating and detecting shaped rydberg wave packets*, Physical Review Letters **79**, 4978 (1997).

[42] L. Kurtz, A. Hofmann and R. de Vivie-Riedle, *Groundstate normal mode analysis: Linking excited state dynamics and experimental observables*, Journal of Chemical Physics **114**, 6151 (2001).

[43] K. Kwon and A. Moscowitz, *Molecular ion geometries from inversion of coulomb explosion imaging data*, Physical Review Letters **77**, 1238 (1996).

[44] L. Laaksonen, gOpenMol *Ver. 1.3 (99xxyy) Linux*, Center for Scientific Computing, Espoo, Finland (1999).

[45] R. D. Levine and R. B. Bernstein, *Molecular Reaction Dynamics*, Oxford Univ. Press, New York, N.Y. (1974).

[46] R. J. Levis, G. M. Menkir and H. Rabitz, *Selective bond dissociation and rearrangement with optimally tailored, strong-field laser pulses*, Science **292**, 709 (2001).

[47] S. Lochbrunner, W. Fuß, W. E. Schmid and K. L. Kompa, *Electronic relaxation and ground-state dynamics of 1,3-cyclohexadiene and cis-hexatriene in ethanol*, Journal of Physical Chemistry A **102**, 9334 (1998).

[48] S. Lochbrunner, A. J. Wurzer and E. Riedle, *Ultrafast excited-state proton transfer and subsequent coherent skeletal motion of 2-(2'-hydroxyphenyl)benzothiazole*, Journal of Chemical Physics **112**, 10699 (2000).

[49] A. K. Louis, *Numerik Inverser Probleme*, GAMM-Mitteilungen **1**, 5 (1990).

[50] B. Lowe, M. Pilant and W. Rundell, *The recovery of potentials from finite spectral data*, SIAM Journal on Mathematical Analysis **23**, 482 (1992).

[51] P. M. Morse, *Diatomic Molecules According to the Wave Mechanics. II. Vibrational Levels*, Physical Review **34**, 57 (1929).

[52] G. K. Paramonov, *Coherent control of linear and nonlinear multiphoton excitation of molecular vibrations*, Chemical Physics **177**, 169 (1993).

[53] W. H. Press, S. A. Teukolsky, W. T. Vetterling and B. P. Flannery, *Numerical Recipes in C: The Art of Scientific Computing*, Cambridge University Press, 2nd ed. (1994).

[54] S. Pullen, N. A. Anderson, L. A. Walker II and R. J. Sension, *The ultrafast ground and excited state dynamics of cis-hexatriene in cyclohexane*, Journal of Chemical Physics **107**, 4985 (1997).

[55] S. Pullen, N. A. Anderson, L. A. Walker II and R. J. Sension, *The ultrafast photochemical ring-opening reaction of 1,3-cyclohexadiene in cyclohexane*, Journal of Chemical Physics **108**, 556 (1998).

[56] S. Pullen, L. A. Walker II, B. Donavan and R. J. Sension, *Femtosecond transient absorption study of the ring-opening reaction of 1,3-cyclohexadiene*, Chemical Physics Letters **242**, 415 (1995).

[57] H. Rabitz, R. de Vivie-Riedle and M. M. K. Kompa, *Whither the future of controlling quantum phenomena?*, Science **288**, 824 (2000).

[58] P. J. Reid, S. J. Doig and R. A. Mathies, *Picosecond time-resolved uv resonance raman-spectroscopy of the photochemical ring-opening of 1,3,5-cyclooctratrine and alpha-phellandrede*, Journal of Physical Chemistry **94**, 8396 (1990).

[59] P. J. Reid, S. J. Doig, S. D. Wickham and R. A. Mathies, *Photochemical ring-opening reactions are complete in picoseconds - a time-resolved uv resonance raman-study of 1,3-cyclohexadiene*, Journal of the American Chemical Society **115**, 4754 (1993).

[60] P. J. Reid, M. K. Lawless, S. D. Wickham and R. A. Mathies, *Determination of pericyclic photochemical-reaction dynamics with resonance raman-spectroscopy*, Journal of Physical Chemistry **98**, 5597 (1994).

[61] E. Riedle, S. Lochbrunner, A. J. Wurzer, V. de Waele and R. de Vivie-Riedle, *Does the proton move during ultrafast excited state intramolecular proton transfer?*, in: T. Elsaesser, S. Mukamel, M. Murnane and N. Scherer (Eds.), *Ultrafast Phenomena XII*, pp. 645–647, Springer Verlag (2000).

[62] E. Schrödinger, *Quantisierung als Eigenwertproblem (Erste Mitteilung)*, Annalen der Physik **79**, 361 (1926).

[63] M. Shapiro, *Spectroscopic wave function imaging and potential inversion*, Journal of Physical Chemistry **100**, 7859 (1996).

[64] J. Stoer and R. Bulirsch, *Numerische Mathematik 2*, Springer Verlag, Berlin, 3rd ed. (1990).

[65] A. Szabo and N. S. Ostlund, *Modern Quantum Chemistry: Introduction to Advanced Electronic Structure Theory*, Macmillan Publishing, New York (1982).

[66] D. J. Tannor, R. Kosloff and S. A. Rice, *Coherent pulse sequence induced control of selectivity of reactions: Exact quantum mechanical calculations*, Journal of Chemical Physics **85**, 5805 (1986).

[67] D. J. Tannor and S. A. Rice, *Control of selectivity of chemical reaction via control of wave packet evolution*, Journal of Chemical Physics **83**, 5013 (1985).

[68] A. N. Tikhonov and F. John, *Solutions of Ill-Posed Problems*, Scripta Series in Mathematics, Winston, Washington, D.C. (1977).

[69] M. O. Trulson, G. D. Dollinger and R. A. Mathies, *Femtosecond photochemical excited state ring opening dynamics of 1,3-cyclohexadiene from resonance raman intensities*, Journal of the American Chemical Society **109**, 586 (1987).

[70] M. O. Trulson, G. D. Dollinger and R. A. Mathies, *Excited-state structure and femtosecond ring-opening dynamics of 1,3-cyclohexadiene from absolute resonance raman intensities*, Journal of Chemical Physics **90**, 4274 (1989).

[71] S. A. Trushin, W. Fuß, T. Schikarski, W. E. Schmid and K. L. Kompa, *Femtosecond photochemical ring opening of 1,3-cyclohexadiene studied by time-resolved intense-field ionization*, Journal of Chemical Physics **106**, 9386 (1997).

[72] Z. Vager, R. Naaman and E. P. Kanter, *Coulomb explosion imaging of small molecules*, Science **244**, 426 (1989).

[73] H. V. von Geramb (Ed.), *Quantum Inversion Theory and Applications*, Springer, New York, N.Y. (1994).

[74] J. C. Williamson, J. Cao, H. Ihee, H. Frey and A. H. Zewail, *Clocking transient chemical changes by ultrafast electron diffraction*, Nature **386**, 159 (1997).

[75] G. A. Worth, H.-D. Meyer and L. Cederbaum, *The effect of a model environment on the S_2 absorption spectrum of pyrazine: A wave packet study treating all 24 vibrational modes*, Journal of Chemical Physics **105**, 4412 (1996).

[76] G. A. Worth, H.-D. Meyer and L. Cederbaum, *State filtering by a bath: up to 24 mode numerically exact wavepacket propagations*, Chemical Physics Letters **299**, 451 (1999).

[77] A. J. Wurzer, S. Lochbrunner and E. Riedle, *Highly localized vibronic wavepackets in large reactive molecules*, Applied Physics B **71**, 405 (2000).

[78] A. Zewail, *Femtochemistry*, Journal of Physical Chemistry **97**, 12427 (1993).

[79] D. H. Zhang and J. C. Light, *Potential inversion via variational generalized inverse*, Journal of Chemical Physics **103**, 9713 (1995).

[80] W. Zhu and H. Rabitz, *Molecular dipole function inversion from time dependent probability density and electric field data*, Journal of Physical Chemistry A **103**, 10187 (1999).

[81] W. Zhu and H. Rabitz, *Potential surfaces from the inversion of time dependent probability density data*, Journal of Chemical Physics **111**, 472 (1999).

[82] W. Zhu and H. Rabitz, *Multidimensional potential surfaces from the direct inversion of probability density and energy spectral data*, Journal of Physical Chemistry B **104**, 10863 (2000).

[83] W. Zhu and H. Rabitz, *Excited state potential energy surfaces from the inversion of absorption spectra: Removal of a global singularity*, Journal of Chemical Physics **114**, 4434 (2001).

Thanksgiving!

Meinen Dank allen, mit denen ich das Glück hatte, während der Promotionszeit in den vergangenen dreieinhalb Jahren in Garching / München verbunden zu sein. Im besonderen möchte ich danken ...

... Regina de Vivie-Riedle, die mir eine interessante und vielfältige Promotionszeit ermöglicht hat. Herzlichen Dank für die weitgehende Freiheit in der Umsetzung der Fragestellungen und das entgegengebrachte Vertrauen. Ich hoffe, mich teilweise revanchiert zu haben oder zumindest das an anderer Stelle weiterreichen zu können.

... den Menschen, mit denen ich einen großen Teil meiner angenehmen (Arbeits-) Zeit verbracht habe, die mir halfen, und die mich erdulden mussten: Karsten Sundermann, Carmen Tesch, Thomas Hornung und Dorothee Geppert. Judith Voll möchte ich danken für die Zusammenarbeit bei Grafiken, die in die Arbeit Eingang fanden. Besonderer Dank gebührt Angelika Hofmann für Freundschaft und eine langjährige angenehme und erfolgreiche Zusammenarbeit, die das Gelingen der Arbeit ermöglichte.

... Herschel Rabitz, working on the inversion with you was great fun. Merci aussi à Vincent de Waele pour travailler avec moi dans le projet HBT.

... den Dokoktoranden, Postdocs und Diplomanden am MPQ. Ich habe eine schöne Promotionszeit hier verbracht. Im Besonderen sei Andreas Kemp, Robert Pfund, Sergei Gordienko, Malte Kaluza und Matthias Dreher für viele anregende Mensagänge gedankt. Ebenso mein Dank an Christine Bucher, Enrique Solano und Giovanna Morigi und „Hoch die Kaffeetassen!“ an Andreas Krug, Jens Schneider und Christoph Skornia. Keinesfalls sei Renate Weise-McKnight als Postdoc h.c. vergessen.

... Lorenz Welker für extrem viel Geduld und Aufmerksamkeit.

... Conni Schmitt, Julia Skornia und Rita Neiteler aber auch Adrianna und Wolfgang Streit, Tanja Labonte und Stephan Schneider, Cordula Schultheis und Jean Philippe Bitterlin sowie Carolin Semtner und Helge Garke, die als WG-Mitbewohner, Nachbarn und Freunde mit zu den angenehmen Seiten im Münchener Leben zu rechnen sind.

... meinen Telefonseelsorgern vor allem in der Anfangszeit in der Bayrischen Wildnis: Jan Kunterding, Carsten Bolwien, Christoph Klein und Felix Hüning.

... meinen Eltern und Geschwistern sowie den beiden Jüngsten Paula und Jan für ihre beständige Unterstützung und Zuneigung.

Curriculum Vitae

Persönliche Daten: Lukas Karl Kurtz
geboren am 18. April 1971 in Wodzisław Śl., Polen
ledig

1977 Übersiedlung nach Deutschland und Einbürgerung
Einschulung in Unna

1981 Weiterführender Schulbesuch zunächst am Ritzefeld-Gymnasium, Stolberg Rheinl.

1987 Aufnahme in den Förderzweig der Jugenddorf-Christophorusschule, Braunschweig

1990 Abitur
Wehrdienst als Sanitätssoldat im PzArtBtl 155, Lahnstein

1991 Beginn des Physikstudiums an der RWTH Aachen

1994 Vordiplom

1998 Diplom in Physik
Anfertigung der Diplomarbeit am Institut für Theoretische Physik, Lehrstuhl B unter Anleitung von Prof. Dr. Volker Dohm
Kritisches Verhalten des $O(n)$-symmetrischen ϕ^4-Modells für $n \to \infty$ im thermodynamischen Limes und in endlicher Geometrie

Seit April Forschungstätigkeit im Bereich Theoretische Femtochemie des Max-Planck-Instituts für Quantenoptik mit dem Ziel der Promotion; Betreuung durch Priv. Doz. Dr. Regina de Vivie-Riedle